ELLIPTICALLY POLARIZED LIGHT FOR DEPTH RESOLVED DIFFUSE REFLECTANCE IMAGING IN BIOLOGICAL TISSUES

SUSMITA SRIDHAR

DiMABio
Institut Fresnel
Aix-Marseille Université

Medical Optics Group
ICFO - Institut de Ciències Fotòniques
Universitat Politècnica de Catalunya

SUPERVISORS:
Dr. Anabela DA SILVA
Prof. Dr. Turgut DURDURAN

ELLIPTICALLY POLARIZED LIGHT FOR DEPTH RESOLVED DIFFUSE REFLECTANCE IMAGING IN BIOLOGICAL TISSUES

SUSMITA SRIDHAR

A thesis under the supervision of

DR. ANABELA DA SILVA

and

PROF. DR. TURGUT DURDURAN

submitted in partial fulfillment of the requirements for the degree of

DOCTOR

by

Aix-Marseille Université

and

Universitat Politècnica de Catalunya

5th October 2016

AIX-MARSEILLE UNIVERSITÉ

UNIVERSITAT POLITÈCNICA DE CATALUNYA

INSTITUT FRESNEL

ICFO - INSTITUT DE CIÈNCIES FOTÒNIQUES

PHD Thesis as part of the doctoral school

PHYSICS AND SCIENCES OF MATTER: ED352
with specialization in: OPTICS, PHOTONICS AND IMAGE PROCESSING

presented by

SUSMITA SRIDHAR

on 5th October 2016

Elliptically Polarized Light for Depth Resolved Diffuse Reflectance Imaging in Biological Tissues

MEMBERS OF THE PHD COMMITTEE:

REVIEWER: Prof. Dr. Walter BLONDEL
REVIEWER: Dr. Udo WEIGEL
MEMBER: Dr. Pablo LOZA-ALVAREZ
PH.D SUPERVISOR: Dr. Anabela DA SILVA
PH.D CO-SUPERVISOR: Prof. Dr. Turgut DURDURAN

ABSTRACT

Polarization gating imaging is a popular and widely used imaging technique in biomedical optics to sense tissues, deeper volumes, and also selectively probe sub-superficial volumes. Due to the 'polarization memory' effect of polarized light, elliptical polarization-gating allows access to tissue layers between those of accessible by linear or circular polarizations. As opposed to the conventional linearly polarized illumination, we focus on polarization gating methods that combine the use of elliptically polarized light to select polarization-maintaining photons and eliminate the background while providing superior contrast and depth information. With gating, it has also become possible to access user-defined depths (dependent on optical properties) in biological tissues with the use of images at different ellipticities. Furthermore, this investigation allowed the application of polarization gating in spectroscopy to selectively quantify the concentration of tissue chromophores at user-desired depths. Polarization gating methods have been validated and demonstrated with *in vivo* experiments on abnormalities of human skin (nevus, burn scar) and also on the exposed cortex of an anaesthetized rat. Finally, as a first step towards the use of coherent illumination, adding the concept of polarimetry to laser-speckle imaging was demonstrated. Preliminary tests on phantoms (solid and liquid) suggested evidence of the influence of polarization ellipticity on the formation and behaviour of speckles, which could pave the way for more insight in the study of blood flow in tissues.

KEYWORDS: Polarization, elliptically polarized light, polarization gating, depth resolution, biomedical imaging;

RÉSUMÉ

L'imagerie de filtrage en polarisation est une technique populaire largement utilisée en optique pour le biomédical pour le sondage des tissus superficiels, pour le sondage de volumes plus profonds, mais aussi pour l'examen sélectif de volumes sub-surfaciques. Du fait de l'effet de '*mémoire de polarisation*' de la lumière polarisée, l'imagerie de filtrage en polarisation elliptique est sensible à des épaisseurs de tissus différentes, depuis la surface, accessible avec la polarisation linéaire, jusqu'à une épaisseur critique accessible par la polarisation circulaire. Nous nous concentrons sur des méthodes utilisant des combinaisons de polarisations elliptiques afin de sélectionner la portion de lumi ère ayant maintenu son état de polarisation et éliminer le fond pour un meilleur contraste avec, de plus, une information sur la profondeur. Avec ce type de filtrage, il est possible d'accéder à des profondeurs de tissus biologiques bien définies (selon ses propriétés optiques) selon l'ellipticité de polarisation. De plus, ces travaux ont permis d'étendre la méthode à la spectroscopie pour quantifier sélectivement la concentration en chromophores à une profondeur spécifique. Les méthodes développées ont été validées *in vivo* à l'aide d'expériences réalisées sur des anomalies de la peau (grain de beauté, cicatrice de brûlure) et aussi sur le cortex exposé d'un rat anesthésié. Enfin, une étude préliminaire a été réalisée pour examiner la possibilité d'étendre la méthode à l'imagerie de tavelures (speckle). Des tests préliminaires réalisés sur fantômes (solides et liquides) montrent l'influence de l'ellipticité de polarisation sur la formation et le comportement du speckle, ce qui offre la possibilité d'accéder à des informations sur le flux sanguin à des profondeurs spécifiques dans les tissus.

MOT CLÉS: Polarisation, lumière polarisée elliptiquement, filtrage en polarisation, résolution de profondeur, imagerie biomédicale;

RESUMEN

"Polarization gating imaging" es una técnica de imagen muy popular y ampliamente empleada en óptica biomédica con el fin de caracterizar tejidos y sondear volúmenes subsuperficiales de manera selectiva incluso a regiones profundas. Debido al efecto conocido como memoria de polarización de la luz polarizada, la técnica de "polarization gating" elíptica permite el acceso a capas de tejido que, de otro modo, no son accesibles mediante polarización lineal y circular. En contra de la iluminación linealmente polarizada convencional, nuestro estudio se centra en los métodos de "polarization gating" en combinación con luz elípticamente polarizada. Esto permite discriminar aquellos fotones que mantienen una polarización concreta, eliminando así el fondo al mismo tiempo que proporciona un mayor contraste y profundidad de campo, incrementando notablemente la información extraída. Gracias a esta técnica es posible el acceso a distintas profundidades en tejidos biológicos definidas por el usuario (dependiendo de las propiedades ópticas) mediante el empleo de imágenes a distinta elipticidad. Es más, este estudio ha permitido la aplicación del método "polarization gating" a la espectroscopia con el fin de cuantificar la concentración de ciertos cromóforos presentes en tejidos biológicos de manera selectiva y a distintas profundidades deseadas. Los métodos de "polarization gating" han sido validados, establecidos y demostrados en experimentos in-vivo sobre anomalías en tejidos epiteliales humanos (nervios, cicatrices por quemadura) y también en el córtex expuesto de una rata anestesiada. Finalmente, como primer paso en el uso de iluminación coherente, se ha añadido y demostrado el concepto de polarimetría a la técnica de speckle imaging por láser. Los test preliminares en "phantoms" (tanto en sólido como en líquido) arrojan indicios sobre una influencia de la polarización elíptica en la formación y comportamiento de la distribución de las motas (speckle), lo cual podría abrir nuevas puertas y dar un nuevo enfoque sobre la comprensión de la circulación de la sangre en los tejidos.

PALABRAS CLAVES: Polarización, luz elípticamente polarizada, polarization gating, resolución de profundidad, imágenes biomédicas;

Thriving on the lines of Benjamin Franklin,
Well done is better than well said.

ACKNOWLEDGMENTS

This thesis, like many others', has been no less than a whirlwind of memories, information, inspiration, and, confusion. I would like to reflect on all the people who have supported and helped me so much throughout this experience.

I would first like to thank my supervisor, Dr. Anabela Da Silva, whose expertise, understanding, and patience, added considerably to my graduate experience. I really appreciate her skills and efforts in guiding me in all the time of research and also in writing my thesis. You definitely provided me with the tools that I needed to choose the right direction and successfully complete my thesis. I would also like to express my gratitude to Prof. Dr. Turgut Durduran, my second supervisor, for all his valuable guidance despite his many other academic commitments.

It has indeed been a great experience and a pleasure to be a part of Institut Fresnel. Dozens of people have helped and taught me immensely in ways I cannot express. The list is endless, Juan, Martin, Naveen, Satish, Sid, Simona, Siwei, Tassos and Wiktor, thanks for the great company, especially in my initial days in France. A special shout out to my lunch group buddies for providing all the entertainment and helping me keep mind off work. Institut Fresnel has truly been my home and family these past three years.

Being a part of the Europhotonics Joint Ph.D program from Erasmus Mundus, I had the good fortune of spending a few months at Institute of Photonic Sciences (ICFO) in Castelldefels, Barcelona. I really owe it all to the people I met there for making my stay so pleasant and enjoyable. A special mention to the 'volleyball team' in Castelldefels, for constantly keeping my spirits high during the writing phase. This program has indeed given me so many friends and unforgettable experiences. I would like to sincerely acknowledge the grant from the European commission for the Europhotonics program (Grant No. 159224-1-2009-1-FR-ERA MUNDUS-EMJD).

It goes without saying that I am completely indebted to my family. My parents, Roopa and Sreedhar, have been my strongest support for never doubting my dreams, always giving me their wise counsel and pushing me higher. My big sister, Suchetha, who has always been such a great role-model for me, thanks for setting high standards! My husband and confidante, who at every step on the way, pushed me with his encouraging words, 'to handle success, one must first learn to handle stress'. I definitely could not have done this without your constant presence, Swaroop. And finally, I would like to thank my grandparents, who had so much in making me what I am today. I wish you were all here to see this

happening.

Last, but not the least, I would love to thank all my friends and extended family for always being there. In spite of my best efforts to be very precise and accurate, if any errors have crept in, I take full responsibility for them.

CONTENTS

LIST OF FIGURES

LIST OF TABLES

ACRONYMS

2D	Two-dimensional
3D	Three-dimensional
CBF	Cerebral Blood Flow
CCD	Charge-coupled Device
CMOS	Complementary metal-oxide-semiconductor
DCS	Diffuse Correlation Spectroscopy
DOP	Degree of Polarization
DOLP	Degree of Linear Polarization
DOCP	Degree of Circluar Polarization
DOT	Diffuse Optical Tomography
DRS	Diffuse Reflectance Spectroscopy
EPDI	Elliptical Polarization Difference Imaging
EPRS	Elliptical Polarized Reflectance Spectroscopy
FOV	Field of View
HSI	Hyper-Spectral Imaging
IOS	Intrinsic Optical Signal
IR	Infra-red
LASCA	Laser Speckle Contrast Analysis
LCD	Liquid Crystal Display
LDF	Laser Doppler Flowmetry
LHS	Left Hand Side
LPDI	Linear Polarization Difference Imaging
LSF	Laser Speckle Flowmetry
LSCI	Laser Speckle Contrast Imaging
MBLL	Modified Beer-Lambert's Law
MFP	Mean Free Path

MFP′	Transport Mean Free Path
MPDI	Multi-Polarization Difference Imaging
MVD	Mean Visitation Depth
MRI	Magnetic Resonance Imaging
MSE	Mean-Square Error
NIH	National Institutes of Health
NIR	Near Infra-red
OCT	Optical Coherence Tomography
PAT	Photo Acoustic Tomography
PDI	Polarization Difference Imaging
PDT	Photo Dynamic Therapy
PET	Positron Emission Tomography
PSA	Polarization State Analyzer
PSG	Polarization State Generator
QWP	Quarter-Wave Plate
ROI	Region of Interest
RTE	Radiative Transfer Equation
SCOS	Speckle Contrast Optical Spectroscopy
SNR	Signal-to-noise Ratio
VRTE	Vectorial Radiative Transfer Equation

SYMBOLS

A	Attenuation
α	Alpha factor for Multi-Polarization Difference Imaging (MPDI)
α_s	Alpha factor for spectroscopy
δ	Phase
ϵ	Specific absorption coefficient of absorbing species
κ	Speckle contrast
κ_P	Polarization gated speckle contrast
κ_{PC}	Noise-corrected polarization gated speckle contrast
λ	Wavelength
ω	Angular frequency
φ	Angle of elliptical polarization, ellipticity
ρ	Concentration of absorbing species
θ	Angle of incidence
σ_I	Standard deviation of measured intensity over different speckles separated in space or time
μ_I	Mean of the measured intensity over different speckles separated in space or time
C1	Co-linear channel
C2	Cross-linear channel
C3	Co-elliptical channel
C4	Counter-elliptical channel
ρ_{oxy}	Oxyhaemoglobin concentration
ρ_{deoxy}	Deoxyhaemoglobin concentration
d	Optical path length
DP_l	Differential path length
$\vec{E}$	Electric-field vector

E_0	Electric-field amplitude
$E_\perp$	Perpendicular electric-field vector
$E_\parallel$	Parallel electric-field vector
ϵ_{oxy}	Molar extinction coefficient of Oxyhaemoglobin
ϵ_{deoxy}	Molar extinction coefficient of Deoxyhaemoglobin
f	Natural frequency
$f\#$	F-number of a camera/system
g	Anisotropy factor
g_1	Electric-field temporal autocorrelation function
g_2	Intensity temporal autocorrelation function
G	Constant offset in attenuation
Hb	Deoxyhaemoglobin
HbO_2	Oxyhaemoglobin
I_{Max}	Maximum signal intensity
I_{Min}	Minimum signal intensity
$I_\parallel$	Linearly polarized parallel image intensity
$I_\perp$	Linearly polarized orthogonal image intensity
$I_{45°}$	45° Linearly polarized component
$I_{135°}$	135° Linearly polarized component
I_R	Right circularly polarized component
I_L	Left circularly polarized component
I_S	Signal intensity
I_N	Signal noise
k	Wave number
l_a	Absorption length
l_s	Scattering length
M	Magnification
MS_E	Multiple-scattered photons from elliptical polarization
MS_L	Multiple-scattered photons from linear polarization

μ_a	Absorption coefficient
μ_s	Scattering coefficient
μ_s'	Reduced scattering coefficient
μ_t	Total attenuation coefficient
n	Refractive index
P_E	Polarization-maintaining photons from elliptical polarization
P_L	Polarization-maintaining photons from linear polarization
ρ_{pixel}	Speckle size
$\rho_{speckle}$	Speckle size
R	Ratio of concentrations of two chromophores
R'	Estimate of R
S	Stokes Vector
S_E	Surface-reflected photons from elliptical polarization
S_L	Surface-reflected photons from linear polarization
t	Image exposure time
T	Transmission co-efficient for a given wavelength, λ
TiO_2	Titanium di-oxide

1 INTRODUCTION

Light has always played an important role in medicine dating back to the prehistoric times, when sunlight was believed to have healing powers for the mind as well as the soul. With the advent of science and technology, the contribution of light to medicine has evolved throughout human history, starting from the invention of the microscope in the 17th century to today's sophisticated Optical Coherence Tomography (OCT) tools. The basic idea revolves around the exploitation of the various properties and characteristics of light. Optical imaging techniques use radiation from the visible range of wavelengths to Near Infra-red (NIR). The simplest of these properties is, light absorption, where incident light from a source causes a potentially therapeutic (or damaging) effect on a tissue. This effect permits quantitative identification of the molecules present in a sample, their concentration and their local environment and also serves as a mechanism of optical contrast during imaging. The other important event is, light scattering, which provides feedback during therapy. It is mainly dependent on the ultra-structure of the tissue and proves as an excellent diagnostic tool for imaging. Generally, these traditional optical techniques are rigorous and are well established in simple, homogeneous, optically thin samples.

A thorough physical understanding of photon propagation in biological tissues (which is a highly scattering media), is required to use these characteristic properties of light. A breakthrough contribution to the evolution of optical imaging was given by Jöbsis [Jöbsis, 1977; Jöbsis van der Vliet, 1999; Jöbsis van der Vliet and Jöbsis, 1999] in the 1970's when he observed a spectral window in the NIR (~650-950nm) range wherein photons could travel deep in tissue as a result of the relatively small absorption of water and haemoglobin (discussed in detail in Section 2.2).

Optical imaging methods used for living organisms can be classified in two categories:

High-resolution microscopy, which focuses on infinitely small cells and ideally, molecules *in vivo*, with the objective to push back the limits of geometrical optics to enhance the understanding of biological mechanisms. These techniques use micro- or mesoscopic approaches, where coherence and phase of the electromagnetic wave are maintained for high-resolution imaging. The coherence properties of light are used to push back these limits along with the use of clever optical systems to overcome parasitic phenomena and to also increase the signal to noise ratio.

Thick tissue imaging, which probes human organs, such as the breast or the brain, or is used for pre-clinical imaging of small animals (laboratory mice). The challenge is to achieve imaging of objects with low contrast, such as tumours, through several centimetres of highly absorbent and diffusing tissue, with sufficient resolution. These techniques use meso- or macroscopic approaches, where the information is gathered from measurements of luminous flux for the examination of deep tissue. Propagation of light is done incoherently, and the ability to manipulate the system is limited, thus creating a need for the development of sophisticated physical models to understand and account for the prop-

agation in these random environments.

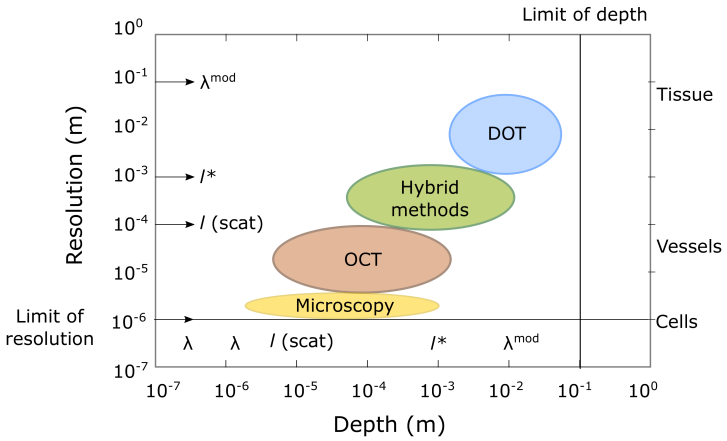

Figure 1.1: Multi-scale optical imaging. In NIR, the reference scales are the wavelength $\lambda \sim 1\mu m$, the elastic scattering length $l(scat) \sim 20-40\mu m$, transport length $l^* \sim 1mm$, and the modulation length of the macroscopic diffuse wave, photon density, $\lambda^{mod} \sim 10cm$ [Tromberg et al., 2005].

Figure 1.1 categorizes the four major families of optical imaging techniques classified according to depth of penetration and resolution: Microscopy; OCT; Hybrid methods, using a selection of specular or quasi-specular photons; and Diffuse Optical Tomography (DOT), to probe deep structures for which there no longer are specular photons. Figure 1.2 shows optical imaging techniques that complement the other imaging techniques (Ultrasound, X-ray tomography, Magnetic Resonance Imaging (MRI), Positron Emission Tomography (PET)). Optical imaging techniques cannot achieve "whole-body" imaging, but they can compete with conventional techniques, particularly PET for centimetric scale probes and, at the microscopic level, optical techniques obviously remain as the reference.

The advancement of optical imaging techniques has been progressing drastically from the past twenty years by offering many advantages that paved as an alternative to conventional biomedical imaging techniques – They a) use non-ionizing radiation, proving harmless to the patient; b) allow for a non-invasive tissue "biopsy"; c) are of low-cost hardware and can easily be implemented in a preclinical or clinical unit (contrary to MRI or PET techniques that require a specific imaging department). The technique we are trying to develop in this thesis allows for exploring an intermediate "mesoscopic" scale, ranging from 10μm to a few mm, to provide a model for superficial examination of biological tissue (or relatively transparent) which gives both, axial/spatial (wide-field) and depth resolution.

Biological tissue is a multi-layered, heterogeneous structure with cells (a few μm), membranes (a few nm), mitochondria (approx. 1μm) and the presence of these structures in the trajectory of the light beam modifies or defines its path. The main problem of light interactions with biological tissues in the optical wavelength range is the strong scattering of light. Most optical imaging methods not only face the common obstacle of image degradation and blurring which limit the ability to identify objects with high-resolution and contrast but also suffer from a lack of resolution in depth. As photons undergo multiple

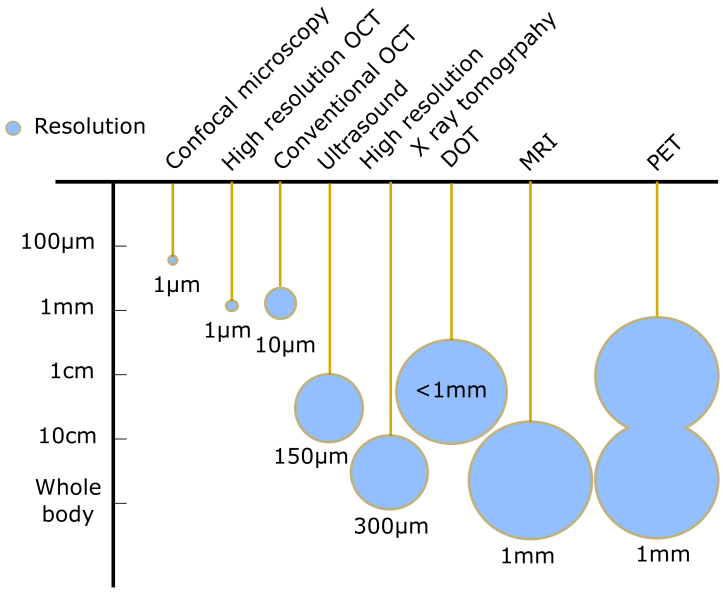

Figure 1.2: Resolution according to depth for different imaging techniques [Da Silva, 2013].

scattering events before being detected, it is difficult to associate a probed depth to the detected signal. Images are Two-dimensional (2D) projections of a combination of signals from superficial and deeper tissue layers, with an *a priori* unknown proportion. Conventional optical imaging of Intrinsic Optical Signal (IOS) provides high-resolution functional 2D images, by monitoring changes in absorption of intrinsic chromophores. As *in vivo* IOS measurement is usually performed under reflectance geometry [Tuchin, 2000], illumination sources and detectors belong to the same half-space. However, such systems do not allow depth discrimination which is very important in order to know the degree of invasiveness of a certain tumour, or to improve the quality of images that is degraded due to blurring. Blurring occurs mainly due to: (a) mirror reflections at the surface and (b) diffused light coming from the deeper tissues. The blurring due to specular reflection at the surface, can be easily overcome by working with linear polarization illumination and cross-polarization detection. But, at this point the depolarized backscattered detected photons (those who have undergone a large number of scattering events) are likely to come from deep locations. Moreover, the selective detection of photons stemming from the surface or other specific depths remains a challenge. Polarization gating has been widely used to selectively probe the structure of superficial biological tissue. Depth-selective measurements are crucial to differentiate single and low-order scattering originating in the superficial tissue (e.g. epithelium) from the light multiply scattered in deeper tissue. Recently, it has been demonstrated that elliptically polarized light is capable of selecting sub-surface volumes in turbid medium and in biological tissues [Rehn et al., 2013].

Polarization gating is a simple method that uses information of the polarization state of the detected backscattered light to filter the unpolarized/depolarized photons. The propagation of light in a scattering medium is accompanied by a loss of polarization due to multiple interactions between the electromagnetic field and scatterers, resulting in changes

of amplitude and direction of the field [Bicout and Brosseau, 1992; Bicout et al., 1994; MacKintosh et al., 1989; Tuchin, 2000; Yoo and Alfano, 1989]. The use of polarizing filters allows, up to a point, selecting photons for which polarization state is maintained: this is the basis of the polarization gating imaging methods. It is understood that beyond a certain optical thickness, depending on the number of scattering events, anisotropy factor, and also absorption, photons will completely lose memory of their initial polarization - as was demonstrated by MacKintosh et al. [1989] and called the *polarization memory effect*. This effect describes how the original polarization is maintained during a number of scattering events for a given polarization and showed that the polarization of circularly polarized light is indeed maintained through a larger number of scattering events than that of linearly polarized light. It is shown that this effect depends mainly on the size the scattering particle, i. e. the Anisotropy factor (g). Since biological tissues are Mie scatterers [Tuchin, 2000], this filtration with circularly polarized light can indeed be achieved in tissues, allowing a deeper screening than linearly polarized light. If the particles are very small (Rayleigh scattering), the opposite occurs, due to the numerous changes of helicity of circular polarization with multiple reflections. This concept has been used in various areas of research to locate or analyse specific regions in samples. Initial polarization will be maintained only for a certain number of scattering events until total depolarization is reached [MacKintosh et al., 1989]. Commonly, linear polarization and more rarely circular polarization are used for polarization gating. It was shown that this method allows light extraction from superficial tissue [Demos and Alfano, 1997], whereas circular polarization is sensitive to deeper layers [Morgan and Ridgway, 2000]. If the diffusing medium is composed of Mie scatterers as in most biological tissues, because of polarization-memory effects [Bicout et al., 1994; MacKintosh et al., 1989] the depth defined by a circular-polarization gate is shown to be larger than that defined by a linear-polarization gate. Moreover, as circular polarization undergoes a helicity flip with mirror reflection, this technique thus allows screening of subsurface tissues deeper than linearly polarized light, without any blurring due to surface mirror reflection. Preliminary studies [Da Silva et al., 2012] have shown that elliptical polarization-gating is sensitive to tissue layers between those of the two latter mentioned polarizations and is also illustrated in Figure 1.3.

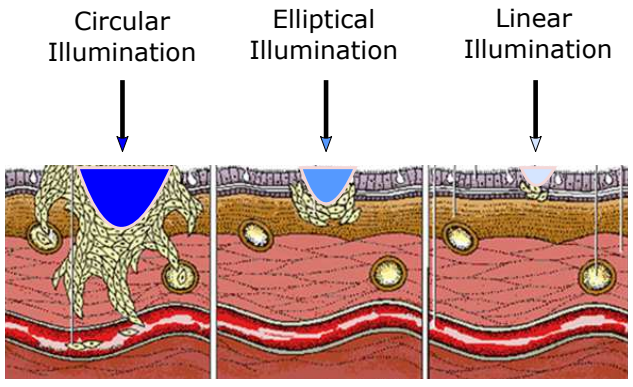

Figure 1.3: Resolution according to depth for different imaging techniques. [Da Silva et al., 2012]

In this thesis, we have chosen to develop this approach of polarization gating because it allows for non-contact tissue examination over a large (wide-field) Region of Interest (ROI) with low-cost instrumentation. In addition and in comparison to practised techniques, we develop new methods to access polarization maintaining photons and retrieve depth information from different samples ranging from tissue mimicking liquid phantoms to real-time *in vivo* imaging of Human skin.

1.1 AIM AND STRUCTURE OF THE WORK

The aim of this Ph.D thesis is centred around the study of elliptically polarized light and how it can be exploited to extract information from biological tissue, with enhanced spatial as well as depth resolution. The manuscript has been categorized in three main aspects depending on the source, illumination type, sample and type of information that can be measured/quantified.

The first part deals with the understanding of elliptically polarized light and its role in polarization gating by means of image subtraction and the quality of information that can be extracted from this method of imaging biological tissues. In Chapter 2 I present the existing state-of-the-art techniques and the evolution of polarization gating imaging or in short, polarimetry. The comparison of polarimetric imaging to its contemporaries in optical and medical imaging is also presented. To study biological tissues, the obvious starting point is the light-matter interaction and a thorough knowledge of the absorption, scattering and anisotropy behaviour of various tissues with light, and especially polarized light. An introduction into the methods that describe the state of polarization: Jones and Stokes vectors encompassing the Pointcaré sphere is also included in this chapter. Polarized light transport in biological media has been studied using the Vectorial Radiative Transfer Equation (VRTE) with Monte-Carlo simulation-based solutions. Although this was studied as a part of this thesis, some of the assumptions and results from a previous study [Rehn, 2012] have been used to develop ideas and concepts of depth resolution in this manuscript. Another major concept discussed in this chapter is the differences between measuring the effective contrast in terms of Degree of Polarization (DOP) and collecting only the polarization maintaining photons (as in the case of Linear Polarization Difference Imaging (LPDI), Elliptical Polarization Difference Imaging (EPDI) and Multi-Polarization Difference Imaging (MPDI)). The use of elliptically polarized light including the characteristics with a focus on 'polarization memory', role in polarization gating and different types of polarization gating has been described extensively in Chapter 3. Chapter 3 also describes the instrumentation and calibration of the experimental set-up and samples' preparation to achieve different polarization gating methods: Linear Polarization Difference Imaging (LPDI), Elliptical Polarization Difference Imaging (EPDI) and Multi-Polarization Difference Imaging (MPDI). Polarization gating methods based on subtraction of background employ different channels with polarization-sensitive (linear, elliptical or circular) illumination and detection for accessing photons with different characteristics. Automation of the set-up with faster image acquisition was achieved to reduce unforced manual errors and minimize motion artefacts. Another key milestone was set in image processing with the development of an image registration algorithm that reduced motion

artefacts from the order of $10-12$ pixels to ~ 1 pixel. With the theory, instrumentation and image acquisition system developed, the results of different polarization gating methods were compared and presented in Chapter 4 for different samples. The calibration and validation of the method was first carried out on solid and liquid phantoms based on Intralipid® solution with matched optical properties. The signal intensity and contrast for MPDI that involves use of various polarization channels was seen to be superior to linear and elliptical gating methods. Another key fact was the probing in depth achieved with each increasing ellipticity. These results were further verified on chicken sample to check for biological feasibility of the method. The superior contrast and signals were consistent and proved a reliable method for *in vivo* imaging as well. Before going into the details of quantification of the volumes probed, it was essential to check the behaviour of this method for a spectrum of wavelengths. With the results of Rehn [2012]; Zonios and Dimou [2006], it was possible to develop a 3D relationship between wavelength used, ellipticity of polarization and depth probed. A detailed summary of this technique to access user-defined depths is presented at the end of Chapter 4.

The second aspect that is dealt with in this thesis is the union of spectroscopy and depth probing via polarimetric methods. The measurement of tissue oxygenation being one of the main focus points for diagnosis of various diseases, is of interest in this study as well. The fact that elliptically polarized light can retain their incident polarization for a number of scattering events (or Mean Free Path (MFP)s) depending on the optical properties, makes it possible for polarization gated spectroscopy. For this purpose, we have developed an algorithm based on the Modified Beer-Lambert's Law (MBLL) as demonstrated by Stockford et al. [2007] that uses multi-wavelength images that have been processed by MPDI. This algorithm was applied to *in vivo* images obtained at different wavelengths for the exposed cortex of an anaesthetized rat to check the efficiency of the algorithm and assess the extracted information. Mapping the attenuation of images at different depths was made possible using the manipulations of the algorithm at different wavelengths (minimum of three). Calculation of the Ratio of concentrations of two chromophores (R) has been described for different imaging samples and the values and related conclusions have also been discussed in this chapter.

The third and final part of this manuscript revolves around the study of the 'polarized speckle'. Chapter 6 represents a new application of the polarization gating methods to coherent light, i. e. it's incorporation in speckle contrast calculation for the measurement of blood flow *in vivo*. Polarization gating with background subtraction (using EPDI) was developed for speckle contrast calculation. Preliminary tests were done on solid and liquid Intra-lipid® based phantoms and they showed evidence that the polarization channels influence the photon paths and change the value of speckle contrast accordingly. It suggested that the possibility of accessing depth information and depth characterization is very high with this method and marks the starting point for *in vivo* applications like depth-resolved blood flow sensing.

Finally, in Chapter 7, I present the concluding remarks to sum up the results presented in this manuscript. This thesis has been a part of the Europhotonics Erasmus Mundus Joint Doctorate program between Institut Fresnel in Marseille, France and The Institute of

Photonic Sciences (ICFO) in Barcelona, Spain under the the supervision of Dr. Anabela Da Silva and Prof. Dr. Turgut Durduran respectively. This work was supported by the European Commission through the Erasmus Mundus Joint Doctorate Programme Europhotonics (Grant No. 159224-1-2009-1-FR-ERA MUNDUS-EMJD). The animal experiments were done in collaboration with Dr. Ivo Vanzetta from Institut des Neurosciences de la Timone (INT), Aix-Marseille Université, Marseille.

2

POLARIMETRIC IMAGING OF BIOLOGICAL TISSUES

This chapter deals with the description of the existing state-of-the-art imaging techniques for the examination of biological tissues, highlighting the advantages of the optical imaging techniques, and in particular, polarimetric methods and technology that we have developed in the course of this thesis. Firstly, the contribution of optics for the examination of biological tissues is discussed in detail. We have then described the physical phenomena governing the interaction between the incident light beam and tissue at the microscopic level (molecules). This is followed by the introduction of the definitions of physical quantities used and the detailing of the intrinsic property of light used in this work, i. e. Polarization.

2.1 INTRODUCTION

The use of light for biomedical applications dates back to the 19th century, where candle light was the only source of illumination. It is indeed interesting to follow the evolution of optical methods from that point. With the onset of quantum theory, molecular spectroscopy became a revolution in the mid-1950s. With molecular spectroscopy, light was used in many different ways to analyse complex biological systems and understand nature at the molecular level. Light at a certain wavelength was used to irradiate the sample (e.g., a bodily fluid, a tissue, or an organ) in a process called excitation. Then some of the properties of the light that emerged from the sample were measured and analysed. Some analyses dealt with the fraction of the incident radiation absorbed by a sample; the techniques involved are called absorption spectroscopies (e.g., ultraviolet, visible, IR absorption techniques). Other analyses included examining the incident radiation that was dissipated and reflected back from the samples (elastic scattering techniques). Alternatively, it became possible to measure the light emitted and scattered by a sample, that occurred at wavelengths different from the excitation wavelength: by means of techniques like fluorescence, phosphorescence, Raman scattering, and inelastic scattering. Other specialized techniques were also used to detect specific properties of emitted light (circular dichroism, polarization, lifetime, etc.). The range of wavelengths used in molecular spectroscopy to study biological molecules is quite extensive. Molecular spectroscopic techniques have led to the development of a wide variety of practical techniques for minimally invasive monitoring of disease. For instance, Chance et al. [1988] developed and used NIR absorption techniques to monitor physiological processes and brain function non-invasively. Today, a wide variety of molecular spectroscopic techniques, including fluorescence, Raman scattering, and bioluminescence, are being developed for cancer diagnosis, disease monitoring, and drug discovery. The use of light for medical applications has now become widespread, mainly owing to the flexibility of use, safety of radiation and also due to the fact a large

number of biological functions can be studied through optical contrasts and low-cost instrumentation.

2.1.1 *Microscopy*

To get a thorough understanding of the various optical techniques commonly used for the examination of biological tissues, it is important to know the optical property on which their operation is based – phase, spatial information, the temporal coherence and polarization. Confocal microscopy, invented by Minsky in 1955, is an elegant and simple method for achieving high image contrast by reduction of light scatter from adjacent (lateral and axial) voxels and is one of the mostly widely used techniques that exploits spatial information [Wilson, 1990]. The lateral resolution of confocal microscopy, typically 0.2 - 1.0µm, enables tissue imaging with a resolution comparable to that of high-magnification histology. In biological tissues, confocal microscopy allows a depth penetration of about 200 - 300µm, since the focus of the illumination beam is limited by scattering in tissues. It is however, applicable to weakly scattering tissues with a small thickness or for surface examination. Since confocal microscopy is a point-to-point imaging technique requiring scanning in 3D of the incident light spot, it is very apt for the observation of small ROI. Current research effort has focused on overcoming the limitations of confocal microscopy. However, due to the loss of focus and its limitation to the examination of small areas, this technique is not feasible for achieving depth resolution. This technique has undergone sophistication owing to the development of two-photon microscopy, which exploits the signal emitted by fluorescent markers *in vivo* or *ex vivo*. It allows for the viewing of different cells with a three-dimensional resolution of the micro-metric scale [Strupler et al., 2007]. This technique has a colossal cost (> 300k Euros), exceeding the instrumentation costs of even some non-optical techniques. It is mainly used to get a better understanding of the cellular mechanisms.

2.1.2 *Macroscopy*

On a macroscopic scale, there are other optical techniques which are based on measuring the macroscopic optical contrast (μ_a, μ_s) using detectors like Charge-coupled Device (CCD) cameras, Complementary metal-oxide-semiconductor (CMOS) cameras etc. This type of instrumentation is very convenient because it allows for quick examination of superficial tissues. To improve the Signal-to-noise Ratio (SNR), two approaches are of use: a) excitation of contrast with the use of exogenous absorbers or fluorescent markers; b) Filtering the light signal to overcome scattering, either by spatial filtering, temporal filtering, interferential filtering or by polarization. OCT is an imaging technique that works on the basis of using temporal information based on low-coherence interferometry, typically employing NIR light. It was first proposed in 1991 by Huang et al. [1991], for deep imaging of a slice of tissue by a point-by-point detection of the backscattered signal and its elimination at the same time. The system is made up of an interferometer (traditionally Michelson) illuminated by a course of low coherence length. OCT allows for three-dimensional imaging of biological tissues providing a depth resolution of a few millimetres depending on

the tissue type. Because the eye is the only transparent organ in the body accessible to *in vivo* and non-invasive examination, it is often the first and best venue for the application of new optical imaging techniques. OCT is a prime example. Before this technique spread rapidly to other fields of inquiry, it was perfected in ophthalmology [Fujimoto et al., 1995; Fukuda et al., 2005; Puliafito et al., 1995; Schuman et al., 1995; Weinreb and Khaw, 2004]. The optics of the eye can be limiting in terms of theoretical achievable resolution (i. e. ocular aberrations, numerical aperture, etc.) compared to conventional or confocal microscopy. These limitations have, however, provided opportunities for the development of tools to overcome them (e.g., adaptive optics). The low cost of the technique makes it very accessible. However, the wavelength used is typically greater than 1000 nm, which offers little access to the study of metabolites such as haemoglobin [Chen et al., 2009; Maheswari et al., 2003] and is also hampered due to the effects of tissue scattering.

To tackle the problems associated with highly diffuse tissues and multiple scattering, a brief review of optical the techniques used is apprehended in this paragraph. The use of multi-scattered photons, as a diffuse optical imaging method dates back to 1831, when Bright [1831] examined the cranium of a hydrocephalic patient, by transparency, using candle light. The same concept was applied by Cutler [1929] for the examination of breast. Diffuse optical imaging experienced renewed interest in the 1980s [Arridge et al., 1986] and 1990s [Yodh and Chance, 1995], as it is a non-ionizing imaging method that utilizes light in the NIR spectral region to measure the optical properties of physiological tissue. This macro imaging technique is based on the exploitation of spatial, spectral or temporal information, contained in diffuse light, that has completely lost all sense of polarization due to multiple-scattering. DOT has gained popularity in the recent years in various deep-tissue applications including breast cancer imaging, brain functional imaging, stroke detection, muscle functional studies, Photo Dynamic Therapy (PDT), and radiation therapy monitoring. The sensitivity and geometric resolution in depth is limited to $< 1\mathrm{cm}$; therefore, this technique cannot be used for whole-body imaging.

2.1.3 *Polarimetry*

The resolution obtained with DOT, PDT and other optical techniques are low, ranging from mm (for small animals) to cm (humans). Contrary to these methods, imaging by polarization gating operate by excluding light that is multiply-scattered and uses the light that has kept its initial polarization [Schmitt et al., 1992]. In 1991, Anderson [Anderson, 1991] showed the use of polarized light to study malignant disease of the skin which led to a new beginning. This method of filtering scattered photons is thus more attractive for our study because of the possibility of selecting and detecting light that has probed the tissue to a certain depth. It is a well-established tool for non-invasive material characterization (various forms of clear media) and involves the comparison of the polarization states of light before and after light interacts with the material. The technique that we have developed in the course of this thesis is based on the selection of photons by polarimetric filtering. In contrast to other optical imaging techniques, polarimetric imaging for biomedical applications has only gained importance over the past 20 years. The interest in this type of imaging has grown recently due to the fact that, unlike conventional techniques based

mainly on the exploitation of attenuating contrasts, polarimetric methods are very sensitive to the structure of the environment. Polarization gating techniques are being used in diverse fields [Ghosh and Vitkin, 2011] ranging from remote sensing applications (metrology [Gadsden et al., 1979], astronomy [Chrysostomou et al., 2007]), computational analysis of waves, to differentiating between normal and precancerous cells [Gurjar et al., 2001], as well as many other applications in biomedical imaging [Tuchin et al., 2006]. The effect of scattering on the polarization state of light has been found very useful for imaging of surface or sub-surface structures in scattering media, and for transmission imaging of deep structures [Rowe et al., 1995]. It has also been shown that the scattering parameters of turbid tissue, including the scattering coefficient, can be determined from spatially dependent intensity patterns of polarized light that is diffusely backscattered from highly scattering media [Hielscher et al., 1997]. The incorporation of polarimetric imaging in more conventional techniques such as microscopy or OCT helps in the extraction of precise information such as on collagenous tissue structure (eye [Ducros et al., 2001], skin [Yasui et al., 2004]). Promising studies of polarimetric examination of tissues were carried out in dermatology and gynaecology [Demos and Alfano, 1997; Jacques et al., 2002; Kapsokalyvas et al., 2013; Morgan et al., 2006; Pierangelo et al., 2013; Stockford and Morgan, 2005; Stockford et al., 2002] , where melanomas or other lesions (lupus) were characterized by various polarimetric indicators (depolarization and birefringence).

The use of polarization property of light is one of the most used method for the examination of superficial tissues. These techniques are based on the fact that the polarization is lost depending on the tissue's scattering properties. The backscattered light thus contains a mixture of polarized and depolarized photons that have undergone small number of scattering events. Polarized light can be extracted by a simple image subtraction method [Jacques et al., 2000] a) for moving beyond the specular and probing more deeply; or b) for selecting the specular photons. It is precisely this approach that we have chosen to develop. Although depth of penetration achieved by polarization gating is limited, this technique is adapted to our study because, it allows: examination of tissue over a large (wide-field) ROI with low-cost instrumentation, usage of markers (absorbers, fluorescent markers) and non-contact tissue examination. However, in a complex random medium-like tissue, numerous complexities due to multiple scattering and simultaneous occurrences of many scattering and polarization events present formidable challenges both in terms of accurate measurements and in terms of analysis of the tissue polarimetry signal. A detailed description of the existing polarimetric imaging techniques for biological tissues is discussed in Section 2.5, for which it is very necessary to understand the basic physical concepts of light-matter interaction, polarization and its nomenclature.

2.2 INTERACTION OF LIGHT-MATTER

In the previous section, we have reviewed the different optical imaging techniques conventionally used in the examination of biological tissues. These imaging techniques are based on the fact that light interacts with biological tissues which helps access certain information. Here, we discuss the optical properties of biological tissues and the specific properties of polarized light that are needed to understand the work done in this thesis.

When light is incident on tissue, some of the light is reflected by the surface, and the rest is transmitted, which means, depending on its optical properties, some of the light is either absorbed and/or scattered.

2.2.1 *Absorption*

In the NIR region (diagnostic and therapeutic window see Fig. 2.1), the optical transparency of tissues is maximal which is due to the low level of absorption of strong intrinsic chromophores (like water, lipids, haemoglobin, melanin etc.) that would absorb radiation in living tissues [Da Silva, 2013; Tuchin, 2000; Tuchin et al., 2006; Vo-Dinh, 2003; Wang et al., 2002]. Absorption of light provides a diagnostic role such as the spectroscopy of a tissue. Absorption can provide information on the chemical composition of a tissue, and serve as a mechanism of optical contrast during imaging. For an absorbing medium, the Absorption coefficient (μ_a), (expressed as unit cm^{-1}) is described as the loss of intensity of a collimated beam through a medium of thickness, l. This is expressed by the Beer-Lambert law,

$$I = I_0 e^{-\mu_a l} \tag{2.1}$$

where I_0 is the incident intensity and I is the transmitted intensity. In other words, μ_a is the reciprocal of the Absorption length (l_a), which is the typical distance travelled by photons before they are absorbed in the medium ($\mu_a = 1/l_a$).

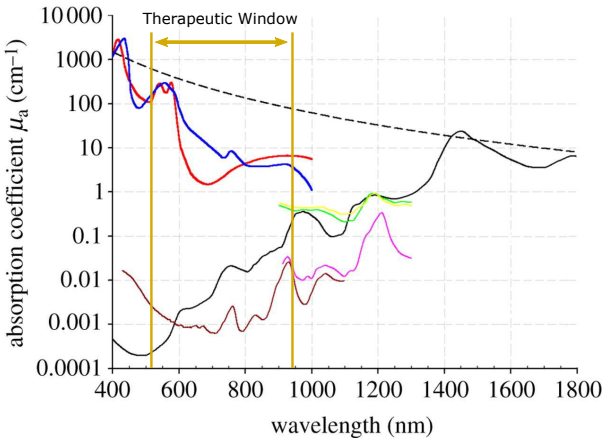

Figure 2.1: Absorption Spectra of the major chromophores making up biological tissue; Oxyhaemoglobin (HbO_2) (red), Deoxyhaemoglobin (Hb) (blue), Water (black), Lipid (brown), Melanin (pink), Collagen (green) and Elastin (yellow) [Beard, 2011].

2.2.2 *Scattering*

However, tissues are strongly scattered in NIR range due to the presence of inhomogeneities in the anatomy (cell organelles, vasculature etc.), defined by the Refractive index (n), which pose a problem of obtaining clear images. But scattering is an important optical property of tissues as it provides feedback (by collecting the backscattered light) during therapy

and has diagnostic value (depending on the ultra-structure of the tissue). For a scattering medium, the Scattering coefficient (μ_s), (expressed as unit cm^{-1}) is described as the probability of transmission of a photon without redirection by scattering after a unit path-length L (units in cm). In other words, μ_s is the reciprocal of the Scattering length (l_s), which is the typical distance travelled by photons before they are scattered in the medium ($\mu_s = 1/l_s$). In biological tissues, μ_s is in the range $100 - 500 cm^{-1}$ [Cheong et al., 1990; Jacques, 2013]. Biological tissues exhibit both absorption and strong scattering and are considered as opaque or turbid media. The total attenuation incurred by turbid media can be defined by the μ_t, which is the sum of the individual absorption and scattering coefficients [Twersky, 1962],

$$\mu_t = \mu_a + \mu_s \tag{2.2}$$

And the inverse of μ_t is called the Mean Free Path (MFP) between two interactions,

$$\text{MFP} = \frac{1}{\mu_t} = \frac{1}{\mu_a + \mu_s} \tag{2.3}$$

In general, the MFP is the average distance travelled by a moving particle (a photon in our case) between successive impacts (collisions), which modify its direction or energy or other particle properties. In biological tissues, it is approximately $20 - 100 \mu m$ [Gelebart, 1998].

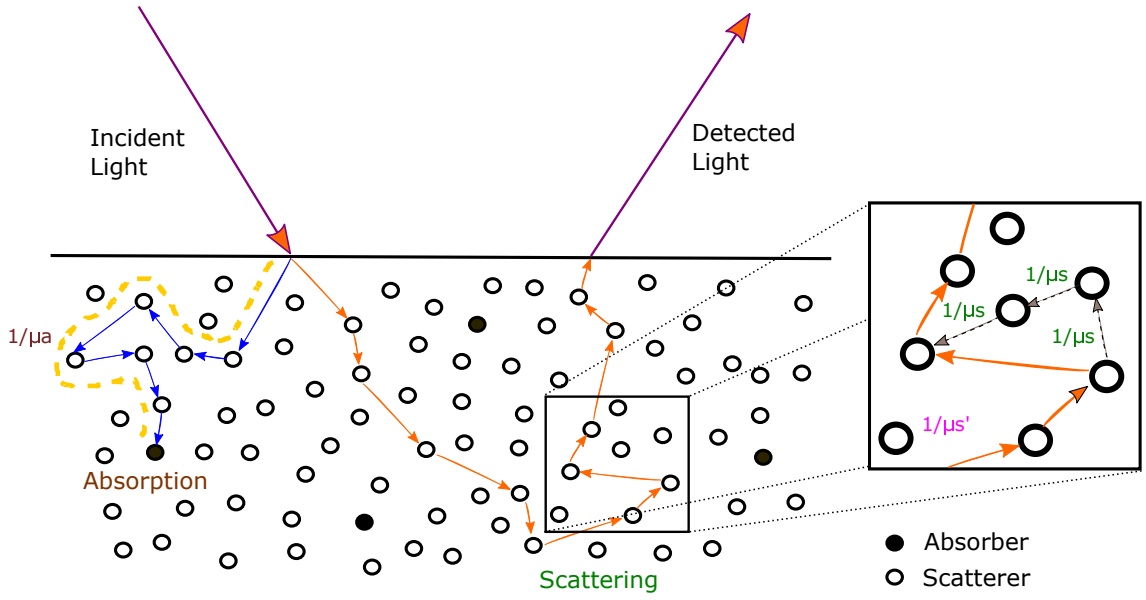

Figure 2.2: Schematic of light-matter interaction in a turbid medium.

A simple schematic of what happens when light hits a turbid medium is represented in Figure 2.2. Scattering of light follows different regimes based on their arrival time in the detector and how far light has penetrated into the medium: the ballistic, transition or random-walk step regimes. Ballistic transport is observed when the MFP of the photon is longer than the dimension of the medium through it travels. These photons are the first to arrive in the medium and they travel in the direction of the incident beam. They undergo only single scattering events and retain their initial state of polarization. Transition regime is the intermediate process where the number of scattering events increase before reaching

the diffusive or random walk regime. These photons have a longer path length than ballistic photons, and their polarization state depends on the number of scattering events they have undergone. They still retain their initial direction of propagation and coherence information. In the random walk regime, the initial propagation direction has been completely randomized and photons undergo multiple-scattering events. The path length, coherence information, propagation direction and polarization state is completely lost in this regime. The multiple-scattered photons still carry information about the structure of the medium and is the 'deepest' we can probe in a tissue.

2.2.3 *Anisotropy*

Considering the case of elastic scattering, the probability of an incident photon in a direction Ω', to scatter in a direction Ω is given by the scattering phase function, $f(\Omega, \Omega')$. This phase function is mainly dependent on the size of the particle in relation to the wavelength, and is not always constant depending on the scattering angle. This translates to a scattering distribution. In a multiple-scattering process, the direction of propagation is described by the Anisotropy factor (g), which is a measure of the amount of forward direction retained after a single scattering event illustrated in Fig. 2.3. It can be mathematically represented as,

$$g = <\cos\theta> = \int_{-1}^{1} f(\cos\theta)\partial(\cos\theta) \tag{2.4}$$

which is the expectation value of $\cos\theta$. Most biological tissues are highly forward scattering, and have values of g in the range of $0.8 - 1$ [Cheong et al., 1990; Jacques, 2013].

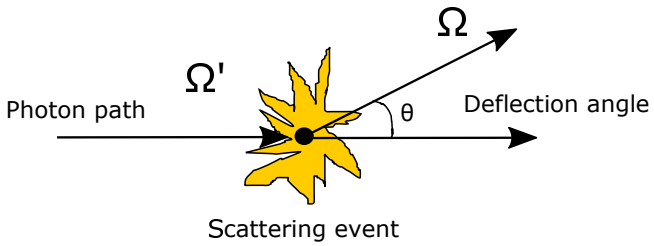

Figure 2.3: Schematic of a scattering event which causes a deflection angle, θ, from the original forward trajectory of the photon. Ω is the direction of propagation of photon and Ω' is the deflected direction of photon after scattering at an angle of $\cos\theta$.

2.2.4 *Transport Mean Free Path (MFP′)*

Another important unit is the 'Transport Mean Free Path (MFP′)' or 'random-walk step' which corresponds to the typical distance travelled by photons before their direction is randomized, and corresponds to a scattering parameter, μ_s', known as the Reduced scattering coefficient (μ_s') (also, $\text{MFP}' = 1/\mu_s'$).

In general, in the red-NIR tissues have a high μ_s' and a low μ_a; which means a photon is likely to undergo many scattering events before being absorbed. In the multiple scattering

regime, the light received by each particle comes from scattered light from other particles located before (or even after) and sometimes far from the initial propagation direction. After multiple-scattering events, photons will travel almost equally in all directions so the diffusion approximation to the Radiative Transfer Equation (RTE) (discussed in Section 2.4) can be utilized. The anisotropy dependent μ_s of the medium can be replaced by an equivalent isotropic Reduced scattering coefficient (μ_s') (in the diffusion regime), given as,

$$\mu_s' = \mu_s(1-g) \tag{2.5}$$

And, the MFP′ (typically $\sim 500\mu m$ in biological tissues) can be further represented as,

$$\text{MFP}' = \frac{1}{\mu_s'} = \frac{1}{\mu_s(1-g)} \tag{2.6}$$

2.3 POLARIZATION BASICS: DEFINITIONS AND THEORY

After reviewing the interaction of light-matter, it is very important to understand the role of the polarization property of light and how it fits into the concepts discussed in Section 2.2. For this purpose, we shall begin with the basics of polarization described by the electro-magnetic formalism.

2.3.1 *Concept of Polarization*

The state of polarization or light polarization refers to the pattern described by the electric field of the light wave as a function of time at a fixed point in space. To understand polarization mathematically, let us consider a plane wave travelling along the z-axis, with wavelength λ and frequency f,

$$\vec{E}(z,t) = E_0 \cos(kz - \omega t) \tag{2.7}$$

where $\vec{E}$ is the electric-field vector, E_0 is the electric-field amplitude, $k = 2\pi/\lambda$ and $\omega = 2\pi f$. When $\vec{E}$ oscillates in a direction parallel to the direction of the propagation of the wave, the light is said to be linearly polarized and is illustrated in Figure 2.4a.

A linearly polarized wave can be resolved into two mutually orthogonal components, $E_\perp$ and $E_\parallel$ given by,

$$E_0 = E_\perp + E_\parallel \tag{2.8}$$

where $E_\perp$ and $E_\parallel$ have their own phase $\delta_\perp$ and $\delta_\parallel$ respectively (see Figure 2.4b). The phase relationship, between these two components can explain the different states of polarization. If the plane of polarization of the electrical field rotates, the light is said to be elliptically polarized, because the electrical field vector traces out an ellipse at a fixed point in space as a function of time and can be seen in Figure 2.5. The degree to which the ellipse is oval is described by a shape parameter called eccentricity or ellipticity, defined as $\varphi = \arctan(b/a)$.

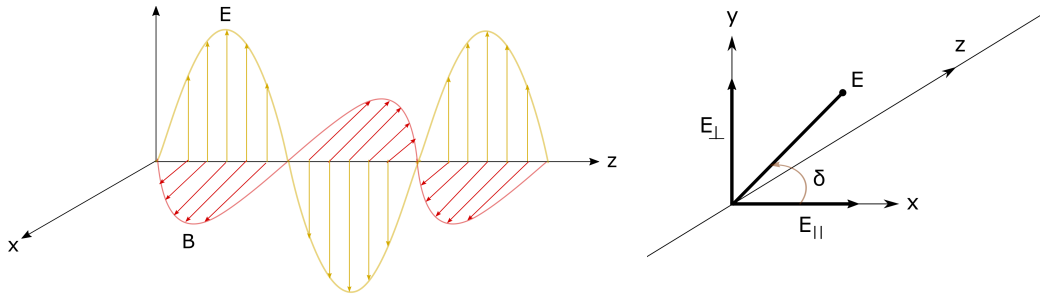

(a) (b)

Figure 2.4: (a) Schematic of a vertically polarized electromagnetic wave with it's Electric-field vector ($\vec{E}$) (yellow) oscillating in the vertical direction. The magnetic field vector, B (red), is always perpendicular to the electric field. (b) $E_{||}$ and $E_{\perp}$ components of the total electric field, $\vec{E}$, where δ is the phase angle of the electric field components.

If the ellipse happens to be a circle (i. e. when ellipticity $\varphi = \pm 45°$), the light is said to be circularly polarized.

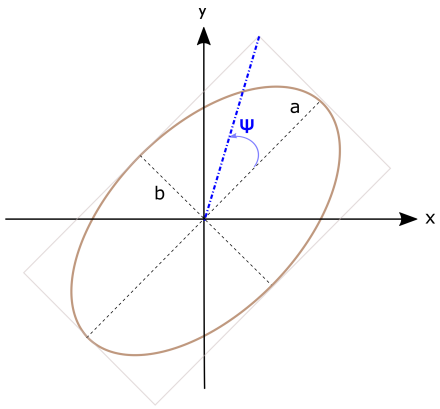

Figure 2.5: Schematic of a polarization ellipse showing the ellipticity, φ, as a function of the semi-major and semi-minor axes, a and b.

There are two orientations of circularly/elliptically polarized light: right-handed (or positive *helicity*), where $\vec{E}$ is rotating clockwise as seen by an observer towards whom the wave is moving, and left-handed (or negative *helicity*), where $\vec{E}$ is rotating counter-clockwise as seen by an observer towards whom the wave is moving. A schematic representation of the handedness of light is represented in Figure 2.6. The connection between phase and polarization can be understood as follows: circularly polarized light consists of equal quantities of linear, mutually orthogonal polarized components that oscillate exactly 90° out of phase.

In general, light of arbitrary elliptical polarization consists of unequal amplitudes of linearly polarized components where the electrical fields of the two polarizations oscillate at the same frequency but have some constant phase difference.

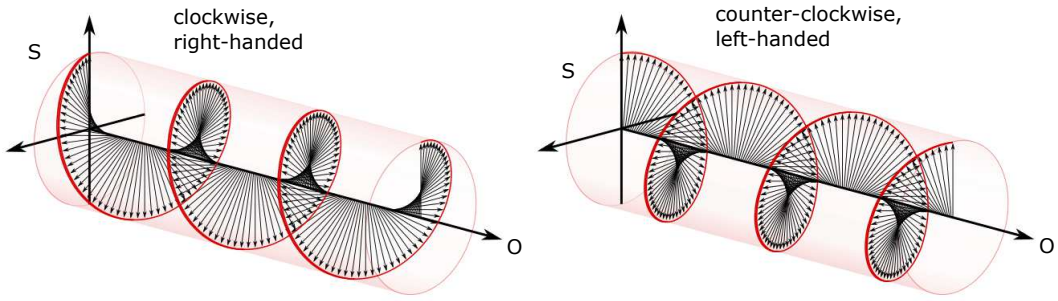

(a) (b)

Figure 2.6: (a) Right-handed circularly polarized light as seen by the observer with $\vec{E}$ rotating clockwise (also called as positive helicity), and (b) Left-handed circularly polarized light as seen by the observer with $\vec{E}$ rotating counter-clockwise (also called as negative helicity). Symbols, O: Observer and S: Source.

2.3.2 *Describing the state of polarization*

The different states of polarization can be expressed mathematically in two main schools of representation: Jones calculus and Stokes vectors. The method of Jones is unique in that it deals with the instantaneous electric field, whereas the Stokes parameters describe a time-averaged optical signal. For this reason the Stokes/Mueller method is often chosen for use with light of rapidly and randomly changing polarization state, such as natural sunlight, while the Jones method is preferred when using coherent sources such as lasers.

2.3.2.1 *Jones Calculus*

The Jones method, introduced by R. C. Jones [Jones, 1941] in 1941, provides a mathematical description of the polarization state of light, as well as a means to calculate the effect that an optical device will have on input light of a given polarization state. Since light is composed of oscillating electric and magnetic fields, the most natural way to represent light is in terms of the Electric-field vector ($\vec{E}$). The column vector representation of $\vec{E}$ is known as a *Jones Vector*, given by,

$$\vec{E} = \begin{bmatrix} E_{\parallel} \\ E_{\perp} \end{bmatrix} = \begin{bmatrix} E_{0\parallel} e^{i\delta_{\parallel}} \\ E_{0\perp} e^{i\delta_{\perp}} \end{bmatrix} \tag{2.9}$$

where $E_{\parallel}$ and $E_{\perp}$ contain both amplitude and phase information. Any state of polarization can be described by a two-element Jones vector, and the linear operation of any optical device can be fully described by a 2x2 Jones matrix, given by,

$$\begin{bmatrix} E_{\parallel,t} \\ E_{\perp,t} \end{bmatrix} = \begin{bmatrix} a & b \\ c & d \end{bmatrix} \begin{bmatrix} E_{\parallel,i} \\ E_{\perp,i} \end{bmatrix} \tag{2.10}$$

where the 2x2 matrix in the LHS of Eqn. 2.10 is called the *Jones matrix* of the optical device (linear polarizer, quarter-wave plate, etc.). It is possible to represent the passage of a beam of light through multiple devices as the multiplication of Jones matrices. The Jones vector is only valid in the space of fully polarized light, and is only useful for problems involving

coherent light. In our studies, the main focus is on retaining light that has kept its polarization and removing the depolarized light, we have to deal with characterizing light which is fully, partially polarized or even unpolarized. Thus, we concentrate on using the Stokes Vector formalism which is designed for this purpose.

2.3.2.2 *Stokes Vectors*

In the Stokes formalism which was introduced by G. G. Stokes in 1852 [published in Stokes, 1901], the polarization state of the light beam is represented by four measurable quantities: I representing the overall intensity of the light source, Q and U representing the linear polarized components and V representing the circularly polarized component. These parameters grouped in a 4x1 vector is known as the *Stokes Vector*. These Stokes parameters are described by one of the following intensity measurements performed using ideal polarizers: $I_{\parallel}$, $I_{\perp}$, I_{45°, I_{135°, I_R and I_L and can be represented as,

$$S = \begin{bmatrix} I \\ Q \\ U \\ V \end{bmatrix} = \begin{bmatrix} I_{\parallel} + I_{\perp} \\ I_{\parallel} - I_{\perp} \\ I_{45^\circ} - I_{135^\circ} \\ I_R - I_L \end{bmatrix} \tag{2.11}$$

From the Stokes Vector, different polarization parameters can be defined [Bickel and Bailey, 1985; Chipman, 1994; Collett, 1990; Kliger et al., 1990]. Degree of Polarization (DOP), represented as,

$$DOP = \frac{\sqrt{Q^2 + U^2 + V^2}}{I} \tag{2.12}$$

The DOP varies from 0 to 1, where a fully polarized state will have a DOP of 1, a completely unpolarized state will have a DOP of 0 and a partially polarized state will have intermediate values. Other important quantitites are also defined using the Stokes Vector, called the Degree of Linear Polarization (DOLP) and Degree of Circluar Polarization (DOCP), written as,

$$DOLP = \frac{\sqrt{Q^2 + U^2}}{I} \tag{2.13}$$

and,

$$DOCP = \frac{V}{I} \tag{2.14}$$

respectively. DOCP can have positive or negative values which is an indicator of the handedness of the circulary polarized light. The DOP should not exceed unity and should satisfy the condition,

$$I \geqslant \sqrt{Q^2 + U^2 + V^2} \tag{2.15}$$

The Stokes Vector summarizes the representation of the polarization state of light, and is used in conjugation with a 4x4 matrix, known as the *Mueller Matrix* [Mueller, 1943] to describe the transfer functions of any medium with its interaction with polarized light.

$$S_0 = MS_i \tag{2.16}$$

where S_i and S_0 are the Stokes vectors of the input and output light, respectively. It is also possible to represent multiple incoherent light sources travelling in the same direction, by a common Stokes vector,

$$S = \sum S_i \tag{2.17}$$

The Mueller matrix is also called as the complete "Optical Polarization Fingerprint", as all the polarization properties of the medium is represented in one of it's 16 elements. It is also possible to represent the polarization ellipse, in turn the Stokes parameters in Three-dimensional (3D) cartesian coordinates using the *Pointcaré Sphere* (introduced by H. Pointcaré in 1892 [Pointcaré, 1892]). Figure 2.7 shows the graphical representation of the Pointcaré sphere, along with a few examples of fully-polarized states and their locations on the surface of the sphere.

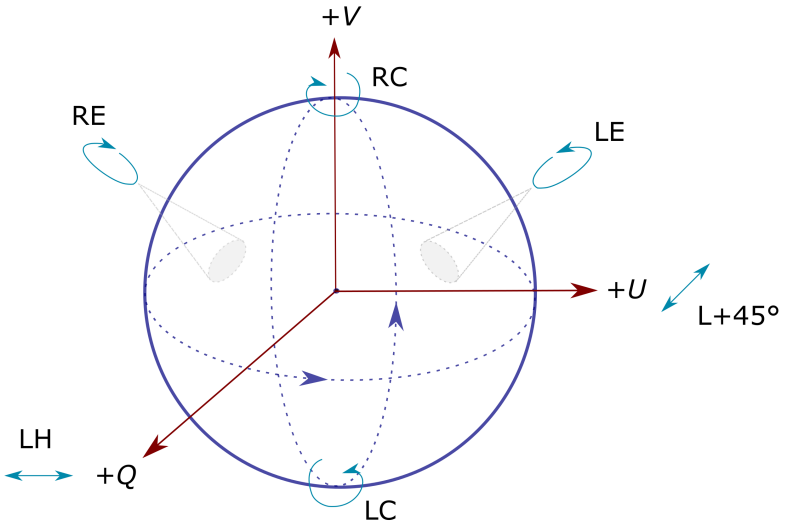

Figure 2.7: Schematic of the Pointcaré Sphere with it's correlation to the Stokes Parameters (Q, UandV). Examples of different fully polarized states and their corresponding locations on the sphere are also represented where, LH: linear horizontal, L+45°: linear +45°, RC: right circular , LC: left circular, RE: right elliptical and LE: left elliptical polarizations respectively.

A single point in the sphere represents a polarization state, and all possible states exist within a sphere of unit radius. The points on the sphere's surface represent all fully-polarized states, and the points that lie within the sphere represent partially-polarized states.

2.4 POLARIZED LIGHT INTERACTIONS WITH SCATTERING MEDIA

The polarization effects of light propagation through various multiply-scattering media, including biological tissues, are fully described by the Vectorial Radiative Transfer Equation (VRTE).

2.4.1 *Vectorial Radiative Transfer Equation (VRTE)*

The transport of light through a medium containing many scattering particles is a complex problem and there is a need to represent this formalism mathematically and with a general solution that will account for all types of interactions. The Radiative Transfer Equation (RTE) serves this purpose efficiently with the calculation of radiance and in turn measures the propagating intensity however, it does not account for polarization property of the propagating light intensity [Chandrasekhar, 1960].

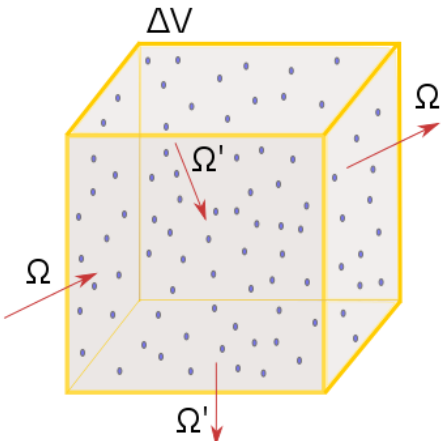

Figure 2.8: Schematic of radiance along a direction Ω, of a volume element ΔV. The total change in radiance is given as a result of losses due to absorption, gains due to incoming scattering from all directions Ω′ into direction Ω and losses due to scattering in all directions.

For a given volume ΔV (as shown in Figure 2.8), if an initial incident radiance $L(r, \Omega, t)$ (with units $Wm^{-2}sr^{-1}$) propagates a distance Δr in a direction Ω, at a time t, and velocity $v = c/n$,the RTE can be written as,

$$\frac{1}{v}\frac{\partial L(r,\Omega,t)}{\partial t} + \bigtriangledown.L(r,\Omega,t)\Omega = -\mu_t L(r,\Omega,t) + \mu_s \int L(r,\Omega',t) f(\Omega,\Omega')\partial\Omega' + S(r,\Omega,t) \tag{2.18}$$

where $S(r, \Omega, t)$ represents the spatial and angular distribution of photons added by a source inside the medium. The RTE is a linear solution which uses the law of energy conservation and accounts for any change in the propagating radiance. The left-hand side of Equation. 2.18 represents the total change in the radiance during light transport through the volume ΔV at a velocity v in the medium, where the first term corresponds to the

rate of change between movement of photons in and out of the volume and the second term corresponds to the flux of photons along direction Ω. On the right-hand side, the interactions of the photons within the volume is described where: the first term represents the losses due to the total attenuation, i.e. absorption and scattering losses, the second term represents the portion of photons that further scatter to its neighbouring volumes, calculated by the scattering phase function $f(\Omega, \Omega')$ which represents the probability of scattering the volume along each direction Ω' into direction Ω, and the third term corresponds to the portion of photons retrieved due to source gains inside the medium.

While this gives a solution to the scalar transport problem, it is based on the assumption of employing a non-polarization dependent scattering phase function. Even with the use of an unpolarized source, scattering itself might generate partially polarized light. Also, for the case of using a polarized light source, or illuminating a medium with polarized light, the radiance and polarization of light leaving the medium is not a scalar quantity, but a complex vectorial one. To address these problems, we use a modified form of the RTE called the Vectorial Radiative Transfer Equation (VRTE) [Ishimaru, 1978] and with the inclusion of four different radiances, one for each of the Stokes vectors. The VRTE can be represented as,

$$\frac{1}{v}\frac{\partial \vec{I}(r,\Omega,t)}{\partial t} + \bigtriangledown.\vec{I}(r,\Omega,t)\Omega = -\mu_t \vec{I}(r,\Omega,t) + \mu_s \int \vec{I}(r,\Omega',t) Z(\Omega,\Omega') \partial\Omega'. \\ +S(r,\Omega,t) \tag{2.19}$$

Here, $\vec{I}$ is a vector containing the four radiances corresponding to the four Stokes vectors and is represented as,

$$\vec{I} = \begin{bmatrix} I(r,\Omega,t) \\ Q(r,\Omega,t) \\ U(r,\Omega,t) \\ V(r,\Omega,t) \end{bmatrix} \tag{2.20}$$

where I, Q, U and V represent each intensity of their respective elements of the Stokes Vector. The scattering phase function $f(\Omega, \Omega')$, has been replaced by a 4x4 matrix, Z which represents the scattering Mueller-matrix of the volume, that transform incoming intensity along direction Ω' into the direction Ω.

Solving the VRTE has always known many challenges since it was derived, and one of the most common approaches of solving the problem is through Monte-Carlo simulations. Although this part has not been worked on during this thesis, it is important to be aware of the assumptions and solutions that have been used in some of the experiments.

2.5 POLARIZED LIGHT IMAGING OF BIOLOGICAL TISSUES

Polarimetry has a long and successful history in various forms of clear media. Driven by their biomedical potential, the use of the polarimetric approaches for biological tissue assessment has also recently received considerable attention. Specifically, polarization can be

used as an effective tool to discriminate against multiply scattered light (acting as a gating mechanism) in order to enhance contrast and to improve tissue imaging resolution. Moreover, the intrinsic tissue polarimetry characteristics contain a wealth of morphological and functional information of potential biomedical importance. However, in a complex random medium-like tissue, numerous complexities due to multiple scattering and simultaneous occurrences of many scattering and polarization events present formidable challenges both in terms of accurate measurements and in terms of analysis of the tissue polarimetry signal. In order to realize the potential of the polarimetric approaches for tissue imaging and characterization/diagnosis, numerous work is being done to find innovative solutions to these challenges.

Some inroads in biomedical polarimetry have been made in the context of optical imaging, specifically using polarization gating to separate out and potentially remove the multiply scattered (depolarized) component of the light beam to either observe the glare from the air/skin surface and surface details (or to suppress it for a better view the deeper subsurface tissue structures) [Jacques et al., 2000; Morgan and Stockford, 2003]. A widely used technique is the detection via the cross-linear imaging channel to get rid of the mirror reflections, for tissues examination, which was suggested by Anderson [1991]. Jacques et al. [2002] modified this scheme further for high resolution imaging of the texture of the superficial (sub-surface) skin structures, whose measurements were sensitive to depths greater than 300 $microns$. In this approach, the glare from the air/glass/skin interfaces was removed through optical coupling (using index matching liquid) of a glass plate in contact with the skin and by off-normal illumination. A simple system was developed and used in clinics to image skin cancer where the tissue is illuminated with linearly polarized light, and two images are acquired in parallel and orthogonal polarization channels [Ramella-Roman et al., 2004]. The multiply scattered photons were filtered out by extracting the polarization preserving component of the scattered light employing either the polarization difference scheme (also called Linear Polarization Difference Imaging (LPDI)),

$$\text{LPDI} = I_{\parallel} - I_{\perp} \tag{2.21}$$

or the DOP scheme;

$$\text{DOP} = \frac{I_{\parallel} - I_{\perp}}{I_{\parallel} + I_{\perp}} \tag{2.22}$$

where LPDI and DOP are the polarization component containing images, $I_{\parallel}$ is the image in parallel polarization channel and $I_{\perp}$ is the image in orthogonal polarization channel. An illustration of the kind of images obtained with a DOP image is shown in Figure 2.9. It is evident from Panel (d) that DOP image is very different from the other channels and emphasizes the scattering of incident polarized light by the superficially located burn scar.

DOP imaging has some advantages over LPDI; as DOP imaging is relatively insensitive to spatial variation of illuminating light and variations in pigmentation. This can be explained as the DOP image is formed by the ratio of the numerator (primarily comprised of superficial sub-surface reflectance) and the denominator (representative of total subsurface reflectance). Linear polarization gating was made popular by Schmitt et al. [1992],

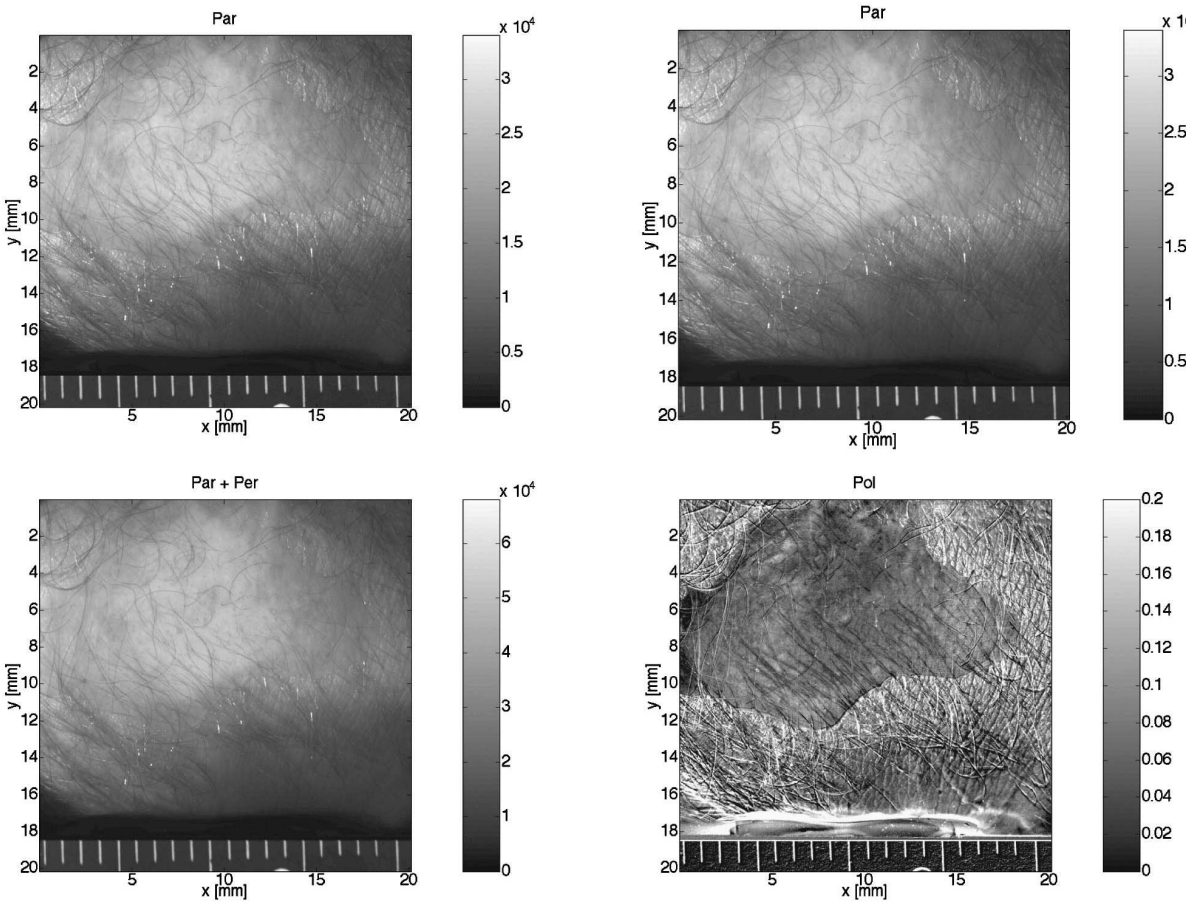

Figure 2.9: Images of skin burn scar illustrated in Jacques et al. [2002] with (a) Linearly polarized parallel image intensity ($I_{\parallel}$) image (denoted as 'Par'), (b) Linearly polarized orthogonal image intensity ($I_{\perp}$) image (denoted as 'Per'), (c) $I_{\parallel} + I_{\perp}$ image (denoted as 'Par + Per'), and, (d) DegreeofPolarization(DOP) image (denoted as 'Pol' in this figure).

Demos and Alfano [1997] and Demos et al. [2000], but is still limited to the surface examination of tissues.

Morgan and Stockford [2003] developed another elegant polarization scheme for eliminating surface reflection in backscattering imaging of superficial tissue layers, obviating the use of index optically flat plates (and index matching fluid) and angled illumination (thus enabling co-axial detection). It was shown that a suitable combination of co- and cross-polarized images acquired using linear and circular polarization illumination can be used to simultaneously filter out both the multiply scattered light and the surface reflection. Demos and Alfano [1997] and Demos et al. [2000] developed a methodology based on both spectral and polarization discrimination of backscattered photons for deep sub-surface imaging of tissue. This approach, known as spectral polarization difference imaging, exploits the difference in light penetration of different wavelengths in combination with polarization filtering for selectively imaging different tissue depths. Polarization imaging was also used to perform spectroscopy as shown by Backman et al. [1999] and Bartlett and Jiang [2002] to extract surface features. Another approach that was demonstrated recently [Georges et al., 2007], was the application of a new principle of selective

cancellation of scattering, by the control of properties of polarization. By cleverly adjusting the angles between a polarizer (to linearly polarize the incident beam), and an optical retarder (quarter-wave plate), it is possible to obtain a) the cancellation of the volume scattering for better surface visualisation; b) the cancellation of surface scattering to visualize the scattering volume.

Intrinsic polarimetry exploits morphological, biochemical, and functional information that can be used for non-invasive and quantitative tissue diagnosis [N. Ghosh and Vitkin, 2010], [M. F. G.Wood and Vitkin, 2010] and [McNichols and Coté, 2000]. Measuring the polarization maintaining signal is very important for either of these applications, accurate measurement of the polarization retaining signal is extremely important and many of the traditional polarimetry systems are not suitable for biological tissue examination, i. e. to study thick tissues that undergo multiple scattering. This multiple-scattering leads to depolarization of light, creating a large depolarized source of noise that hinders the detection of the information-carrying polarization signal (which is usually very small). To overcome these problems, methods that measure Stokes vector of the light (Stokes vector polarimeter) and/or the Mueller matrix of the sample (Mueller matrix polarimeter) can be used. Further, the linear polarization gating technique has advanced with the development of Mueller imaging systems which provides the most complete spatial polarimetric characterization of biological tissues (see Section 2.3.2) [Falconet et al., 2008; Liu et al., 2005]. This Mueller matrix can be interpreted in terms of depolarization, retardance (amount and orientation) and polarizance which translate to tissue properties. Other important biomedical applications include: diagnosis of skin lesions [Jacques, 1999; Kapsokalyvas et al., 2013; Stockford and Morgan, 2005], colon [Antonelli et al., 2010; Pierangelo et al., 2011], uterine cervix [Anastasiadou et al., 2008; Pierangelo et al., 2013; Shukla and Pradhan, 2009]. In addition to the classical intensity image, the Mueller matrix contains information on birefringent, dichroic, or depolarization properties of the tissue, In particular cases when there is a priori knowledge regarding the tissue investigated (i. e. targeted composition or expected structure, degree of alignment, etc.), measurement of subsets of the Mueller-matrix elements could provide useful information. Various techniques based on Mueller-matrices, such as orthogonal polarization or differential polarization have been used successfully for differentiating between normal and diseased tissue. However, the design of high end polarimetric fibers (internal end fiber) for Mueller imaging systems still remains a technical challenge. There is also very less depth information about the tissue sample with this technique. The quest for a technique capable of being sensitive to depth information as well as deterring the consequences of polarization in tissues (like depolarization, multiple scattering etc.) has become significant.

The underlying principle for polarization gating as a depth selective technique is based on the fact that (see Section 2.2) – the photons which are scattered (or re-emitted) from deeper tissue layers undergo multiple scattering events and are depolarized to a larger extent. Polarization gating thus effectively selects photons which have not travelled beyond a few scattering mean free paths (1 MFP $\sim$ 100µm in tissue). For examining tissues deeper than in linear polarization gating methods, Morgan and Stockford [2003] introduced the use of circular polarization and demonstrated that subtraction of images taken in co-circular illumination/detection configuration and cross-linear illumination/detection

allowed for the extraction of weakly scattered light and the elimination of specular reflected photons. Due to the effect of '*polarization memory*' [MacKintosh et al., 1989; Morgan and Ridgway, 2000], the depth probed by the circular polarization is larger than that with linear polarization. In this context, we introduce the use of elliptical polarization to access volumes that are probed intermediate to linear and circular polarization. This technique can probe tissues deeper than linear polarization, and is the basis of why we choose to explore the behaviour of circular and elliptical polarization with respect to the penetration depth in this thesis.

The propagation of light in a scattering medium is accompanied by a loss of polarization due to multiple interactions between the electromagnetic field and scatterers, resulting in changes of amplitude and direction of the field [Bicout and Brosseau, 1992; Bicout et al., 1994; MacKintosh et al., 1989; Tuchin, 2000; Yoo and Alfano, 1989]. The use of polarizing filters allows, up to a point, selecting photons for which polarization state is maintained: this is the basis of the polarization gating imaging methods. It is understood that beyond a certain optical thickness, depending on the number of scattering events, anisotropy factor, and also absorption, photons will completely lose memory of their initial polarization - as was demonstrated by MacKintosh et al. [1989]. This effect describes how the original polarization is maintained during a number of scattering events for a given polarization and showed that the polarization of circularly polarized light is indeed maintained through a larger number of scattering events than that of linearly polarized light. It is shown that this effect depends mainly on the size the scattering particle, i. e. the Anisotropy factor (g). Since biological tissues are Mie scatterers [Tuchin, 2000], this filtration with circularly polarized light can indeed be achieved in tissues, allowing a deeper screening than linearly polarized light. If the particles are very small (Rayleigh scattering), the opposite occurs, due to the numerous changes of helicity of circular polarization with multiple reflections. This concept has been used in various areas of research to locate or analyse specific regions in samples. Schmitt et al. [1992] used these advantages in transmission image acquisition geometry, using a point-illumination system, in which only the circularly polarized light is detected. Morgan and Ridgway [2000] conducted these experiments on circular polarization maintaining photons in reflection geometry, which is more suitable for screening biological tissue *in vivo*. They also demonstrated that, with linear polarization, a maximum DOP is measured when the optical thickness is minimal – which meant an increase in scattering results in a decrease of DOP. However, for circular polarization, a maximum DOP is obtained beyond the minimum optical thickness, thus showing that a detection based on circular polarization selection will probe a sub-surface region from the surface itself. To probe further in examining the behaviour of different polarization states and to confirm the reasoning behind the "polarization memory" effect presented by MacKintosh et al. [1989], Hielscher et al. [1997]; Rakovic et al. [1999] and Wang and Wang [2002] analysed the 2D spatial distribution of backscattered light and verified the effect of size of the scatterers on the polarization of the backscattered light.

After a thorough consideration of all the important polarization gating techniques for biological tissues, we can conclude they did not provide satisfactory depth resolution of tissue at the mesoscopic scale (sub-surface areas). In general, two types of polarization gating techniques have been developed so far – a) Localisation and characterisation of optical

properties; b) Imaging of superficial/surface tissues. Among these techniques, the works of Morgan and Stockford [2003] seems particularly interesting as it eliminates both, the specular reflection of the sample without special preparation (as in [Jacques et al., 2002, 2000]) and also the multiple-scattered photons. And thus we have adopted Morgan and Stockford [2003]'s techniques and in addition, we introduce the novel idea that it is possible to select the probed depth as a function of the polarization ellipticity. Thus allowing screening the tissue at any specific depth ranging between the surface and a maximum depth defined by the maximum penetration depth of the circularly polarized photons.

2.6 PREVIOUS RESULTS AND CONCLUSIONS

This thesis is based on some concepts and results previously published by research group DiMABio, in Institut Fresnel, Marseille [Da Silva et al., 2012; Rehn, 2012; Rehn et al., 2013].

For the purpose of studying elliptically polarized light transport in biological tissues, a substantial reference Monte Carlo code was adapted. In the study, a quaternion Monte Carlo code developed by Ramella-Roman et al. [2005] was modified to account for Fresnel reflections at the surface. The Monte Carlo study verified that using different polarization ellipticities allowed probing at different depths. The code was implemented for a range of optical properties ($\mu_s = 10$ to $200 cm^{-1}$, $\mu_a = 0.5$ to $5 cm^{-1}$ and $g = 0.05$ to 0.95) (mostly Mie scattering regime and also approaching Rayleigh scattering regime) in a semi-infinite medium (with refractive index,$n = 1.4$) to obtain depth information and was found to be reliable with a limited calculation time. It is to be noted that for illumination, a point source was assumed. An example of optical imaging system for producing different polarization illuminations and measuring backscattered intensity from biological tissues is illustrated in Figure 2.10.

The calculated depth sensitivity in biological tissues, totally depends on the optical properties and the ellipticity of the polarization illumination used. The Mean Visitation Depth (MVD) which is a measure of the volume probed by the detected backscattered photons [Tseng et al., 2009] and has all the depth information and its measurement was significant. This method provided a link between the measured backscattered intensity and probed depth with the introduction of two quantities: Z_c, which is a probed depth-descriptor (in terms of MVD) and R_c, which denotes the radial extension of the backscattered signal. It was found that these two quantities were correlated linearly no matter the polarization channel used and could be summarized mathematically as,

$$Z_c \approx \frac{R_c}{3} + (3[\mu_a + (1-g)\mu_s])^{-1} \tag{2.23}$$

By analyzing the morphology of the backscattered polarized signals, it is possible to retrieve the optical properties and hence it is also possible to estimate the Transport Mean Free Path (MFP′) for the sample. Figure. 2.11 summarizes the Mean Visitation Depth (MVD) for different ellipticities that was calculated by Rehn et al. [2013] to illustrate that po-

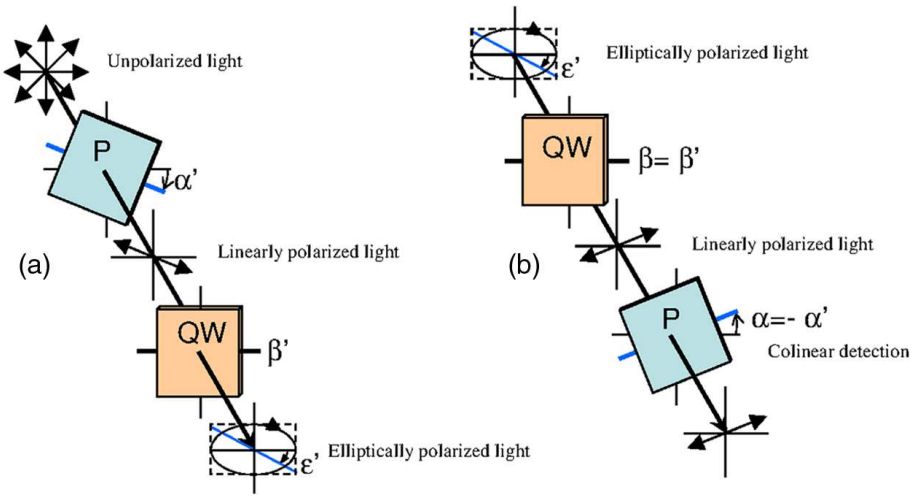

Figure 2.10: Optical imaging system with linear polarizers (P) and quarter-wave plates (QW). (a) Generation of the elliptically polarized light in the illumination path. (b) Analysis of elliptically polarized light in the detection path. The polarization ellipse of the illumination and the detection can be described by the rotation angles α and α' of the horizontal axis of the linear polarizer and the rotation angle β and β' of the fast axis of the quarter-wave plate. The ellipticities ϵ and ϵ' are defined by $\epsilon = \beta - \alpha$ and $\epsilon' = \beta' - \alpha'$. Copolarization detection is obtained for $\alpha = \alpha'$, $\beta = \beta'$ and $\epsilon = \epsilon'$.[Rehn et al., 2013]

larization maintaining channels will probe volumes larger as the polarization ellipticity increases.

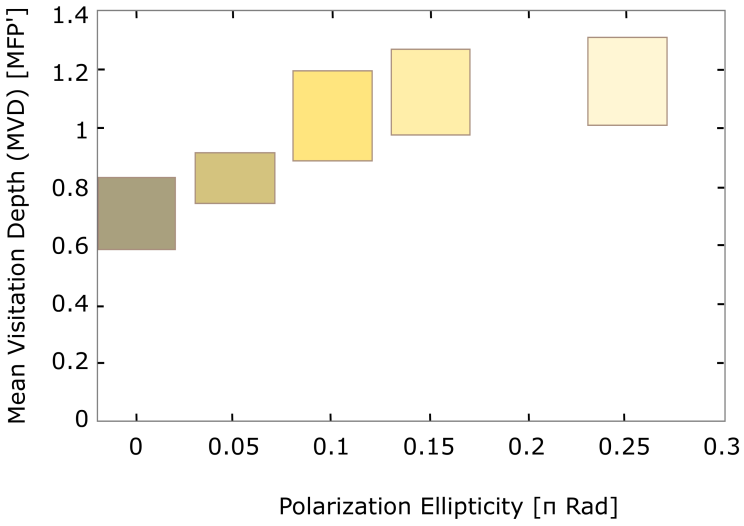

Figure 2.11: Probed depth or Mean Visitation Depth (MVD) as a function of the polarization ellipticity as calculated by Rehn et al. [2013]. The data represents a range of values of probed depth that was calculated and depends on the optical property in question.

The depths are denoted not by single values, but by a range that depends solely on the anisotropy factor and regime of scattering that is in question. In conclusion, it was demonstrated that there is a relationship between the depth probed and the radial extension of

detected back-scattered intensity. Although this was already studied for linear polarization [Liu et al., 2005], this method validates the relationship for all types of incident polarization. Moreover, it was also shown that the depth descriptor, Z_C varied as a function of ellipticity. This forms a stepping stone to analyze the inverse problem of localizing structures in biological tissues.

3

POLARIZATION GATING IMAGING USING ELLIPTICALLY POLARIZED LIGHT

This chapter describes the use of elliptical polarization gating with incoherent light, experimental set-up and the method developed involving co- and counter-elliptically polarized light to probe sub-surface volumes. The principle is validated with phantom experiments on Intra-lipid® and *ex vivo* tissue. The extent of this method is also substantiated with *in vivo* experiments on human skin.

3.1 USING ELLIPTICALLY POLARIZED LIGHT FOR POLARIZATION GATING

Elliptical polarization has seldom been used in polarization gating, but has been catching up especially in the field of optical biopsy [Kunnen et al., 2015]. This form of polarization gating has two reasonable advantages over linear polarization gating (see Figure 3.1): a) it undergoes a change in helicity by reflection, which eliminates the specular reflection through co-elliptical detection; b) Also, elliptically polarized light retains its polarization state for a larger number of scattering events than that of linearly polarized light.

We propose to take advantage of using elliptically polarized light as it allows for more selective probing in terms of depth instead of using the conventional linearly polarized illumination. Co-elliptical measurements allow access to deeper sub-surface volumes than co-linear measurements, where the depth of probing is controlled by the ellipticity of incident polarization. Counter-elliptical measurements attenuate the sub-surface signal and, hence, enhance the signal coming from deeper volumes, provided that mirror reflections are filtered. We propose a new protocol of polarization gating data-acquisition that combines co-elliptical and counter-elliptical measurements. For the purpose of illustrating different modes of application, series of *in vivo* measurements were performed on volunteers' skin abnormalities. Here the main focus is on removing background information, accessing sub-surface information and to illustrate the selective probing in depth.

Figure 3.1 describes the types of photons acquired when polarized light is illuminated linearly or elliptically. Based on previous works [Da Silva et al., 2012; Feng et al., 2013; Morgan and Ridgway, 2000; Morgan and Stockford, 2003], we adopted the polarization scheme of illumination/detection, with four different imaging channels as shown in Table 3.1.

Some of the recent studies have demonstrated that circularly polarized light is more depolarized in Intra-lipid® [Swami et al., 2013] and tissue samples [Swami et al., 2014] than linearly polarized light. The depolarization factor or DOP, which is the ratio between the intensity of detected polarized light to the intensity of illuminated polarized light, has not

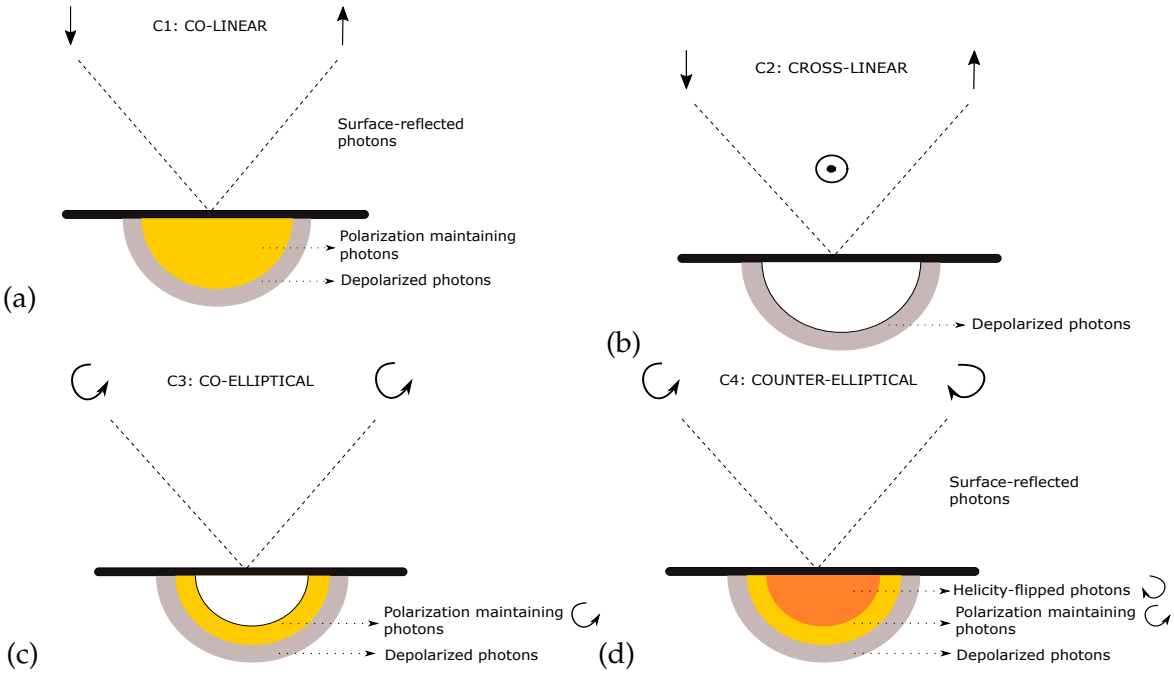

Figure 3.1: Schematic representation of channels used in polarization gating (a) Co-linear channel (C1) (b) Cross-linear channel (C2) (c) Co-elliptical channel (C3) (d) Counter-elliptical channel (C4)

Table 3.1: Back-scattered Photon characteristics measured in different imaging channels.

Channel	Illumination	Detection	Light characteristics
C1	Linear	Linear	Surface-reflected (S_L) + polarization-maintaining(P_L) + multiple-scattered photons (MS_L)
C2	Linear	Cross-linear	Multiple-scattered photons (MS_L)
C3	Elliptical	Co-elliptical	Polarization-maintaining (P_E) + multiple-scattered photons (MS_E)
C4	Elliptical	Counter-elliptical	Surface-reflected (S_E) + multiple-scattered photons (MS_E)

been considered for our studies and only the signal containing polarization-maintaining volume is taken into consideration. The raw signal collected through a given polarization gate, after subtraction of a proper amount of depolarized light, is related to a well defined probing depth, no matter the amount of polarized signal left.

Polarization gating methods concentrate on subtracting the background from the images to improve the polarized signal. In practice, a simple subtraction between co-linear and cross-linear imaging channels, also known as Linear Polarization Difference Imaging (LPDI), allows the separation of the surface contribution from the multiple-scattered

part (coming from deeper volumes), MS_L, resulting in an enhancement of the surface image (S_L+P_L) (See Figure 3.2a and 3.3 (e)).

$$C1 - C2 = P_L + S_L \tag{3.1}$$

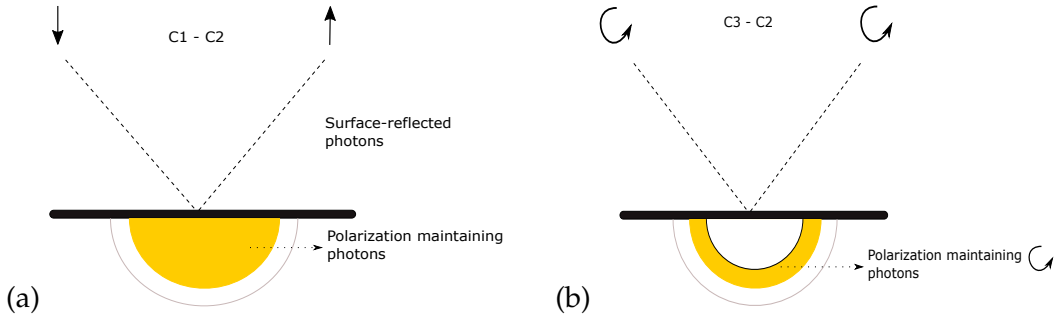

Figure 3.2: Schematic representation of polarization gating using (a) Linear Polarization Difference Imaging (LPDI), i. e. C1-C2, and (b) Elliptical Polarization Difference Imaging (EPDI), i. e. C3-C2.

The resulting image is clearly dominated by the surface reflection, which provides no information about the underlying tissue and distorts conventional polarization images. However, linear polarization gating alone does not allow simultaneous filtering of mirror reflections and multiple-scattered light. To overcome this problem the use of circularly/elliptically polarized light was adopted [Morgan and Ridgway, 2000; Morgan and Stockford, 2003], wherein the cross-linear fraction was subtracted from the co-elliptical images, to access sub-surface volumes (with the assumption that the subtraction nullifies the multiple-scattered photons from both channels and gives only elliptical polarization-maintaining photons, P_E [Jacques et al., 2002]) (See Figure 3.2b and 3.3 (f)).

$$C3 - C2 = P_E \ (when\ S_L = S_E) \tag{3.2}$$

Channel 2 (Figure 3.3 (b)) and Channel 3 (Figure 3.3 (c)) contain no significant surface reflection, and the difference in intensity between them can be attributed to weakly scattered, circularly/elliptically polarized light. This method, also known as Circular/Elliptical Polarization Difference Imaging (EPDI), however, removes an amount of linearly multiple-scattered photons much greater than elliptically multiple-scattered photons. This over-subtraction leads to the loss of some valuable information at the sub-superficial layers.

To overcome this problem and to account for the fact that the multiple-scattered photons arising from linear polarization gating and circular polarization gating are different from each other in fraction, we have devised a new method (referred to as 'Multi-Polarization Difference Imaging (MPDI)' in this manuscript) to nullify and eliminate the background by subtraction. To obtain the polarization-maintaining photons from the elliptical channels, a subtraction between the elliptical channels is performed, to eliminate the elliptically multiple-scattered photons.

$$C3 - C4 = P_E - S_E \tag{3.3}$$

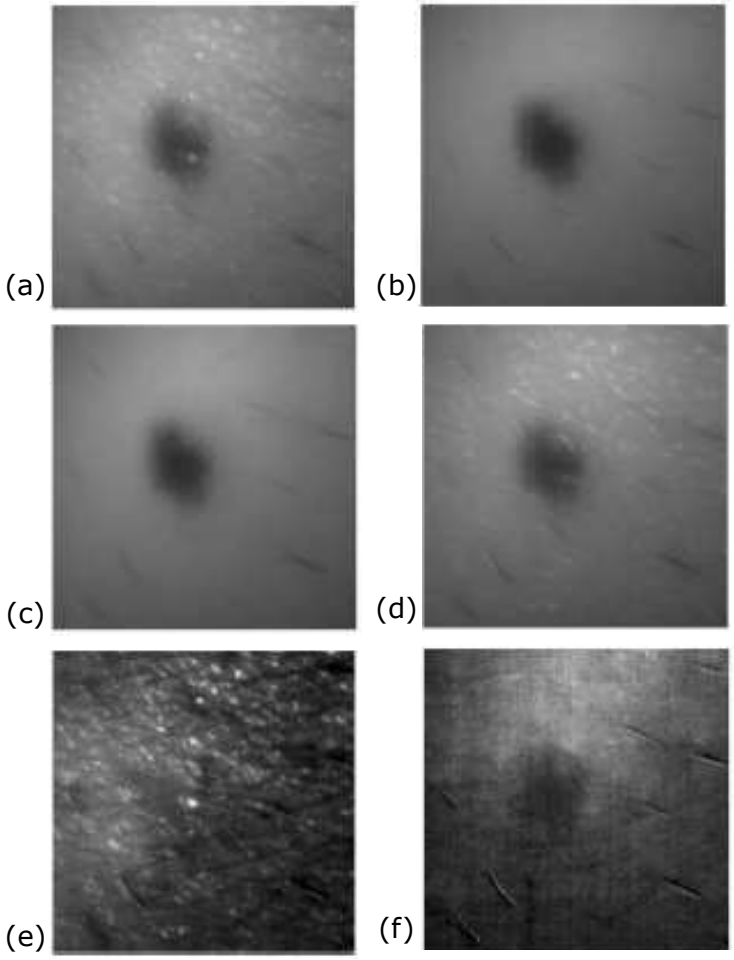

Figure 3.3: Image of a lentigo of a patient as shown by Morgan and Stockford [2003] in (a) Co-linear (C1) (b) Cross-linear (C2) (c) Co-circular (C3 at 45°) (d) Counter-circular (C4 at 45°) (e) Linear polarization subtraction, C1-C2 and (f) Circular polarization subtraction, C3-C2.

After this subtraction, a mixture of backscattered elliptical polarization-maintaining photons and elliptical surface-reflected photons is obtained. To preserve only the polarization-maintaining photons, we can combine the residuals of linear polarization gating (Eqn. 3.1), and that of elliptical channels, (Eqn. 3.3). This gives us a mixture of the surface reflected and polarization-maintaining photons from linear and elliptical polarizations.

$$(C3 - C4) + (C1 - C2) = P_E - S_E + P_L + S_L \tag{3.4}$$

At non-normal incidence, the quantity of surface-reflected photons from linear and elliptical polarizations are different from each other, with a larger contribution from the former (which can be measured theoretically and experimentally). This can be verified by the fact that as we go from co-linear channel to counter-elliptical channels, we are not only increasing the angle of elliptical polarization, but also changing the amount of reflected light projected in the plane of incidence (Parallel or P-polarized) to that perpendicular to

the plane of incidence (Perpendicular or S-polarized). This change in the specular portion of the elliptical channels can be normalized to that of the linear channel by a factor, α, such that $S_E = \alpha\, S_L$. This α value is calculated as the ratio of surface-reflected components of counter-elliptical to co-linear images, and it is computed experimentally on an ROI containing mostly the identified specular-reflection spot.

$$\alpha = \frac{S_E}{S_L} \tag{3.5}$$

Therefore, to eliminate these specular portions from the images, we can reduce the equation as,

$$(C3 - C4) + \alpha(C1 - C2) = P_E + \alpha P_L \tag{3.6}$$

This method allows us to obtain only the polarization-maintaining photons with the elimination of background in terms of specular and multiple-scattered photons. The two mentioned subtraction methods, EPDI and MPDI are compared and illustrated with experiments on different types of samples in Chapter 4.

3.2 EXPERIMENTAL SET-UP

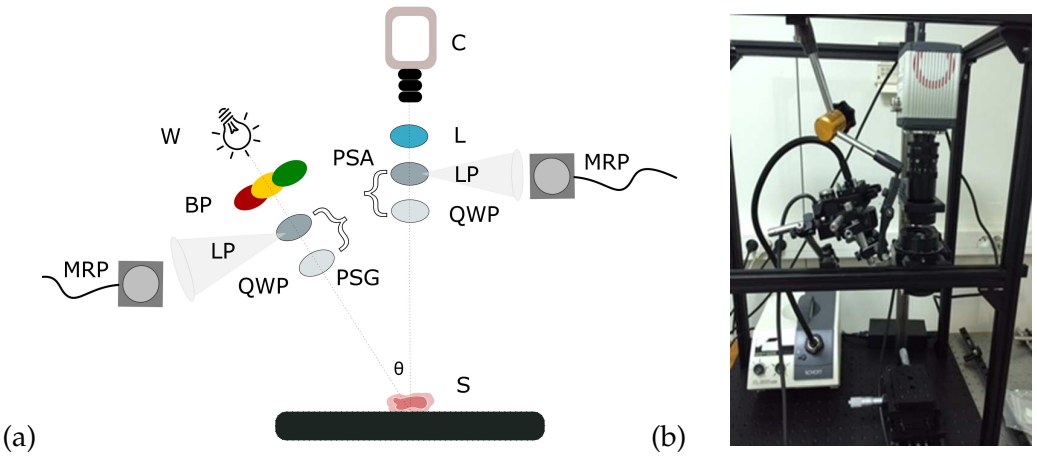

Figure 3.4: (a) Schematic of the experimental set-up with incoherent light where, W: white light source, BP: band-pass filters, PSG: polarization state generator composed of a linear polarizer (LP) and quarter-wave plate (QWP), θ: angle of incidence, PSA: polarization state analyzer composed of a quarter-wave plate and analyzer, L: magnification lens, C: CMOS camera with objective and MRP: motorized rotation plate, (b) Image of the experimental set-up.

The experimental set-up (Figure 3.4 (a) and (b)) composes of a 250W halogen light lamp (KL 2500 Liquid Crystal Display (LCD), Schott AG, Germany) for illumination. The incident light with maximum illumination possible, is first wavelength-filtered with band-pass filters (532, 570, 633 or 670nm with bandwidth 10$\pm$2nm, Thorlabs®, Germany) and is then passed through a Polarization State Generator (PSG) composed of a linear polarizer (1", dichroic, extinction ratio 10000:1, LPVISB100, Thorlabs®, Germany) and a quarter-wave plate (1", achromatic zero-order wave plate for wavelength range 500-700nm with a $\pi/2$

dephasing at 633nm, SPD - Samoylov A.V., Ukraine), to produce elliptically polarized light. The linear polarizer polarizes the incident beam in the required axis (with reference to the plane of incidence) and the quarter-wave plate is then tuned to switch the polarized beam into different types of polarization (linear, elliptical or circular). The desired polarization is chosen and the beam is then incident on the sample.

In the detection path, the reflected beam passes through a Polarization State Analyzer (PSA) composed of a quarter-wave plate (2", achromatic zero-order wave plate for wavelength range 500-700nm with a $\pi/2$ dephasing at 633nm, SPD - Samoylov A.V., Ukraine) and an analyzer (1", dichroic, extinction ratio 10000:1, LPVISB100, Thorlabs®, Germany), to return the state of polarization. The fast axis of the quarter-wave plate is adjusted to tune the backscattered beam's polarization to linear state. The relative rotation angle between polarizers and quarter-wave plates is tuned such as to obtain the desired polarization modes for illumination and detection (Figure 3.5 and Table. 3.1).

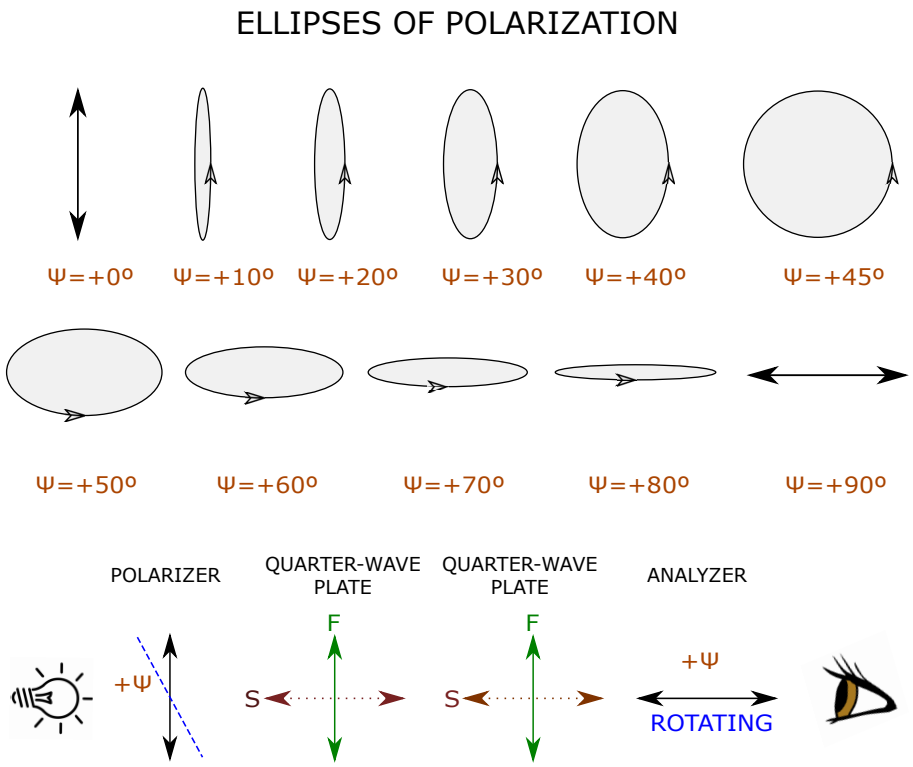

Figure 3.5: Ellipses of polarization and schematic of generating ellipses when tuning the polarizers with the quarter-wave plates kept constant where, φ is the angle of elliptical polarization.

The reflected beam then passes through a magnification lens (AC508-400 A-ML, Thorlabs®, Germany) whose focal length was chosen based on the desired magnification. The backscattered beam is detected by a 16-bit CMOS camera (Orca Flash 4.0, Hamamatsu Photonics, Japan) with an objective (7000E, Laser Components SAS, France). For spectroscopy and speckle studies the calibration and experimental conditions are described in Sections 5.4 and 6.3 respectively.

3.2.1 *Automation*

The precise tuning of the PSG and PSA to produce different polarization states/channels is a very meticulous and sensitive process that needs automation and leads to production of erroneous polarization states or artefacts if done otherwise. For this purpose, we used two motorized rotation stages (1", 360°rotation range, 0.6° rotation in full step, 36rpm, 8MRU-1 and 2", 360°rotation range, 0.01° rotation in full step, 8rpm,8MR190-2-28, from Standa, Lithuania) which run on a two-axis stepper and DC motor controller ($12-36V$, 8SMC4-USB-B9-2, Standa, Lithuania). The motorized stages were controlled using the software `XILab` to have maximum speed and precision in moving the optical components. The linear polarizers in the illumination (1") and detection (2") path were rotated/tuned using the motorized stages and is also indicated in Figure 3.4a. Image acquisition was done with camera software HCImageLive (provided by Hamamatsu for CMOS camera ORCA Flash 4.0) with the possibility of esposure times from $1.1-10ms$.

3.2.2 *Calibration*

The axes of all the components were determined under transmission geometry using extinction measurements and can be seen in Figure 3.6 and are also listed in Table 3.2. To get vertical linear polarization, the components were adjusted to the following angles: Polarizer-illumination 120° , Polarizer-detection 190° , QWP-illumination 160° and QWP-detection 105° . To switch to cross-linear mode, the Polarizer-detection would be tuned to 280°, keeping the other optical components at their previous angles. For producing the co-elliptical channel, e. g. with an ellipticity of +10°, the angles are tuned as: Polarizer-illumination 130° , Polarizer-detection 200° , QWP-illumination 160° and QWP-detection 105° . And similarly for the counter-elliptical configuration, the Polarizer-detection would be tuned to 290°(co-elliptical +90°. Similarly, to produce co-elliptical modes at different ellipticities, we can tune the Polarizer-illumination and Polarizer-detection $+\varphi$ (or $+90+\varphi$ for counter-elliptical mode) from the co-linear mode.

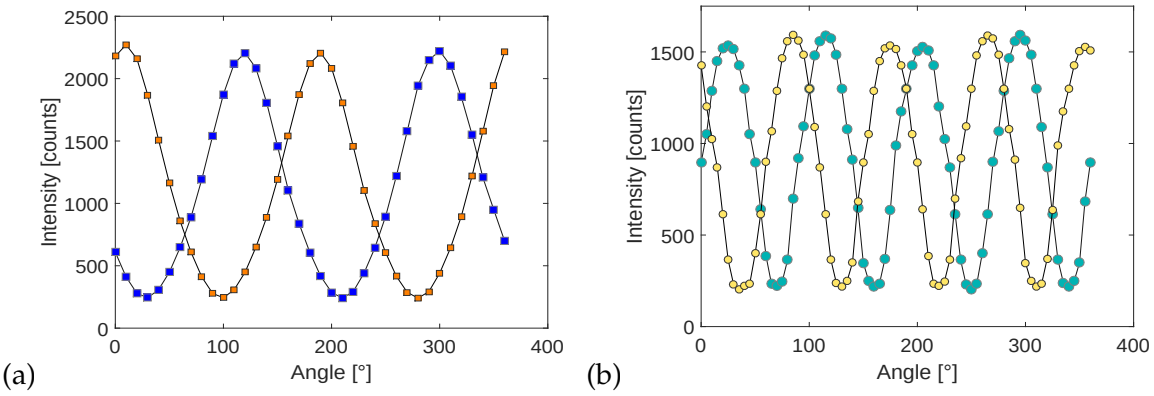

Figure 3.6: Extinction curves of polarization optics in transmission geometry (a) Polarizers (b) Quarter-wave plates. Panels (a) and (b) contain curves of two optical components each, one for the source path and the other for the detection path respectively.

Table 3.2: Transmission axes of optical components: polarizers and quarter-wave plates

A: POLARIZERS

	Polarizer - Illumination		Polarizer - Detection	
Minima [°]	30	210	100	280
Maxima [°]	120	300	190	10

B: QUARTER-WAVE PLATES (QWP)

	QWP - Illumination				QWP - Detection			
Minima [°]	70 - S ⋆	160 - F	250 - S	340 - F	15 - S	105 - F	195 -S	285 - F
Maxima [°]	115	205	295	25	60	150	240	330

The axes of the components were then adjusted under reflectance geometry and experiments were conducted with Intra-lipid® samples for generation of different ellipses. The axis of each component was adjusted to get perfect extinction of the signal detected, and it was observed that the individual axes of each component needed a slight adjustment of $\pm 2°$. The extinction curve of all the optics aligned in reflection geometry, with just the analyzer moving is demonstrated in Figure 3.7. The maxima of the curves indicate linear polarization and corresponds to the Co-linear channel (C1) while the minima of the curves indicate cross-linear polarization and corresponds to the Cross-linear channel (C2).

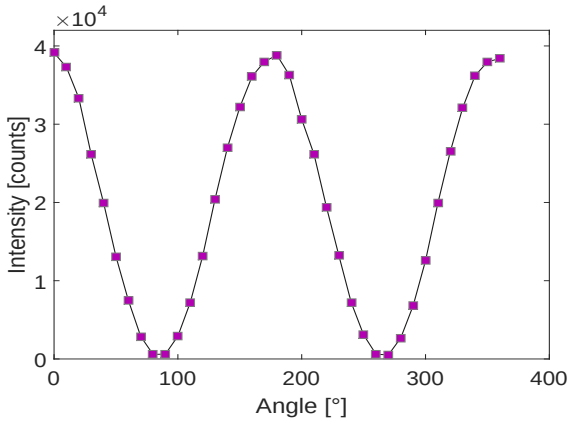

Figure 3.7: Extinction curve of all polarization optics in reflection geometry (as seen in the set-up, Figure 3.4) with Intra-lipid® as a sample.

We use the polarizer/quarter-wave plate couple in the illumination path to generate different elliptically polarized illumination, by adjusting the angle, φ, between the fast-axis of the quarter-wave plate and the linear polarizers' axis. We then use another polarizer/quarter-wave plate couple for detection and the ellipticity 'φ' in the detection path is set to corre-

⋆ **Fast and Slow Axes**
S and F - denote the slow and fast axes of a Quarter-wave plate respectively.

spond to the same as in the illumination path. So for each measurement, we need to tune the two polarizer/quarter-wave plate couples to obtain our desired state of polarization for illumination and detection.

Two different modes of tuning the polarizer/quarter-wave plate couple can be employed: a) tuning just the polarizers with the quarter-wave plates kept constant and, b) tuning the polarizers and quarter-wave plates. The shape and orientation of the ellipses totally depend on the position of the quarter-wave plate. In this manuscript, all the experiments described have been performed using the first method, where only the polarizers are tuned and the quarter-wave plates are kept unchanged and can be seen as described in Figure 3.5. An illustration of behaviour of ellipses when both polarizers and quarter-wave plates are tuned is represented in Figure 3.8.

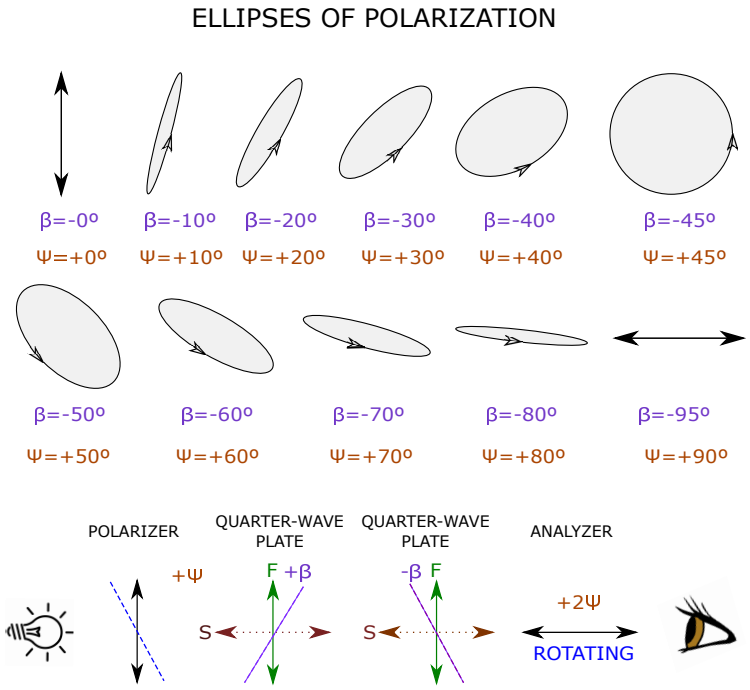

Figure 3.8: Ellipses of polarization and schematic of generating ellipses when tuning the polarizers and quarter-wave plates where, φ is the angle of ellipticity and β is the angle for tuning the QWPs.

In this case, the shape of ellipse and also the orientation of the central axis of the ellipse changes with change in ellipticity. For a given ellipticity of $+\varphi$, the Polarizer-illmination is fixed at it linear axis, the QWPs on either paths are tuned to an angle β with the same magnitude as φ, but vary in handedness of ellipticity (positive or negative) and the Polarizer-detection is tuned to $+2\varphi$ for detecting the required elliptical mode (co or counter). For the co- and cross-linear modes, the QWPs remain at their fast axes and only the Polarizer-detector is kept at +90° from its vertical axis. This case of tuning the polarizer/QWP combination is quite interesting as it may prove as an alternative and different illumination technique which can selectively polarize/highlight different structures or surfaces. With these two modes discussed, it is evident that the intensity and behaviour of signal is very different depending on the shape of the ellipse for the two modes of tuning the

polarizer/quarter-wave plate couple.

3.3 SAMPLES: MATERIALS AND PHANTOM PREPARATION

Different types of samples were used for calibration and validation of measurements made in the course of this thesis. All the experiments were conducted in compliance with the directions of the Local Ethics Committee. All procedures were in agreement with National Institutes of Health (NIH) Guidelines.

3.3.1 *Liquid Phantom: Intra-lipid®*

The liquid phantom was composed of an aqueous Intra-lipid® (20% Stock solution, Sigma-Aldrich, France) diluted to adequate concentrations. The concentration of Intra-lipid® was adapted to match the optical properties of biological tissues, but with a scaling in size of the sample for macroscopic measurement of depth. The optical properties of Intra-lipid® 1% (see Figure 3.9a) was determined as described in Section 3.4: the absorption coefficient (μ_a) was considered negligible and a μ_s' value of $\mu_s'(1\%) = 10.3 \pm 0.5 cm^{-1}$ was estimated. According to the accuracy of our optical (magnification) and mechanical components, a 0.1% diluted solution was used, corresponding to $\mu_s'(0.1\%) = 0.95 \pm 0.05 cm^{-1}$, allowing depth measurements at a millimetric scale. The anisotropy factor of Intra-lipid® was estimated to a value of $g = 0.73$ [van Staveren et al., 1991] leading to a reduced scattering mean free path $MFP' = (1-g)/\mu_s' \sim 2.8mm$ (that is approximately 10 times longer than in biological tissues).

3.3.2 *Solid Phantoms*

In order to validate theoretical models and to test experimental systems, it is desirable to have solid/solid-liquid tissue simulating phantoms, with known optical characteristics. Thus, there is a need for the fabrication of 3D phantoms that mimic rodent skull, brain tissue and blood vessels in different layers. Two types of solid phantoms were tested based on previous works[Cheng, 2012; Cubeddu et al., 1997]:

1. Agar/Titanium di-oxide (TiO_2) solid phantom
   The required amount of distilled water is measured and added to a flask and heated for 2 minutes on a magnetic heater/stirrer. Agar (conc. 2%) and TiO_2 (conc. 0.1%) are added to the flask and the solution is heated. When it reaches the boiling point of Agar (91° C), the flask is placed in a vacuum chamber for two cycles (each cycle refers to the rising of bubbles and lasts for approx. 2 minutes) to eliminate the bubbles. The solution is then poured into the required container and placed in the freezer for 2-3 minutes for allowing for the setting of the solid. The phantom is stored in 4° C.

2. Agar/Intra-lipid® solid phantom
   The required amount of distilled water and Agar (conc. 1%) is measured and added to

a flask and uniformly mixed using a magnetic stirrer. The solution is then heated using a microwave to 91° C. The solution now becomes clear, and is then cooled to 60° C with continuous stirring. At 60° C, the measured amount of Intra-lipid® (conc. 1%) is added and the solution is cooled to 40° C. The solution is then transferred to the required container and cooled rapidly in a cold-water bath to allow for the setting of the solid. The phantom is stored in 4° C. An example phantom of 1% Agar- 0.1% Intra-lipid®is represented in Figure 3.9b.

3.3.3 *Ex vivo sample - Neck of chicken*

To check for biological tissue feasibility, a piece of chicken neck (bought from the supermarket, used as a biological phantom) pinned to a sample holder was used (see Figure 3.9c). The neck in particular was chosen due to the prominence of a blood vessel in the region. The superficial tissue was sufficiently hydrated with glycerine to track the mirror reflections.

(a)  (b)  (c) 

Figure 3.9: Example photos of samples. (a) Liquid phantom: 1% Intra-lipid®, (b) Solid phantom: 1% Agar- 0.1% Intra-lipid®, and, (c) *Ex vivo* sample: neck of a chicken.

3.3.4 *In vivo samples*

1. Human skin
   Different skin abnormalities (mole/nevus, burn scar etc.) of volunteers were illuminated under the given experimental conditions. A glass cover-slip was placed on the skin to track the specular reflections at the surface. The exposure dose was much below the maximum permissible exposure values in the visible wavelength range ($\sim 0.065 W/cm^{-2}$) (Laser Institute of America 2000) and an informed consent was obtained from all subjects. A sample image of a burn scar of a volunteer is represented in Figure 3.10a.

2. Exposed cortex of an anaesthetized rat
   The second type of *in vivo* sample was the exposed cortex of an anaesthetized rat (see Figure 3.10b). An adult, female Longevans rat was first anaesthetised intra-peritoneally with 5% Isofluorane followed by Urethane (130mg/100g body weight) and then placed in a stereotaxic frame for mechanical stability during craniotomy and measurements. Body temperature was monitored, and maintained between 36°- 38° C with the use

of a heated-blanket. A craniotomy was performed creating a cranial window of ca. 5mmx5mm above the barrel cortex. To prevent the cortex from drying, a chamber of dental cement was created around the entire cranial opening and was filled with agarose in saline (2%). To provide a flat optical interface, the chamber was sealed with a microscope cover-slip. In compliance with directions of the Local Ethics Committee, we kept the number of animals used for this study as small as possible. All procedures were in agreement with NIH Guidelines.

(a)  (b) 

Figure 3.10: Example photos of *in vivo* samples. (a) Human skin: Burn scar of a volunteer, and, (b) Exposed cortex of an anaesthetized rat.

3.4 MEASUREMENT OF OPTICAL PROPERTIES

The optical properties of the phantoms were measured using the integral reflectance method described in the works of Farrell and Patterson [1992] and Gobin et al. [1999]. The method involves processing the back-scattered image acquired from a detector by integrating to decrease sensitivity to noise. The resulting curve, the integral reflectance is then fitted with a relaxation model to evaluate the optical properties, Absorption coefficient (μ_a) and Reduced scattering coefficient (μ_s'). This method allows for a non-contact, non-invasive, low cost and time-efficient quantitative measurement of optical properties of biological tissues.

3.5 IMAGE PROCESSING

Images were acquired using HCImageLive Software (provided by Hamamatsu for CMOS camera ORCA Flash 4.0). Signal-to-noise Ratio (SNR) was calculated as the ratio of desired signal intensity to the background intensity [$SNR = 10\log(I_S/I_N)$]. A sequence of twenty images were taken with an adapted exposure time per measurement in order to preserve a high SNR ($\sim$ 35dB) for each measurement. The noise was reduced by averaging these images. An image registration, which corrected translational and rigid body movements in the images (described in Section 3.5.1), was developed and applied on the images using some basic functions in `MATLAB R2015a`. After correcting for movement, the images were averaged to a single mean-image. These mean-images were then subtracted based on one of the methods described in Section 3.1.

3.5.1 *Image registration for motion artefacts*

In the process of *in vivo* image acquisition, there is always a high probability of having motion artefacts in between the acquisition of each image. This could be mainly due to involuntary manual movements of the subject, vibrations from the machinery/environment or simply due to breathing from the subject. The method of polarization gating that we are focussing on is based on *pixel-by-pixel* subtraction (Polarization Difference Imaging (PDI) described in Section 3.1) and hence it is imperative to have the images taken at different channels to be movement registered with each other. Each relative movement (of the order of tens of pixels) of an image will degrade the resulting image which is either added and/or subtracted from another image, thus leading to a loss of original information. In MPDI method, it is required to perform image subtraction and addition of images from 4 different channels, and makes the movement registration a challenge.

To illustrate the kind and magnitude of movement artefacts that occur within our experimental set-up, two random channel images taken from a mole on the dorsal side of a volunteer's hand are shown in Figure 3.11. The chosen reference image, which is normally referred to as the 'fixed' image is fused to the 'moving' image using built-in `MATLAB` functions as seen in Figure 3.11. Samples are always marked before image acquisition with *fiducials*, or reference points that help in the alignment of the moved images. Determining the correct geometric transformation parametersis the key to achieving good image registration. The extent of the movement is represented by the shading of different colours, magenta and green representing each individual image. Normally, the movement is of the order of 1-10 pixels depending on the type of samples used: liquid, solid, *ex vivo* or *in vivo*. It is thus imperative to find an efficient, fast and reliable tool to register the images in real-time to achieve perfect image subtraction using PDI, especially for *in vivo* samples.

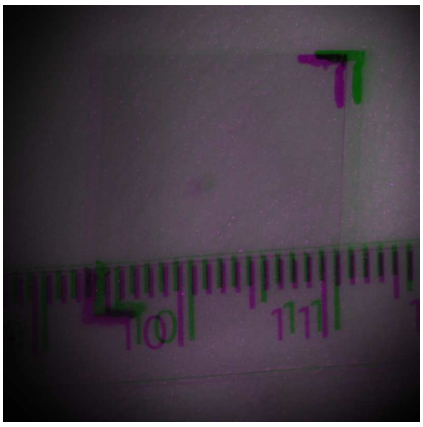

Figure 3.11: Superposed montage of two images (of a mole on dorsal side of a volunteer's hand) affected by movement artefacts. There is a glass coverplate with a marked fiducial (on the top-right and bottom-left corners respectively) and a ruler placed in the FOV of the image to serve as fiducials. The overlapping of images is performed with `MATLAB 2015a` in-built function `imshowpair` in the '*joint*' mode. The colours magenta and green are markers of the two individual images that show extent of the motion artefact. Image size, 800x800 pixels.

Image registration techniques are broadly divided into two classes based on either intensity/grey-level matching or matching of local geometrical patterns. Basic information on image registration techniques can be found in literature from Gozalez and Woods [2002] and Henderson et al. [1985]. In this thesis, we have used the former method, intensity-based image registration, which uses an iterative process to maximize the mutual information and/or minimize the Mean-Square Error (MSE) [Pluim et al., 2000]. This approach maps certain pixels in each image to the same location based on relative intensity patterns and is best suited for work-flows that involve a large collection of images. The Image Processing Toolbox from `MATLAB 2015a` has built-in functions (*imregister, imregtform* etc.) that help perform automatic, intensity-based image registration. In this thesis, we have used the function *imregister*, which involves the definition of three different parameters: `metric`, `optimizer` and `transformation-type`. The `metric` parameter defines the similarity between the specified images by providing a scalar value, or the 'initial transformation matrix'. It has the possibility of using the `registration.metric.MeanSquares`, which uses an algorithm to calculate MSE or `registration.metric.MattesMutualInformation`, which maximizes the number of coincident pixels with the same relative brightness values [Mattes et al., 2001]. The `optimizer` parameter then defines the method for maximizing or minimizing the similarity metric. It can be of two types: a regular step-descent approach that uses constant length steps along the gradient to optimize the similarity metric in the direction of the extrema (`registration.optimizer.RegularStepGradientDescent`) or an evolutionary algorithm that iterates by perturbing or mutating the parameters from previous iterations to find a set that gives the best image registration [Styner et al., 2000] (`registration.optimizer.OnePlusOneEvolutionary`). The `transformation-type` parameter defines the transformation that has occurred between the images and can be either rigid or non-rigid. The *imregister* function gives us the choice of four transformation types: translation, rigid (includes translation and rotation and is most adapted to our case), similarity and affine.

Figure 3.12 describes the work-flow for registering a set of images to a reference as performed during this thesis. At first, the 'fixed' and 'moving' images are read into the directory and undergo some pre-registration processing: resizing (to increase resolution), cropping and/or filtering the ROI. The images are then mounted together (as seen in Figure 3.11) to see the extent of the movement and to visually inspect the motion artefact for setting the optimization parameters. Once we have a thorough understanding of the parameters that we need to best fit our problem, the similarity metric and optimization methods are predefined using the *imreconfig* function in the 'multimodal' regime. With our image acquisition techniques, the image registration was done using the 'rigid' transformation model with bicubic interpolation. Optimal registration was determined by maximization of mutual information using a 'One plus One' evolution algorithm. Once all the parameters were defined and set, the *imregister* function produces an output transformation matrix, T which gives the co-ordinates for re-aligning the moved images. In order to verify the quality of the image registration achieved, there are several concepts and statistical analyses that can be implemented [Pluim et al., 2003].

As an example, the images of a mole with motion artefacts shown in Figure 3.11 have been movement corrected and displayed in 3.13. It is evident from the figure that the

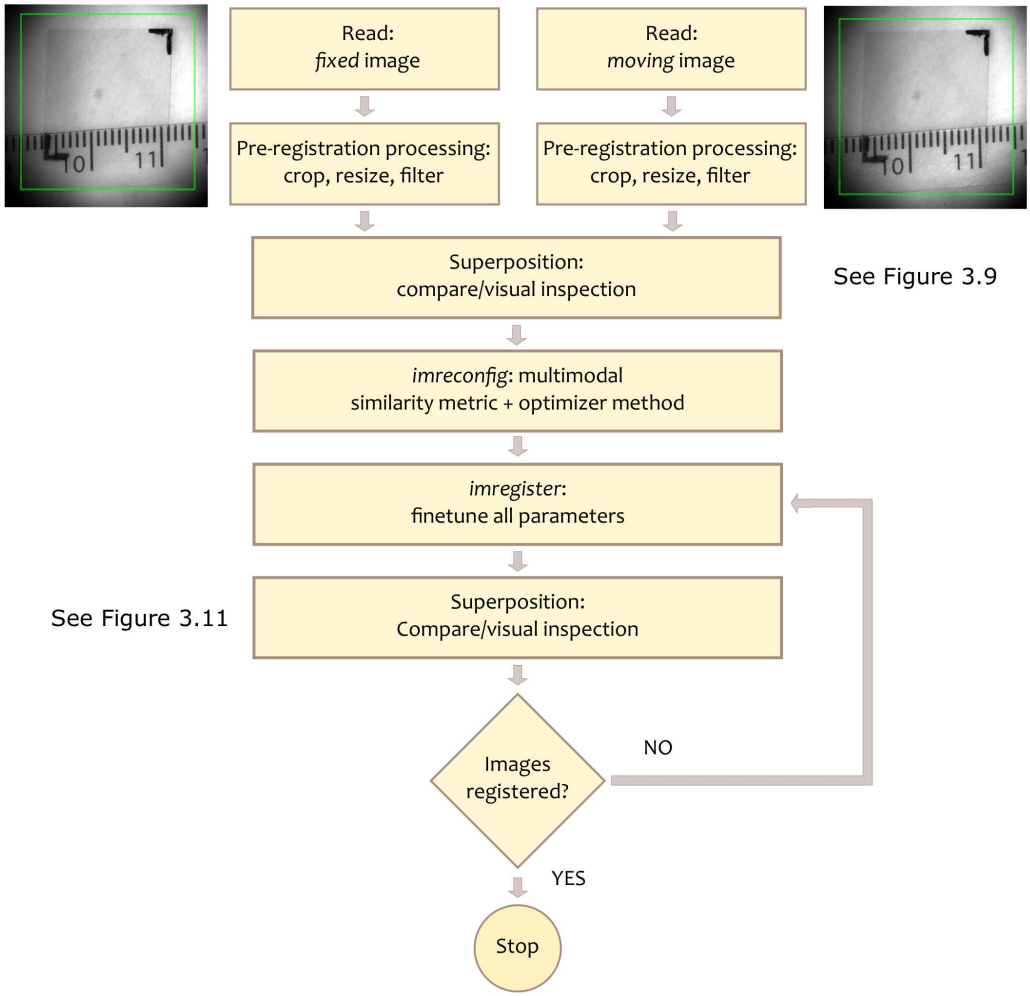

Figure 3.12: Flowchart depicting the registration process adopted for reducing the motion artefacts between two images. Examples of the raw images for *fixed* and *moving* images are shown along with the ROI marked in green.

colour-shading which represents the extent of movement is minimal and the two images have overlapped quite harmoniously. The readings on the ruler and the fiducials are clear without the presence of any blurring. But there is still a slight hint of magenta in the overlapping image. This is mainly because each image taken from different channels in our experiment constitutes a different volume in depth, which denotes that the intensity/grey-levels of every image will vary depending on the channel, ellipticity and wavelength used. Thus when we use the intensity-based image registration algorithm, there might be a slight hint of movement (of the order of $\leqslant$ 1 pixel).

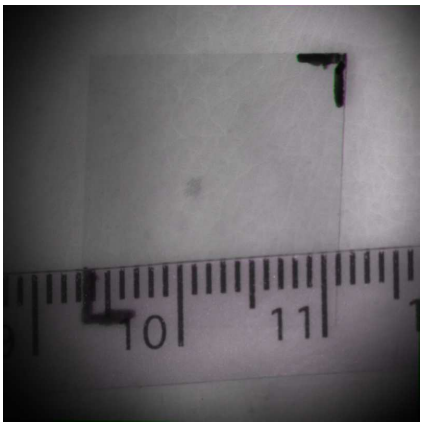

Figure 3.13: Superposed montage of two images (of a mole on dorsal side of a volunteer's hand) corrected from movement artefacts built-in `MATLAB` image registration functions. There is a glass coverplate with a marked fiducial (on the top-right and bottom-left corners respectively) and a ruler placed in the FOV of the image to serve as fiducials. The overlapping of images is performed with `MATLAB 2015a` in-built function `imshowpair` in the '*joint*' mode. The colours magenta and green are markers of the two individual images that show the extent of the motion artefact. Image size, 800x800 pixels.

Thus, a simple and basic introduction to multi-modal image registration was achieved using the built-in `MATLAB` functions. Further work is needed to get an in-depth knowledge of the common practices and the aspects required for multi-modal image registration which could be applied to more *in vivo* applications.

3.6 SUMMARY

In summary, this chapter dealt with the introduction and characteristics of elliptically polarized light and how it can be used in polarization gating to isolate and measure only the photons that have kept its initial polarization. The details and description of the differences of different polarization gating methods: Linear Polarization Difference Imaging (LPDI), Elliptical Polarization Difference Imaging (EPDI) and Multi-Polarization Difference Imaging (MPDI) were outlined. MPDI is also a means of accessing different depths as a function of ellipticity and triumphs over LPDI which only allows access to surface structures.

In particular, the focus of this thesis is on the MPDI method of background subtraction. The experimental set-up and calibration conditions were explained for ease of understand-

ing the practical approach. The generation of ellipses of different intensity and magnitude was explained in the two approaches of tuning the polarizer/QWP couple. In general, keeping the QWPs constant produces ellipses that are oriented in the same central axis for the ellipse with changing magnitudes that are ellipticity-sensitive. The alternative approach of tuning all the components (polarizers and QWPs) results in generation of ellipses that vary in both magnitude and orientation. This might also be of interest for alternative illumination techniques to highlight different structures in a biological sample. The experiment has been automated to quite an extent in terms of tuning the optics (with software-controlled motorized rotation plates) and image acquisition (with camera software). But there are some movable parts which need tuning or adjustment before each image acquisition step and might lead to either movement artefacts or changes in signal intensity. To improve precision and reduce artefacts, there is still scope for complete automation with more powerful and universal software that controls all the components of the set-up. In brief, the set-up provides a low-cost, non-contact and flexible imaging system for phantom, *ex vivo* and *in vivo* imaging.

4

ENHANCED CONTRAST AND IMPROVED BACKGROUND SUBTRACTION USING MULTI-POLARIZATION DIFFERENCE IMAGING (MPDI)

This chapter illustrates the results of polarization gating that combines co- and counter-elliptical measurements of *in vivo* samples illuminated to selectively access sub-surface tissue layers. The results of two polarization gating methods, Elliptical Polarization Difference Imaging (EPDI) and Multi-Polarization Difference Imaging (MPDI) are compared for different phantoms, *ex vivo* and *in vivo* illuminated at 633nm wavelength (as described in Section 3.1). *In vivo* experiments were performed on skin abnormalities of volunteers and on exposed cortex of an anaesthetized rat to illustrate the results of the subtraction method and access spectral information. This chapter represents a detailed illustration of the results published in Sridhar and Da Silva [2016a].

4.1 COMPARING ELLIPTICAL POLARIZATION DIFFERENCE IMAGING (EPDI) & MULTI-POLARIZATION DIFFERENCE IMAGING (MPDI)

The different phantoms were examined under the imaging channels described, and the images were then processed and compared for the two subtraction methods in question. The relation between image contrast and the state of polarization were examined and analyzed.

4.1.1 *Liquid Phantom*

Experiments on the Intra-lipid® were conducted to compare the two background subtraction methods and served as a sample for calibrating the set-up. A plastic ruler was placed obliquely in a tank containing the diluted Intra-lipid® as shown in Figure 4.1a and imaged at different ellipticities to observe the signal coming from different depths.

The 'α' factor for removing specular content was calculated experimentally as follows: A series of 100 images were taken at channel C1 and channel C4 (which contain the respective linear and elliptical specularly reflected components). The ROI containing an identified specular spot was averaged to get a mean value in both C1 and C4. α was then calculated as the ratio of the mean specular value of elliptical to linear channels. This value was found to decrease with the increase in the angle of elliptical channel. The value and range of α depends on the sample used and has to be calculated individually for every experiment. Figure 4.2 shows that, for Intralipid® 0.1% measurements, α was found in the range 1.01

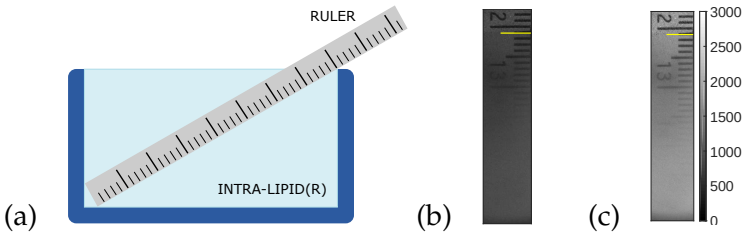

Figure 4.1: Results of the Intra-lipid® experiments: a) Ruler placed obliquely in a tank containing Intra-lipid® solution, b) Elliptical channel image at 45° after Elliptical Polarization Difference Imaging (EPDI) , c) Elliptical channel image at 45° after Multi-Polarization Difference Imaging (MPDI). Panels (b) and (c) have a common colorbar represented at the right edge of the figure. Yellow-dotted line represents the Intra-lipid®-air interface. Each graduation on the ruler (i.e. 1mm) corresponds to 0.35mm in actual depth. Wavelength, 633nm.

- 0.78, for ellipticities 0° to 90°.

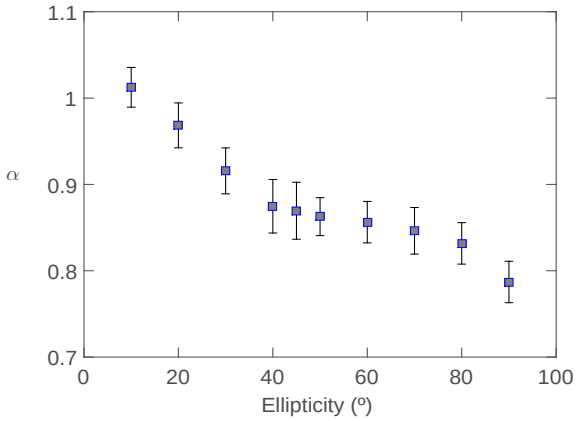

Figure 4.2: Trend of α factor as a function of ellipticity for 0.1% Intra-lipid® experiments.

The polarization gated images of EPDI and MPDI are represented in Figures 4.3a and 4.4a respectively. Although visual inspection of EPDI and MPDI does not reveal too much information about the contrast and depth resolution of images from different ellipticities, it is evident that the amount of signal measured from either of the methods is quite different (seen in Figures 4.3b and 4.4b), with MPDI providing a superior signal intensity. It is thus imperative to quantify the signal at different parts of the images and w.r.t the ellipticity of the channel.

As a first step for quantification, the mean intensity of images obtained with EPDI and MPDI is represented in Figure 4.5. The mean intensity was calculated at smaller ROIs corresponding to the same pixel cordinates of different images and then plotted as a function of ellipticity. This process was repeated for ROIs all across the FOV and the standard deviation error for all measurements has also been represented in Figure 4.5. It shows that with MPDI, there was a higher signal intensity, especially for larger angles of elliptical polarization (a 110 % increase in angles 30° and 40°) in the imaging channels. The signal intensity showed

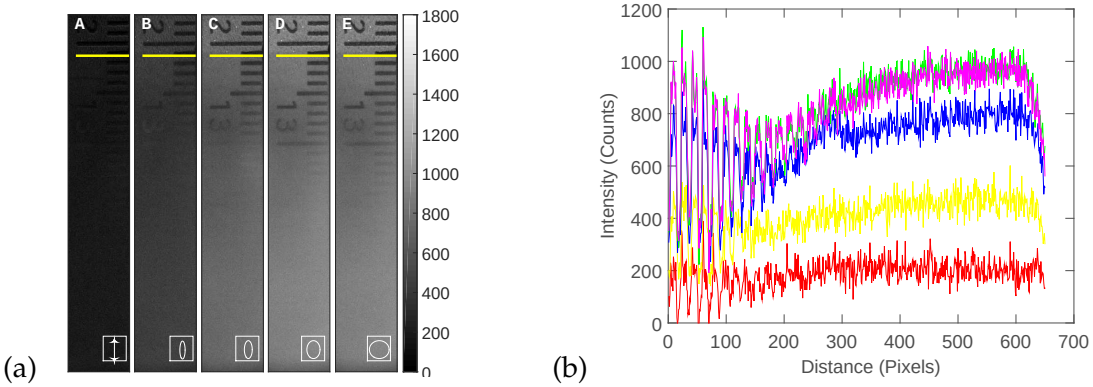

Figure 4.3: (a) Elliptical Polarization Difference Imaging (EPDI) images at different ellipticities for 0.1% Intra-lipid®phantom with a ruler (see Figure 4.1a). Panel A-E are the contrasts for EPDI at 0°, 10°, 20°, 30°, 40° and 45° respectively. They have a common colorbar represented at the right edge of the figure. Yellow line represents the Intra-lipid®-air interface. Each graduation on the ruler (i.e. 1mm) corresponds to 0.35mm in actual depth. Wavelength, 633nm. (b) Vertical cross-plots of EPDI images at different ellipticities. Ellipticities are represented in colours: red (10°), yellow (20°), blue (30°), green (40°) and magenta (45°) respectively.

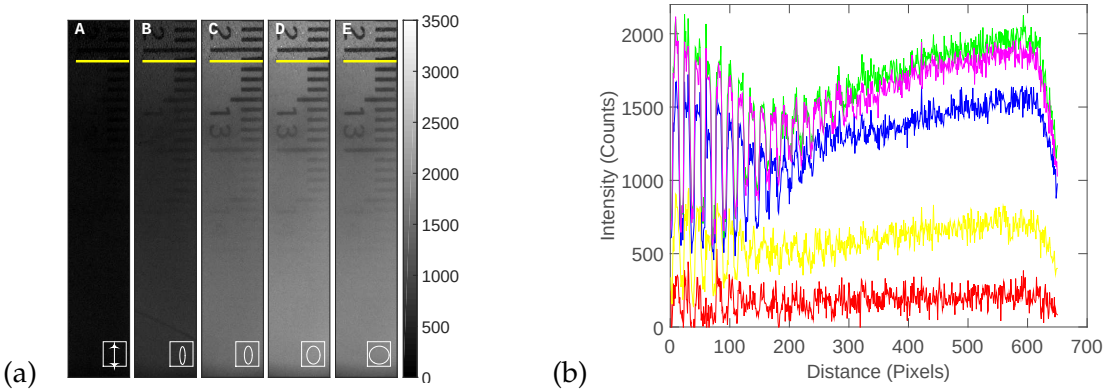

Figure 4.4: (a) Multi-Polarization Difference Imaging (MPDI) images at different ellipticities for 0.1% Intra-lipid®phantom with a ruler (see Figure 4.1a). Panel A-E are the contrasts for MPDI at 0°, 10°, 20°, 30°, 40° and 45° respectively. They have a common colorbar represented at the right edge of the figure. Yellow line represents the Intra-lipid®-air interface. Each graduation on the ruler (i.e. 1mm) corresponds to 0.35mm in actual depth. Wavelength, 633nm. (b) Vertical cross-plots of MPDI images at different ellipticities. Ellipticities are represented in colours: red (10°), yellow (20°), blue (30°), green (40°) and magenta (45°) respectively.

an increase from linear to 40° elliptical polarization reaching a plateau after 40° (close to circular polarization).

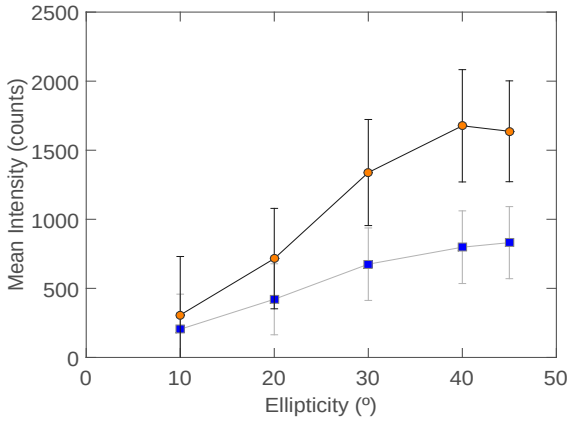

Figure 4.5: Signal intensity of 0.1% Intra-lipid® when performing (a) Elliptical Polarization Difference Imaging (EPDI) (squares), (b)Multi-Polarization Difference Imaging (MPDI) (circles). Standard deviation bars are also shown. Image exposure time, 1000ms.

Figure 4.6 shows the contrast as a function of depth probed (in mm) for the two subtraction methods. The contrast was measured using the ratio (I_{Max}-I_{Min})/(I_{Max}+I_{Min}), where I represents the mean value of intensity taken over the ROI containing the bars of the ruler. In terms of depth, EPDI allowed us to have a reasonable contrast up to 13 graduations (i.e. 4.55mm), as against MPDI , which allowed a good contrast up to 20 graduations (i.e. 7mm). This clearly shows that there is a substantial increase in percentage of signal intensity and in the reachable depth when background subtraction is achieved using MPDI . This is also very evident visually when comparing Figure 4.1 (b) and Figure 4.1 (c), where Panel (c) appears to have a better contrast than Panel (b).

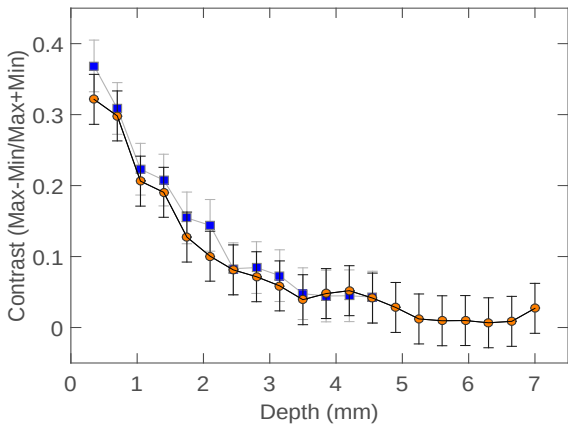

Figure 4.6: Depth probed with Elliptic Channel at 45° for 0.1% Intra-lipid® when performing (a) Elliptical Polarization Difference Imaging (EPDI) (squares) (b) Multi-Polarization Difference Imaging (MPDI) (circles). Standard deviation bars are also shown. Image exposure time, 1000ms.

This experiment shows that polarized light can be collected up to 7mm in depth which corresponds to 0.7mm in biological tissues (as there was a scaling in the optical properties of Intra-lipid® by a factor of 10).

4.1.2 *Ex vivo*

The *ex vivo* experiments were conducted on a piece of neck of a chicken (See Figure 4.7) and illustrated the feasibility of this study in biological tissues. In the ROI projected in Figure 4.7 (c), there is evidence of a vessel appearing diagonally in the cross-linear image, indicating that the vessel is located at a certain depth from the surface. This vessel is not visible in the co-linear image (see Figure 4.8) and thus confirms that it lies in the sub-surface. This is also further substantiated in Figs. 4.9 and 4.10 where the vessel is only seen in the contrasts of elliptic channels at 10°, 20°, 30°, 40°, 45° and 50° (Panels D-I). The presence of wrinkles (caused due to the attachment of the tissue with metallic pins) can also be seen pronounced in Panels E-H. Validating our statements, elliptic channels up to 45° show the presence of deeper lying structures, whereas smaller angles, i.e. smaller elliptic channels show superficial structures or structures close to the surface.

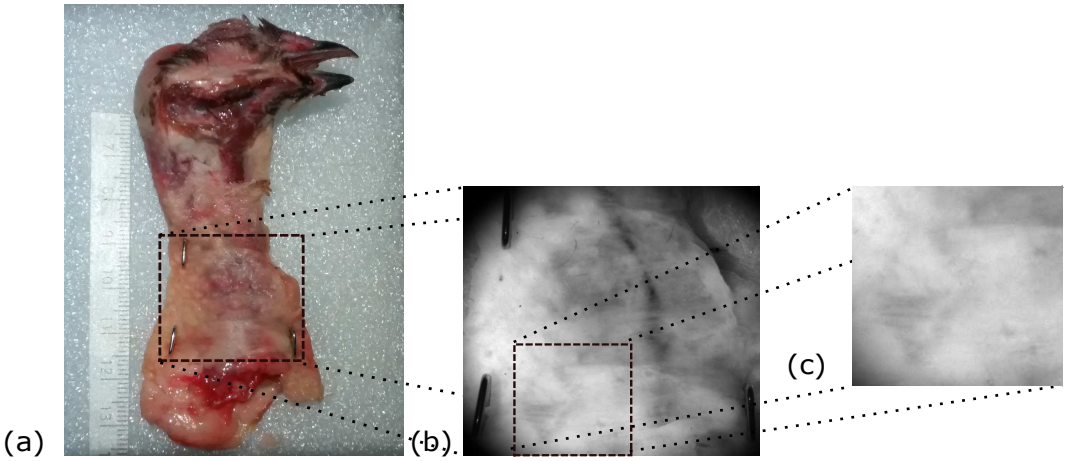

Figure 4.7: *Ex vivo* sample of neck tissue of a chicken: a) Top view of the sample. b) Cross-linear image of a part of the neck under study. c) Zoom-out (Cross-linear) of a section containing a vessel indicated by the red arrow. Images taken in white light. Thickness of epidermis, ~0.5-0.8mm (determined by dissection post imaging).

Comparing EPDI and MPDI (Figs. 4.9 and 4.10 respectively), it is evident that MPDI shows a much better contrast as compared to EPDI with an increase in the contrast signal intensity. It is also interesting to observe the structures in elliptic channels 60° to 90°, as they look completely different to the structures seen in the cross-linear image. This could be due to the fact that, after 45° (which corresponds to circularly polarized configuration) the plane of polarized light shifts by 90° to be in the 'S-polarization' configuration. This in turn would only polarize the structures that are perpendicular to the plane of polarized light. In the EPDI configuration, Panels I-L in Figure 4.9 show the distinct presence of wrinkles,

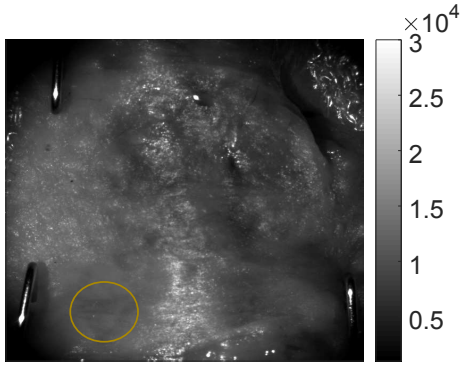

Figure 4.8: Co-linear (C1 image of a part of the neck under study. Yellow circle represents the location of the vessel, which cannot be seen in this figure. Colorbar of the image is represented at the right-hand side.

and can be considered an important application to probe such structures.

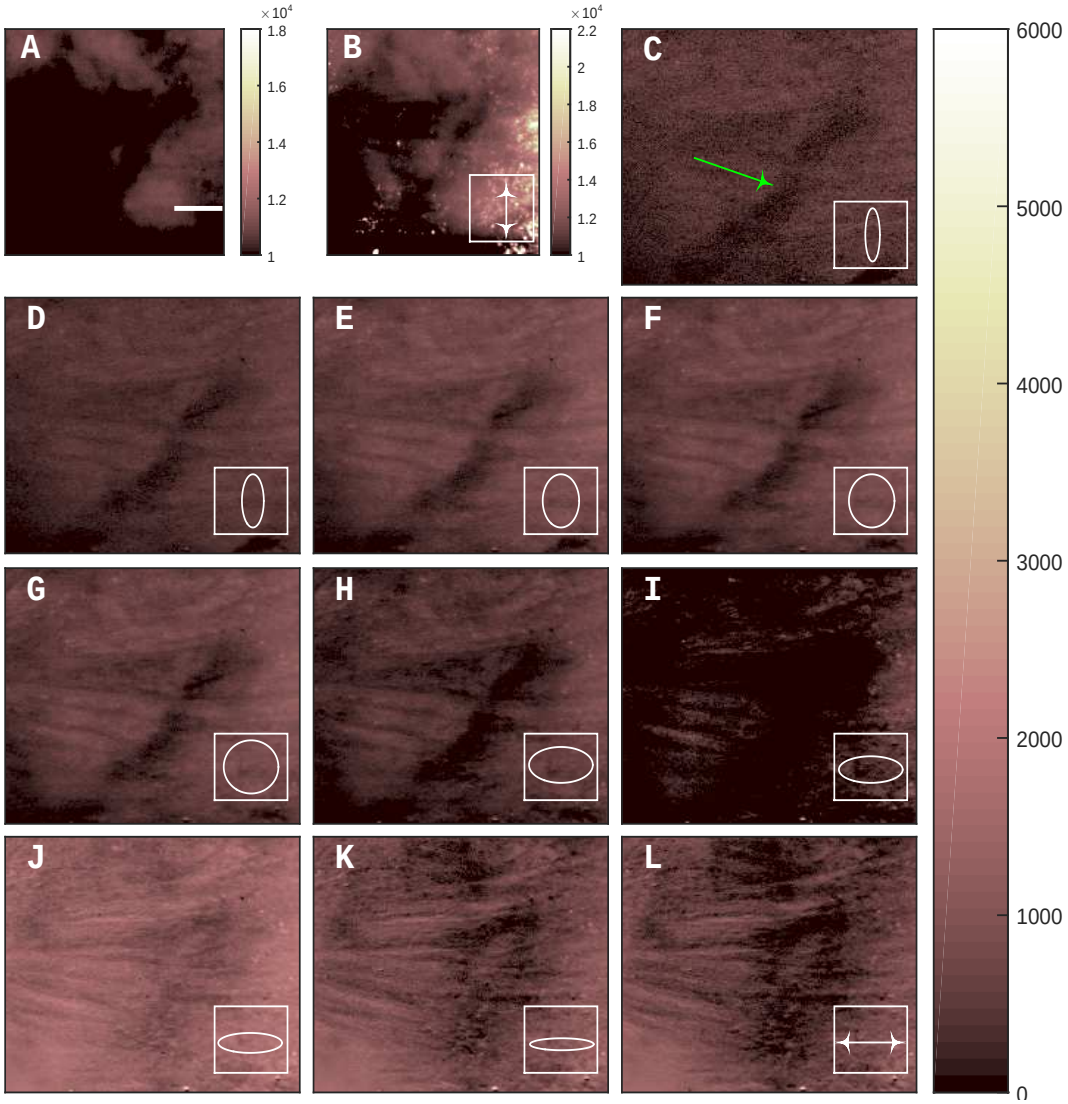

Figure 4.9: Contrast for linear and elliptic channels for *ex vivo* measurements on neck tissue of a chicken. Panel A is the Cross-linear image. Panel B is the contrast of the subtraction of linear (co and cross) channels. Panel C-L are the contrasts for Elliptical Polarization Difference Imaging (EPDI) at 0°, 10°, 20°, 30°, 40°, 45°, 50°, 60°, 70°, 80° and 90° respectively. Scale bar (Panel A), 2mm. Wavelength, 633nm. Image exposure time, 1000ms. Behaviour of the polarized light (linear/elliptical) is represented at the bottom-right corner of each panel. Panels A and B are raw images and have their own colorbar. Panels C-L have a common colorbar represented at the right border of the image. Green arrow in Panel C indicates the presence of the vessel.

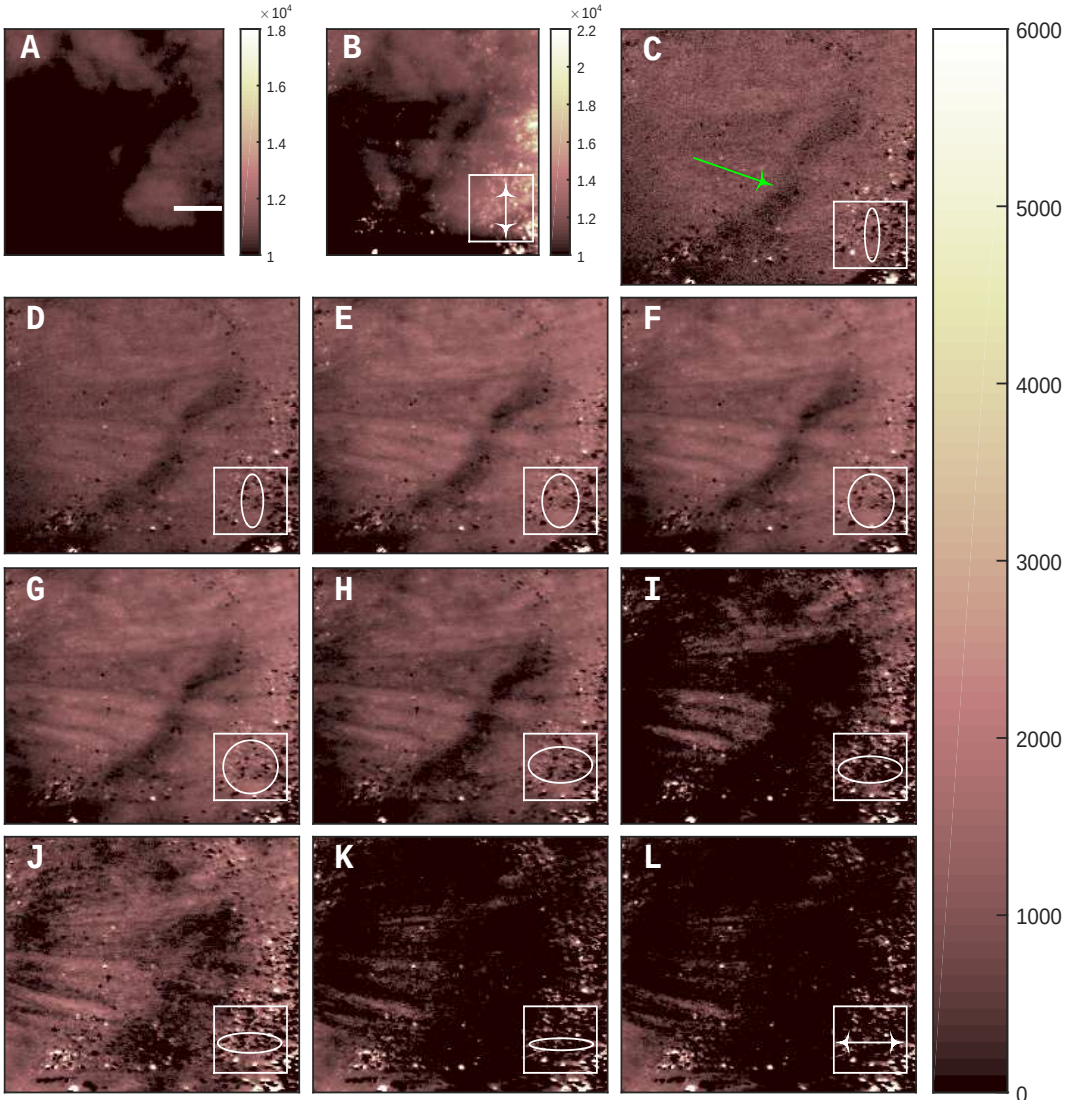

Figure 4.10: Contrast for linear and elliptic channels for *ex vivo* measurements on neck tissue of a chicken. Panel A is the Cross-linear image. Panel B is the contrast of the subtraction of linear (co and cross) channels. Panel C-L are the contrasts for Multi-Polarization Difference Imaging (MPDI) at 0°, 10°, 20°, 30°, 40°, 45°, 50°, 60°, 70°, 80° and 90° respectively. Scale bar (Panel A), 2mm. Wavelength, 633nm. Image exposure time, 1000ms. Behaviour of the polarized light (linear/elliptical) is represented at the bottom-right corner of each panel. Panels A and B are raw images and have their own colorbar. Panels C-L have a common colorbar represented at the right border of the image. Green arrow in Panel C indicates the presence of the vessel.

4.1.3 *In vivo*

4.1.3.1 *Human skin*

Mole/Nevus

A mole on the dorsal side of a volunteer's hand was observed (see Figure 4.11). Figure 4.12 shows the contrast of MPDI performed on skin images. It can be observed that the mole is quite clearly outlined in the elliptic channels (Panels C-L), but is negative and depicts the depolarized photons. On the other hand, it can be seen that the intensity of a polarizing structure (seen towards the right edge of each panel) increases from Panels C-F. And inversely, the intensity of this structure is observed to be decreasing from Panels H-L. There is also the appearance of different structures within the space of the mole from Panels H-l, indicating that these structures are polarizing in a direction different from the co-linear direction (vertical) and horizontal to polarization at 90° (back to linearly polarized light, but in the opposite direction). This behaviour conforms with that of the ellipses shown in Figure 3.5. Due to the effects of image subtraction, the SNR of the resulting channel images is smaller than that of the measured images. Using basic image processing should allow to reduce the noise content of the images. The depolarization/negativity of deeper lying structures could be mainly due to very high specular components from the elliptical channels. This can be avoided by an improvement in the set-up with the addition of a telecentric objective that converges the illumination beam and provides a more homogeneous illumination.

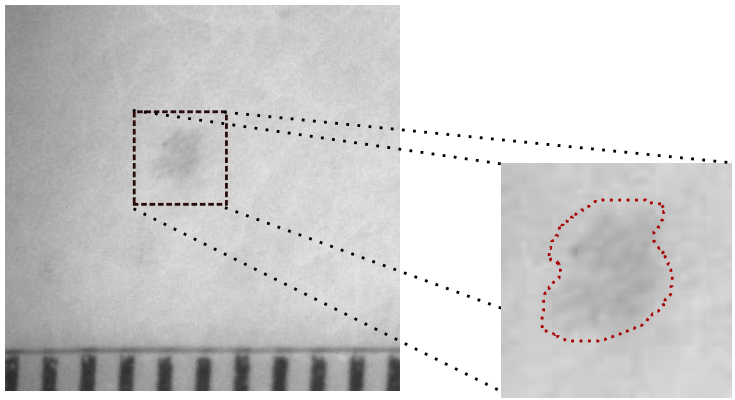

Figure 4.11: Dorsal side of a hand along with a zoom-out of the mole which was studied for the *in vivo* experiments. A ruler with graduations in millimetres is seen at the bottom of the image. Images taken in white light.

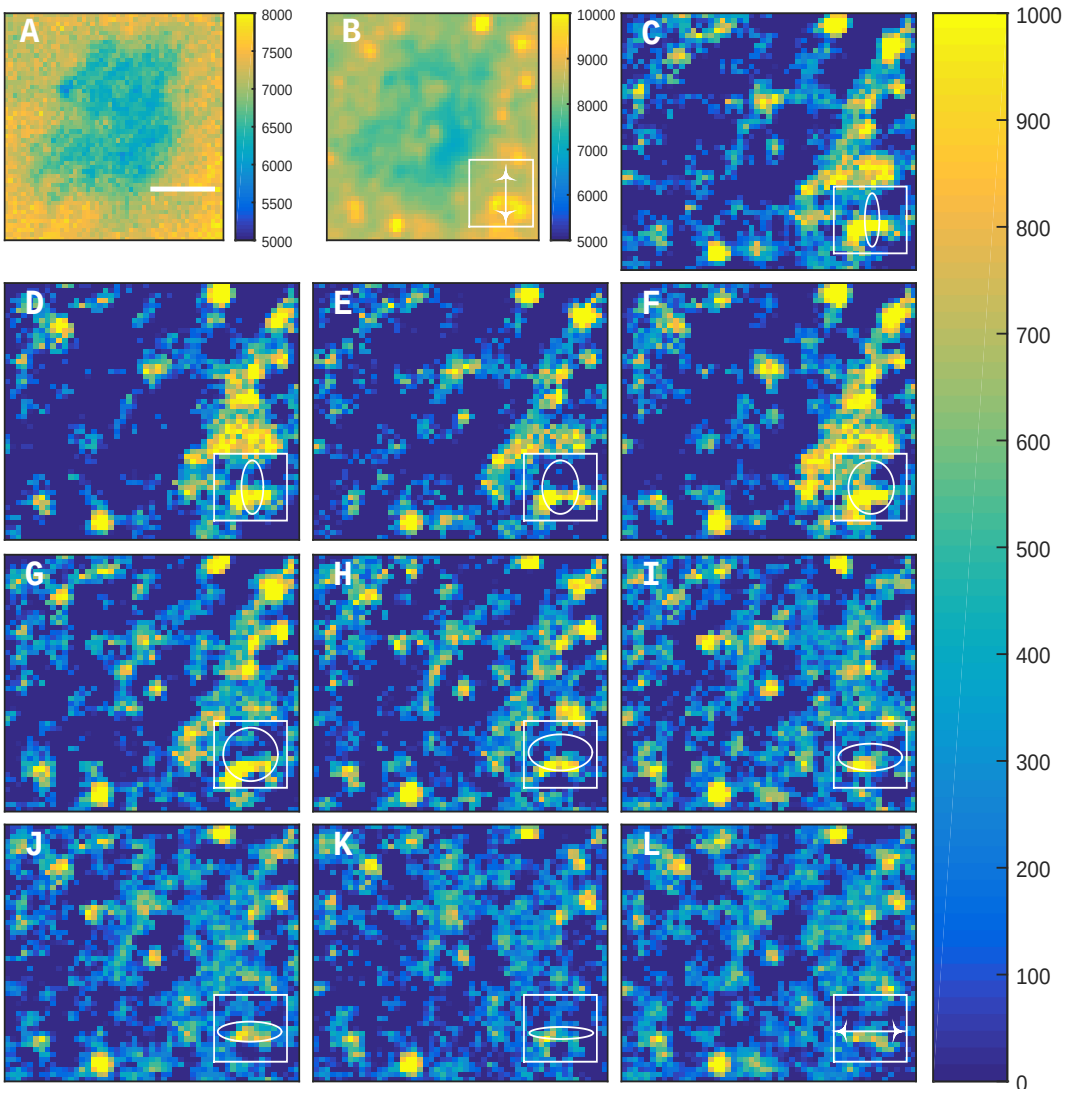

Figure 4.12: Contrast for linear and elliptic channels for *in vivo* measurements on dorsal side of a human hand. Panel A is the histogram of the Cross-linear channel tracing the shape of the mole. Panel B is the contrast of the subtraction of linear(co and cross) channels. Panel C-L are the contrasts for Multi-Polarization Difference Imaging (MPDI) at 0°, 10°, 20°, 30°, 40°, 45°, 50°, 60°, 70°, 80° and 90° respectively. Scale bar (Panel A), 0.5mm. Wavelength, 633nm. Image exposure time, 1500ms. Behaviour of the polarized light (linear/elliptical) is represented at the bottom-right corner of each panel. Panels A and B are raw images and have their own colorbar. Panels C-L have a common colorbar represented at the right border of the image.

Burn Scar

A scar on the dorsal side of a volunteer's hand was observed at 633nm and the compared results of the two subtraction methods is shown in Figure 4.14. Panels 1-2 show the subtracted images of EPDI and Panels 3-4 show the results of MPDI. It is evident from the images that the contrast is more enhanced in Panels 3-4 when compared to Panels 1-2 along with an increase in intensity of polarization maintaining photons. It can also be observed that the scar is quite clearly outlined in images with higher ellipticity (Panel 4 corresponding to circularly polarized channel at 45°). When comparing Panel 1-2 and Panels 3-4, it is evident that we are accessing different volumes and avoiding over-subtraction of photons. It can also be observed that Panel 4 shows the clear appearance of some structures/wrinkles when compared to Panel 3, suggesting that these structures lie deeper than the layer probed with Panel 3 (corresponding to ellipticity of 20°).

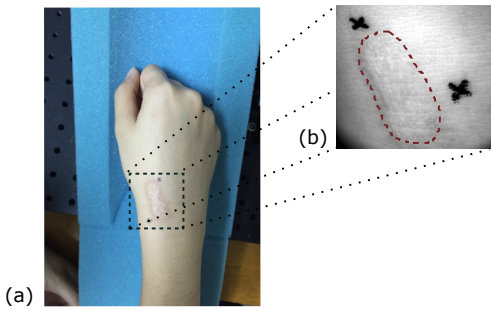

Figure 4.13: (a) Image of dorsal side of a hand showing a burn scar, (b) Zoom-out image of the burn scar. Images taken in white light.

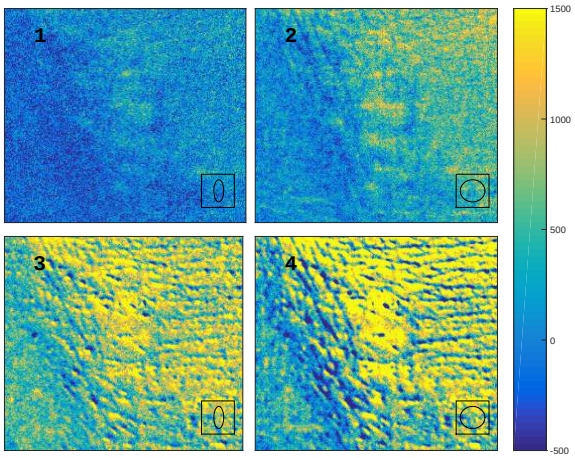

Figure 4.14: Contrast for elliptic channels of *in vivo* measurements on dorsal side of a human hand containing a scar. Panels 1-2 are the result images of Elliptical Polarization Difference Imaging (EPDI) at 20°and 45°respectively. Panels 3-4 are the result images of Multi-Polarization Difference Imaging (MPDI) at 20°and 45°respectively. Wavelength, 633nm. Image exposure time, 1500ms. Elliptical behaviour of the polarized light is represented at the bottom-right corner of each panel. Panels 1-4 have a common colorbar represented at the right border of the image.

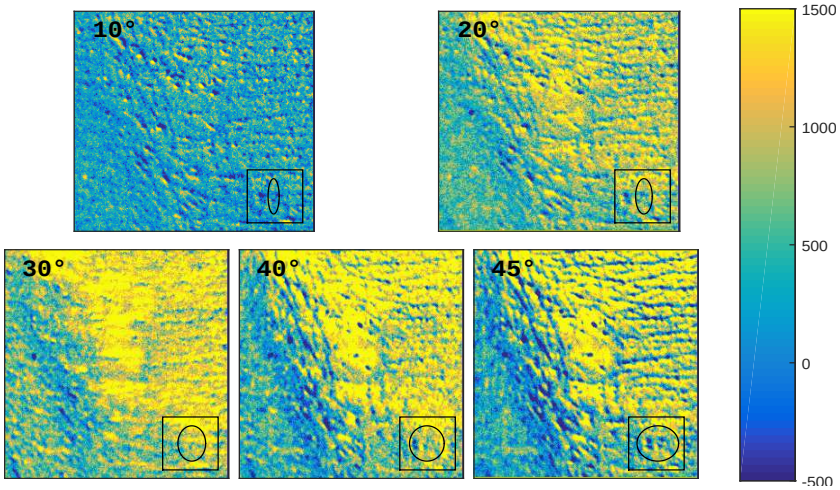

Figure 4.15: Multi-Polarization Difference Imaging (MPDI) contrast for elliptic channels of *in vivo* measurements on dorsal side of a human hand containing a scar. Panels 1-5 are the result images of Multi-Polarization Difference Imaging (MPDI) from 10°to 45°respectively. Wavelength, 633nm. Image exposure time, 1500ms. Elliptical behaviour of the polarized light is represented at the bottom-right corner of each panel. Panels 1-5 have a common colorbar represented at the right border of the image.

4.1.3.2 *Exposed cortex of an anaesthetized rat*

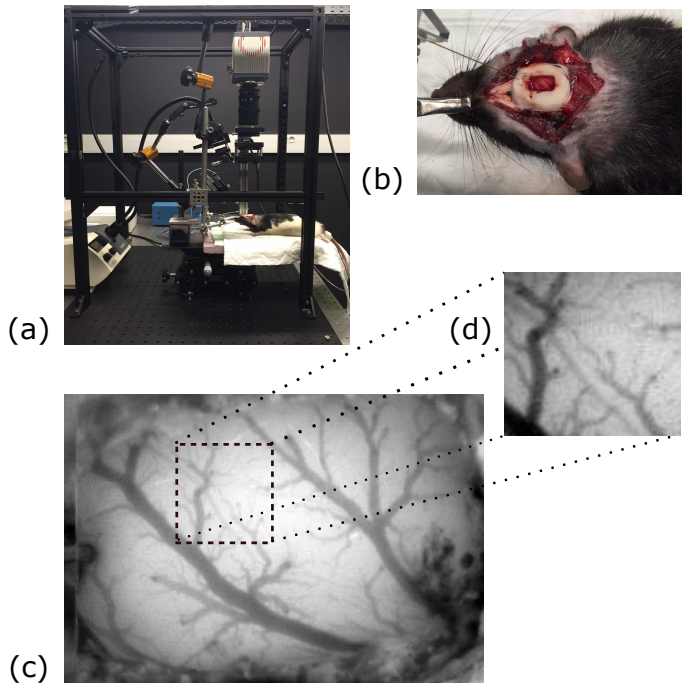

Figure 4.16: a) Photo of the *in vivo* set-up for imaging the Rat brain cortex. b) Image of the exposed cortex of an anaesthetized rat. c) Cross-linear image of the cortex. d) Zoom-out (Cross-linear) of the vessels under study for the *in vivo* experiments.

A network of blood vessels having different sizes can be seen in the white light image (Figure 4.16) and the portion of the image we have focussed on (seen in the zoom-out) shows two distinct large vessels which are superficial and can be seen in all the channels. A comparison between EPDI and MPDI are represented in Figures 4.17 and 4.18. The cross-linear image (Panel A in Figures 4.17 and 4.18), which shows the deepest (probeable) structures, show the existence of other smaller vessels. EPDI images show very poor contrast and signal due to the highly scattering nature of the rat brain, and the image quality is quite poor. But in the case of MPDI images, the vessels which are clearly in the sub-surface can only be seen in the elliptical channels (Panels C-L) and not in the linear channel (Panel B). Also with increase in the ellipticity, there is more signal intensity observed in the smaller vessels (upto 45° after which it decreases).

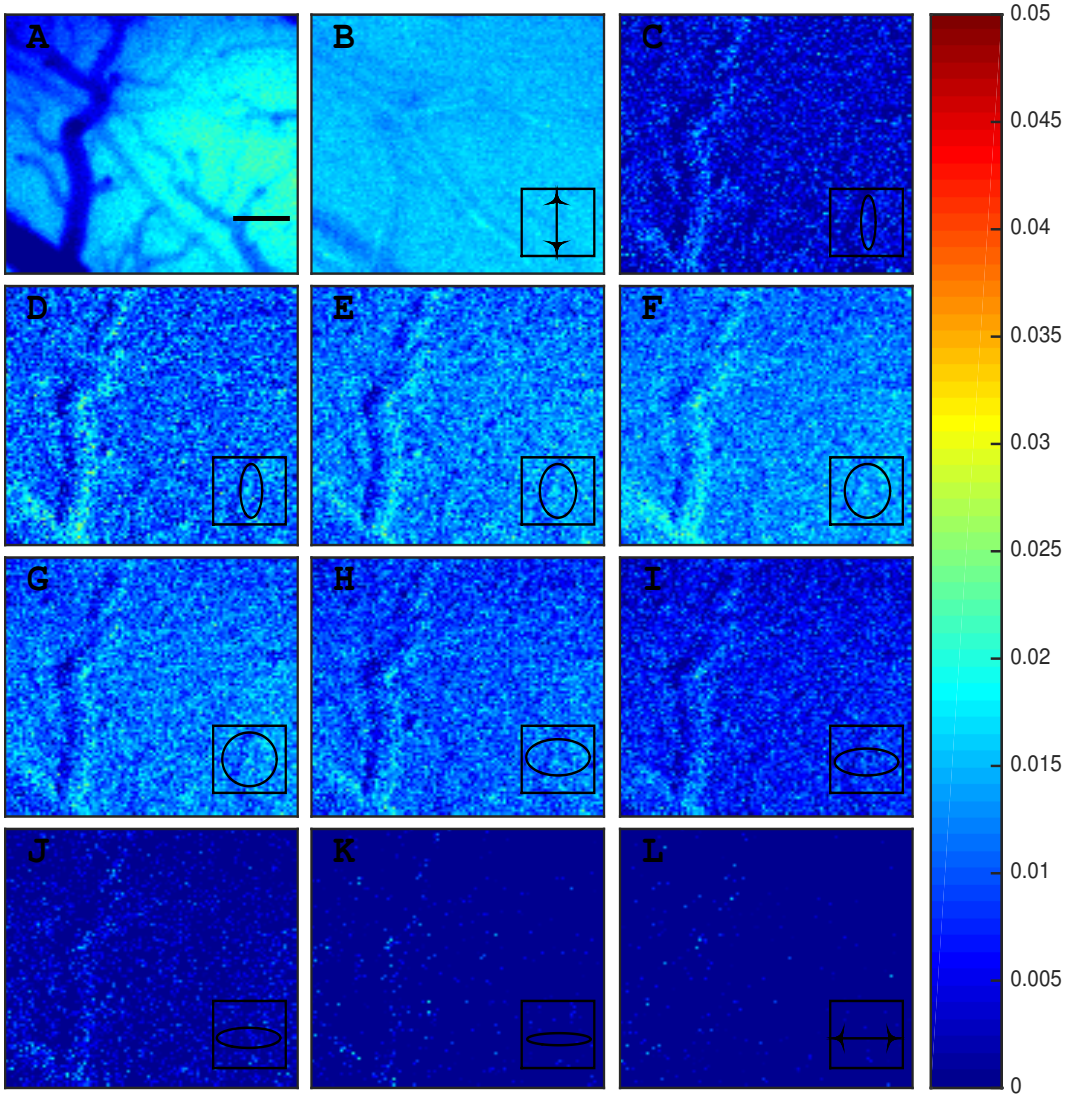

Figure 4.17: Elliptical Polarization Difference Imaging (EPDI) contrast for linear and elliptic channels for *in vivo* measurements on exposed cortex of an anaesthetized rat. Panel A is the Cross-linear channel. Panel B is the contrast of the subtraction of linear (co and cross) channels. Panel C-L are the contrasts for EPDI at 0°, 10°, 20°, 30°, 40°, 45°, 50°, 60°, 70°, 80°and 90° respectively. Scale bar (Panel A), 0.5mm. Image exposure time, 2000ms. Wavelength, 633nm. Behaviour of the polarized light (linear/elliptical) is represented at the bottom-right corner of each panel.

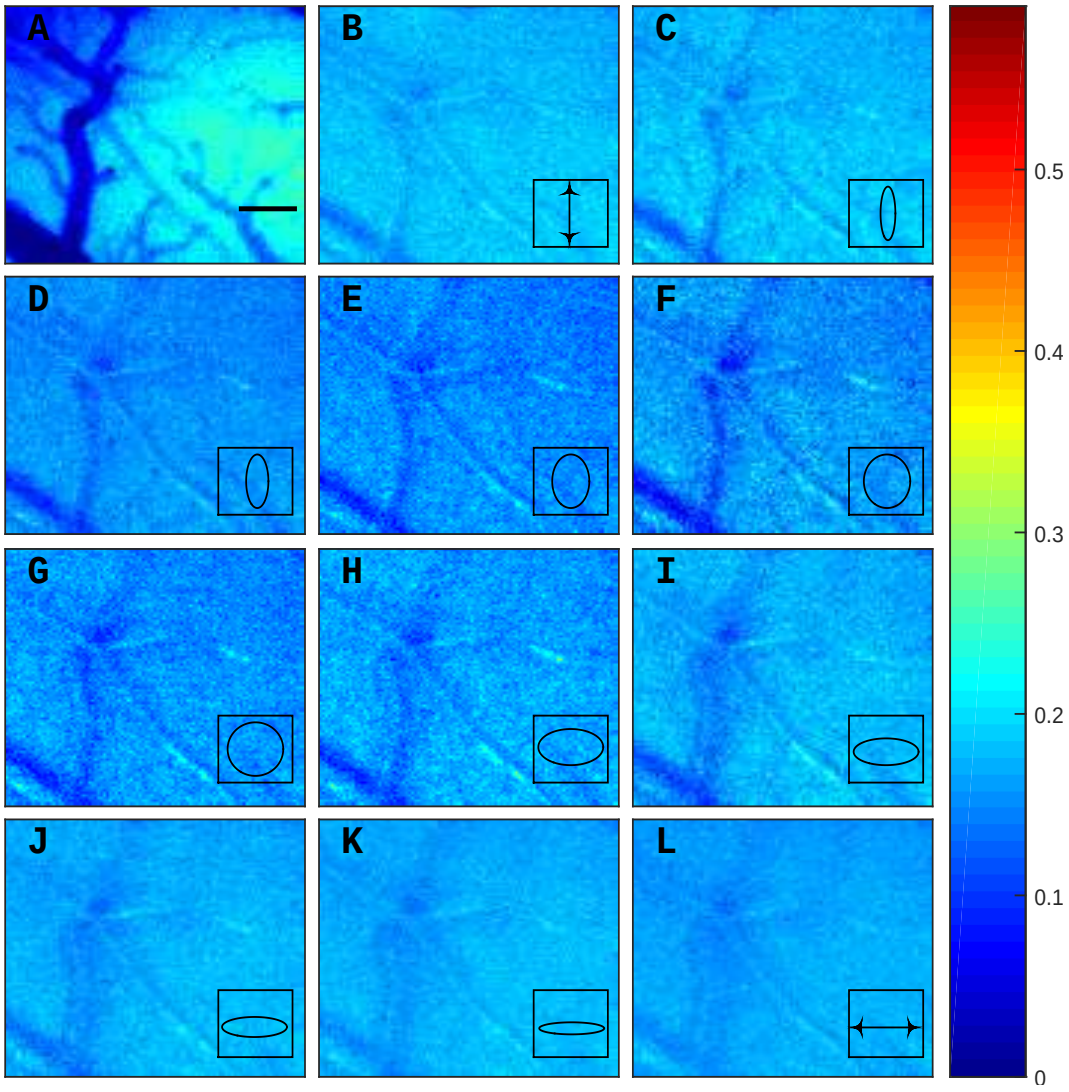

Figure 4.18: Multi-Polarization Difference Imaging (MPDI) contrast for linear and elliptic channels for *in vivo* measurements on exposed cortex of an anaesthetized rat. Panel A is the Cross-linear channel. Panel B is the contrast of the subtraction of linear(co and cross) channels. Panel C-L are the contrasts for MPDI at 0°, 10°, 20°, 30°, 40°, 45°, 50°, 60°, 70°, 80°and 90° respectively. Scale bar (Panel A), 0.5mm. Image exposure time, 2000ms. Wavelength, 633nm. Behaviour of the polarized light (linear/elliptical) is represented at the bottom-right corner of each panel.

4.2 ACCESSING DEEPER REGIONS

A network of blood vessels seen from the exposed cortex of an anaesthetized rat (See Figure 4.16) was further studied for looking into the details of depth of the vasculature. Figure 4.19 shows a comparison of the raw intensity images of all four imaging channels, C1-C4. Visual observation and further quantification showed that channel C4 (be it any angle of ellipticity) shows clear appearances of more number of vessels as compared to the co-elliptical channel, C3. This fact is made clear by the fact that, some vessels which are not observed in the co-linear channel, C1 are seen clearly in the counter-elliptical channel confirming that they lie deeper than the other vessels. The C4 channel (although contains some part of the specular content) gives us access to deeper structures than the Cross-linear channel (C2), provided the specular is out of the field-of-view. It gives us a mixture of the superficial as well as the depth content as can be observed in Panels D and F of Figure 4.19. As compared to the current practice of using the C2 channel to access the deepest-possible regions, this approach could further help us in identifying and quantifying some deep-lying structures with the use of the counter-elliptical channel.

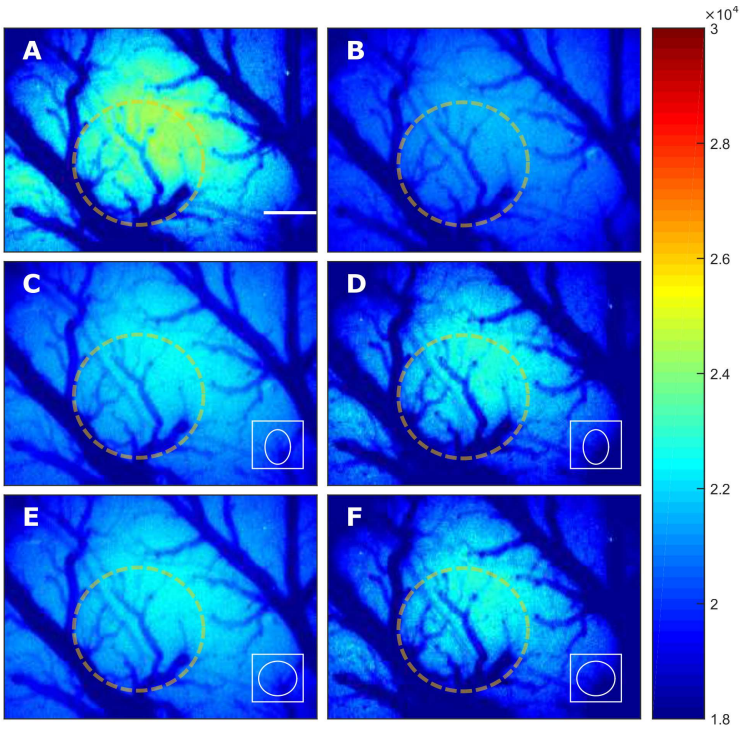

Figure 4.19: Comparison of raw intensity images for all four channels, C1-C4 for *in vivo* measurements on exposed cortex of an anaesthetized rat. Panel A is the Co-linear channel (C1). Panel B is the Cross-linear channel (C2). Panel C and D are Co-elliptical channel (C3) and Counter-elliptical channel (C4) respectively at an ellipticity of 30°. Panel E and F are Co-elliptical channel (C3) and Counter-elliptical channel (C4) respectively at an ellipticity of 45°. Yellow circle represents the ROI where most changes in intensity of vessels can be seen. Scale bar (Panel A), 0.5mm. Behaviour of the polarized light (elliptical) is represented at the bottom-right corner of each panel.

4.3 SUMMARY

In this chapter, we testify the feasibility of depth examination by tuning the state of polarization in four imaging channels, and compare two systems of image subtraction with experiments on calibrated Intra-lipid® phantoms, *ex vivo* and *in vivo* tissues. Intra-lipid® measurements confirm that MPDI involving all the four imaging channels is superior to EPDI because: (a) there is higher signal intensity (b) there is a higher contrast in surface structures (c) it allows probing a depth of $7mm$. Our phantom experiments show that this method can be used to probe tissues in depth up to at least $0.7mm$, which offers the possibility of screening a variety of layered biological tissues such as skin as tested here. *Ex vivo* experiments on chicken neck and Human skin experiments conform with the above conclusions, and show higher signal intensity and higher contrast of some structures with elliptic channels (from $0°$ to $45°$) probing sub-surface structures. Further work includes removal of the specular reflection at the surface using better and more adapted optical clearing agents. This could lead a more efficient isolation of the polarization maintaining photons. Besides, the cross-linear channel has the highest SNR, and this needs to be improved for the elliptic channels to get a better contrast of the sub-surface structures.

As an other application, the Counter-elliptical channel (C4) can be used to extensively study the depth of the structures under study, as against the usual methods of using Cross-linear channel (C2) for accessing the deepest structures. This could help clinicians in practice of using polarimetry for studying the maximum depth probed.

The other important aspect discussed in this chapter is image processing. Although MPDI is more efficient and superior to its contemporaries, the Signal-to-noise Ratio (SNR) achieved is quite low and questionable. MPDI allows depth probing with each increment in ellipticity, and with deeper volumes the quantity of measured photons reduces, thus dropping the SNR with increase in depth. For *in vivo* (mostly) imaging, the occurrence of motion artefacts is quite high. A motion registration algorithm was developed to correct for this shift in coordinates (of the order of 10s of $pixels$) based on in-built `MATLAB` functions. The registration method although quite accurate in most cases did have a residual shift of ± 1 $pixel$. This could be solved with more advance understanding of image processing and application of sophisticated movement correction algorithms.

5 DEPTH-RESOLVED SPECTROSCOPY WITH ELLIPTICALLY POLARIZED LIGHT

This chapter describes a protocol of deep sub-surface imaging in tissues demonstrated by employing both spectral and polarization discrimination of the backscattered photons. This technique allows for selectively accessing and enhancing sub-surface tissue layers via processing of the depolarized images obtained using polarized illumination at different wavelengths and accessing chromophores in biological tissues. The samples were illuminated with different wavelengths and processed using Multi-Polarization Difference Imaging (MPDI) (for removal of multiple-scattered components) involving images at these wavelengths. *In vivo* experiments were performed on skin abnormalities of volunteers and on exposed rat cortex to confirm the results of polarization subtraction and to allow for spectroscopic measurement of tissue chromophores.

5.1 INTRODUCTION

Spectrophotometry, or more specifically Diffuse Reflectance Spectroscopy (DRS) in the visible and NIR spectral ranges is an efficient and popular technique for non-invasive characterisation of various biological tissues. This method helps us extract information about the absorption and scattering properties of light of the examined tissues. Correlation of these optical properties with histological and biochemical characteristics provides a wealth of information regarding tissue composition, morphology, physiology as well as the early detection and diagnosis of various diseases. *In vivo* spectrophotometry of tissues focuses on the measurement of relative concentrations of number of tissue chromophores like haemoglobin in both oxygenated and de-oxygenated states [Friedland et al., 2003; Zonios et al., 1999], melanin, present in the epidermal tissue, and whose relative concentration variations are responsible for skin pigmentation [Zonios et al., 2001], bilirubin [Bhutani et al., 2000] and many others. Of the several applications of DRS, measurement of tissue oxygenation is one of the most important parameters in the diagnosis and therapeutic assessment of many diseases. Tissue oxygenation, in other words, is a measure of the percentage of oxygen that haemoglobin (carrier of oxygen in blood) is loaded with in blood *in vivo*. Since the molecular extinction spectra of Oxyhaemoglobin (HbO_2) and Deoxyhaemoglobin (Hb) are not equal, it can efficiently characterize blood oxygenation and various methods have been developed to measure these parameters. With this basis, it is possible to quantify the concentrations of many other tissue chromophores like melanin, fat, water etc. Most of these methods have their own limitations in terms of accuracy, invasiveness, time-constraint, cost etc.

Tissues being multi-layer structures, often undergo changes in their composition which are depth-dependent leading to pathological conditions. Therefore, the necessity to ex-

tract information about tissue chromophores at different depths becomes imperative. Out of the optical techniques that are being used to access depth information, polarization gated spectroscopy and imaging has become quite competitive because of the property of polarized photons to retain their incident polarization for a number of Mean Free Path (MFP)s depending on tissue optical properties. Due to the concept of 'polarization memory' (discussed in detail in Section 2.5), circularly polarized light maintains its polarization in highly scattering media at greater depths as compared to linearly polarized light and it is advocated to use elliptically/circularly polarized light for depth-resolved reflectance spectroscopy.

In this thesis, we have developed an algorithm based on the generalised form of Modified Beer-Lambert's Law (MBLL) which revolves around a generalized theory that allows estimation of chromophore concentrations. We have adapted this theory for mapping concentrations of cutaneous tissue chromophores from multi-wavelength images that have been processed by Multi-Polarization Difference Imaging (MPDI).

5.2 SPECTROSCOPY: THEORY

To set the theoretical context for our analysis, the modified Beer-Lambert law applied for the measurements of concentrations of different tissue chromophores is reviewed and developed to our purpose. Let us consider a non-scattering medium for which, the absorbance A, of light passing through the medium is related to it's relative absorption by the Beer-Lambert law [Hebden et al., 1997],

$$A(\lambda) = \mu_a(\lambda) d \tag{5.1}$$

where μ_a is the absorption coefficient, d is the path length through the medium and λ is the optical wavelength in the medium. Also, μ_a is represented as the sum of products of the specific molecular extinction coefficients, ϵ_i (expressed in units, L mol^{-1} mm^{-1}) and concentrations, ρ_i (expressed in units, mol L^{-1}), of the M absorbing species present in the medium,

$$\mu_a(\lambda) = \sum_{i=1}^{M} \epsilon_i(\lambda)\rho_i \tag{5.2}$$

To make up for the scattering losses, compensate for the total physical path length and to assess the non-linearity of A and μ_a, the total attenuation is represented by the Modified Beer-Lambert's Law (MBLL) [Cooper et al., 1996; Delpy et al., 1988; Matcher et al., 1994; Sassaroli and Fantini, 2004; Wyatt et al., 1990] given by,

$$A(\lambda) = G + \mu_a(\lambda) DP_l(\lambda) \tag{5.3}$$

where G is assumed to be an offset in attenuation purely due to scattering and DP_l is the differential path length, defined as $DP_l(\lambda) = \partial A(\lambda)/\partial \mu_a(\lambda)$ [Arridge et al., 1992]. This can further be expressed as (substituting from Eq. 5.2),

$$A(\lambda) = G + \sum_{i=1}^{M} \epsilon_i(\lambda)\rho_i.DP_l(\lambda) \tag{5.4}$$

Let us start by considering the chromophores, oxyhaemoglobin (ρ_{oxy}) and deoxyhaemoglobin (ρ_{deoxy}) concentrations for which the apparent absorption depends on factor G, which is supposed to be independent of wavelength and takes into account light scattering by the tissue. The apparent attenuation involving these two absorbing species, can be described as,

$$A(\lambda) = G + [\epsilon_{oxy}(\lambda)\rho_{oxy} + \epsilon_{deoxy}(\lambda)\rho_{deoxy}]DP_l \tag{5.5}$$

where $\epsilon_{oxy}(\lambda)$ and $\epsilon_{deoxy}(\lambda)$ are the extinction coefficients of oxy- and deoxyhaemoglobin at a given wavelength, λ, respectively (expressed in $cm^{-1}/mol/L$). Since the contributions of μ_a and d cannot be isolated, the concentrations of chromophores can only be calculated as a ratio, given by $R = \rho_{oxy}/\rho_{deoxy}$, which is rewritten in Equation 5.5 as,

$$A(\lambda) = G + [\epsilon_{oxy}(\lambda)R + \epsilon_{deoxy}(\lambda)]\alpha_s \tag{5.6}$$

where $\alpha_s = DP_l\rho_{deoxy}$. Thus as seen in the works of Stockford et al. [2007], it is possible to eliminate the measurement of G (back-scattered attenuation due to scattering) with a set of differential measurements of A to give an estimate of R, R'. Measurements at two wavelengths make it possible to now express G in terms of R' as,

$$G = \frac{A(\lambda_2)[R'\epsilon_{oxy}(\lambda_1) + \epsilon_{deoxy}(\lambda_1)] - A(\lambda_1)[R'\epsilon_{oxy}(\lambda_2) + \epsilon_{deoxy}(\lambda_2)]}{R'[\epsilon_{oxy}(\lambda_1) - \epsilon_{oxy}(\lambda_2)] + [\epsilon_{deoxy}(\lambda_1) - \epsilon_{deoxy}(\lambda_2)]} \tag{5.7}$$

Taking measurements at a third wavelength, λ_3, with measurements of either of the two wavelengths as Equation 5.5 and solving the set of linear equations will give us the expression,

$$R' = \frac{\epsilon_{deoxy}(\lambda_2)[A(\lambda_3) - G] - \epsilon_{deoxy}(\lambda_3)[A(\lambda_2) - G]}{\epsilon_{oxy}(\lambda_3)[A(\lambda_2) - G] - \epsilon_{oxy}(\lambda_2)[A(\lambda_3) - G]} \tag{5.8}$$

Combining Equations 5.7 and 5.8, the system of three wavelengths can be expressed as,

$$\begin{aligned}
&R'^2\epsilon_{deoxy}(\lambda_2)\left\{\begin{array}{l} A(\lambda_1)[\epsilon_{oxy}(\lambda_1) - \epsilon_{oxy}(\lambda_2)] \\ +A(\lambda_2)[\epsilon_{oxy}(\lambda_1) - \epsilon_{oxy}(\lambda_3)] \\ +A(\lambda_3)[\epsilon_{oxy}(\lambda_2) - \epsilon_{oxy}(\lambda_1)] \end{array}\right\} \\
&+R'\left\{\begin{array}{l} A(\lambda_1)\{\epsilon_{oxy}(\lambda_1)[\epsilon_{deoxy}(\lambda_3) - \epsilon_{deoxy}(\lambda_2)] + \epsilon_{deoxy}(\lambda_1)[\epsilon_{oxy}(\lambda_3) - \epsilon_{oxy}(\lambda_2)]\} \\ +A(\lambda_2)[2\epsilon_{oxy}(\lambda_1)\epsilon_{deoxy}(\lambda_1) - \epsilon_{oxy}(\lambda_1)\epsilon_{deoxy}(\lambda_3) - \epsilon_{oxy}(\lambda_3)\epsilon_{deoxy}(\lambda_1)] \\ +A(\lambda_3)[\epsilon_{oxy}(\lambda_1)\epsilon_{deoxy}(\lambda_2) + \epsilon_{oxy}(\lambda_2)\epsilon_{deoxy}(\lambda_1) - 2\epsilon_{oxy}(\lambda_1)\epsilon_{deoxy}(\lambda_1)] \end{array}\right\} \\
&+\epsilon_{deoxy}(\lambda_1)\left\{\begin{array}{l} A(\lambda_1)[\epsilon_{deoxy}(\lambda_3) - \epsilon_{deoxy}(\lambda_2)] \\ A(\lambda_2)[\epsilon_{deoxy}(\lambda_1) - \epsilon_{deoxy}(\lambda_3)] \\ A(\lambda_3)[\epsilon_{deoxy}(\lambda_2) - \epsilon_{deoxy}(\lambda_1)] \end{array}\right\} = 0
\end{aligned} \tag{5.9}$$

Further simplifying Equation 5.9 to find the roots of the polynomial and possible values of R',

$$R' = -\frac{\epsilon_{deoxy}(\lambda_1)}{\epsilon_{oxy}(\lambda_1)} \tag{5.10a}$$

$$R' = \frac{\left\{\begin{array}{c} A(\lambda_1)[\epsilon_{deoxy}(\lambda_2) - \epsilon_{deoxy}(\lambda_3)] + A(\lambda_2)[\epsilon_{deoxy}(\lambda_3) - \epsilon_{deoxy}(\lambda_1)] \\ +A(\lambda_2)[\epsilon_{deoxy}(\lambda_1) - \epsilon_{deoxy}(\lambda_2)] \end{array}\right\}}{\left\{\begin{array}{c} A(\lambda_1)[\epsilon_{oxy}(\lambda_3) - \epsilon_{oxy}(\lambda_2)] + A(\lambda_2)[\epsilon_{oxy}(\lambda_1) - \epsilon_{oxy}(\lambda_3)] \\ +A(\lambda_2)[\epsilon_{oxy}(\lambda_2) - \epsilon_{oxy}(\lambda_1)] \end{array}\right\}} \tag{5.10b}$$

Since the first solution (Equation 5.10a) is negative and is not physical, the second solution (Equation 5.10b) is used to estimate R and provides a generalized solution for R′.

Stockford et al. [2007] used a Monte-Carlo model that combined Stokes-Mueller scheme to simulate light propagation in a scattering medium with Mie scatterers and $g = 0.9$. This method allowed measurement of G and α_s that were equivalent to previous measurements [Ramella-Roman et al., 2005] and these values were found to be constant as a function of wavelength with polarization gating allowing more filtering of inherent scattering to some extent.

Stockford et al.'s model does not take into account the actual existence of a dependence of the scattering term, G and the backscattering path-length, DP_l with the wavelength. Nevertheless, several techniques such as polarization subtraction gating and special filtering will allow the user to limit the depth of penetration to a known value. To estimate R for user-defined depths in biological tissues, we can use the images taken at different ellipticities and different wavelengths (at least 3) treated with Multi-Polarization Difference Imaging (MPDI). To be able to apply the generalized solution for the estimation of R to images at different wavelengths, one must access the same volume in all the images chosen. And for this, we need to relate and chose images based on their wavelength and ellipticity which corresponds to the same depth probed.

5.3 DEPTH PROBING USING POLARIZATION GATING: ACCESSING USER-DEFINED DEPTHS

In the previous chapter, we saw the results of the MPDI method and the kind of information that can be retrieved. It is shown that with increasing ellipticities, we can probe different volumes (that are increasing in depth probed), and each wavelength corresponds to a range of depths, depending on the optical properties, i. e. absorption (μ_a) and scattering (μ_s). One can also verify that there is no intersection between volumes probed by depolarized and by polarized light. But it is still important to quantify the depth that can be accessed with each ellipticity and each wavelength. To develop this 3D relationship between *Wavelength-Ellipticity-Depth*, we will use the optical properties of tissue as calculated by Zonios and Dimou [2006] and the ellipticity-dependent Mean Visitation Depth (MVD) as calculated by Rehn et al. [2013] from Monte-Carlo simulations.

Zonios and Dimou [2006] proposed and developed a model for Diffuse Reflectance Spectroscopy (DRS) with fibre optic probes and validated this model by testing on tissue phantoms. They then applied the model to the analysis of diffuse reflectance spectra collected

Table 5.1: Absorption and reduced-scattering co-efficients (both in mm^{-1}) of human skin determined *in vivo* by Zonios and Dimou [2006]

Wavelength (nm)	μ_a (mm^{-1})	μ_s' (mm^{-1})	Wavelength (nm)	μ_a (mm^{-1})	μ_s' (mm^{-1})
360	-	2.25	560	-	1.92
370	-	2.23	570	-	1.90
380	-	2.22	580	0.27	1.88
390	-	2.20	590	-	1.87
400	1.61	2.18	600	0.06	1.85
410	2.42	2.17	610	-	1.83
420	2.92	2.15	620	0.02	1.82
430	2.93	2.13	630	-	1.80
440	1.44	2.12	640	0.01	1.78
450	0.40	2.10	650	-	1.77
460	0.19	2.08	660	0.01	1.75
470	-	2.07	670	-	1.73
480	0.12	2.05	680	0.01	1.72
490	-	2.03	690	-	1.70
500	0.11	2.02	700	0.01	1.68
510	-	2.00	710	-	1.67
520	0.16	1.98	720	0.01	1.65
530	-	1.97	730	-	1.63
540	0.30	1.95	740	0.01	1.62
550	-	1.93			

from human skin *in vivo*. As a result of their calculations, they provided the optical properties of human skin at a range of wavelengths in the visible region of the spectrum and is illustrated in Table 5.1.

The Mean Visitation Depth (MVD) for different ellipticities that was calculated by Rehn et al. [2013] using Monte Carlo simulations for various range of optical properties is described in Section 2.6 and are illustrated in Figure. 2.11. Based on the optical properties in Table 5.1 and range of MVD in Figure. 2.11, we can further calculate the probe-able depths at each ellipticity and wavelength respectively. This 3D relation between *Wavelength-Ellipticity-Depth* is summarized in Table 5.2 and in Figure. 5.1. Table 5.2 shows the probed depths that are accessible by polarization gating for each wavelength, and are in the range of a few hundreds of microns. This corresponds precisely to the volumes that need access in many applications such as in early skin cancer detection or screening of the exposed cortex (usually monitored with 2D IOS imaging techniques that do not offer any depth resolution). The present polarization gating technique, MPDI also provides functional information and

offers the advantage of being simple, with fast data acquisitions.

Table 5.2: Accessible depths at different wavelengths and ellipticities adapted from Rehn et al. [2013] and Zonios and Dimou [2006]

Wavelength (nm)	Mean Visitation Depth (MVD) (μm)				
	0π Rad	0.05π Rad	0.1π Rad	0.15π Rad	0.25π Rad
390	226	250	301	323	348
400	204	226	272	291	314
410	168	186	224	241	259
420	152	169	203	218	235
430	153	169	203	218	235
440	217	240	289	310	334
450	309	342	412	442	476
460	341	377	454	486	524
480	356	394	475	509	549
500	363	402	483	518	559
520	361	400	481	516	556
540	344	380	458	491	529
580	360	398	479	514	554
600	405	448	539	578	623
620	420	465	560	600	647
640	430	475	572	613	661
660	439	486	585	627	676
680	447	495	595	638	688
700	457	506	609	653	704
720	466	516	620	665	717
740	474	525	632	677	730

Similarly for rat brain tissues, we adopted the optical properties as measured by Mesradi et al. [2013] along with the MVD calculated by Rehn et al. to establish the relation between wavelength-ellipticity-depth. This study on rat brain samples was quite crucial for the understanding of spectroscopic measurements (discussed in Section 5.5). Mesradi et al. [2013] measured the optical properties of fresh and frozen tissues of rat heart, kidney, brain, liver, and muscle in the visible wavelength range using an integral sphere set-up and the 'inverse adding doubling' technique [Prahl et al., 1993]. It was found that the μ_s' for brain tissues was much higher than for any other structure for the range of wavelengths from $450 - 700$nm, and are listed in Table 5.3.

The possible penetration depths at each ellipticity and wavelength for rat brain tissue was calculated using Table 5.3 and the values of MVD from Rehn et al. (Figure 2.11) and is summarized in Table 5.4. The depths that can be probed are expressed graphically in

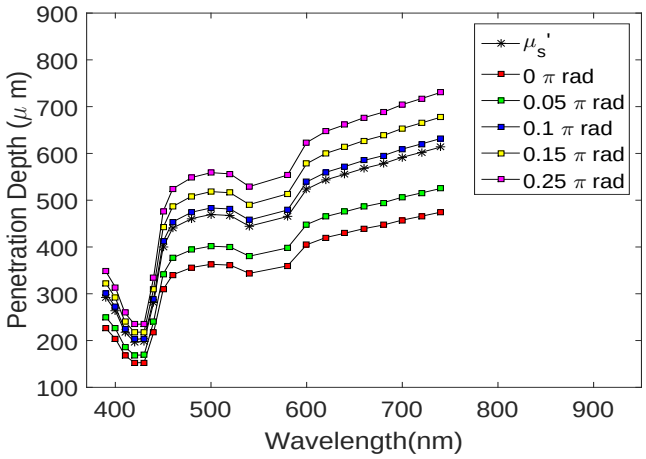

Figure 5.1: Graphical representation of the relationship between Wavelength-Ellipticity-Depth.

Table 5.3: Absorption and reduced-scattering co-efficients of rat brain cortex determined *ex vivo* from fresh rat brain tissue by Mesradi et al. [2013]

Wavelength (nm)	μ_a (mm^{-1})	μ_s' (mm^{-1})	Wavelength (nm)	μ_a (mm^{-1})	μ_s' (mm^{-1})
450	0.620	5.65	580	0.495	4.25
460	0.475	5.51	590	0.490	4.17
470	0.455	5.38	600	0.480	4.09
480	0.455	5.26	610	0.425	4.01
490	0.460	5.14	620	0.416	3.94
500	0.475	5.02	630	0.416	3.87
510	0.505	4.91	640	0.420	3.80
520	0.520	4.80	650	0.430	3.73
530	0.530	4.70	660	0.445	3.67
540	0.570	4.60	670	0.440	3.61
550	0.585	4.51	680	0.440	3.55
560	0.575	4.42	690	0.450	3.49
570	0.535	4.33	700	0.450	3.44

Figure 5.2 and the maximum penetration depth is about ~ 350μm that can be achieved with the circularly polarized light (at an ellipticity of 45°).

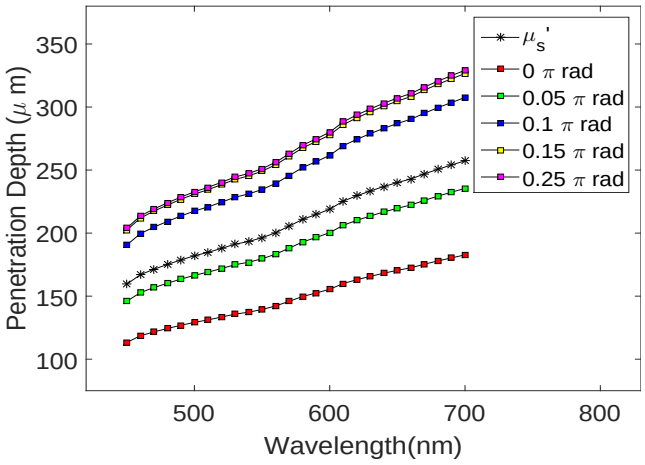

Figure 5.2: Graphical representation of the relationship between Wavelength-Ellipticity-Depth for rat brain cortex.

Table 5.4: Accessible depths at different wavelengths and ellipticities for fresh rat brain tissue adapted from Mesradi et al. [2013] and Rehn et al. [2013]

	Mean Visitation Depth (MVD) (μm)				
Wavelength (nm)	0π Rad	0.05π Rad	0.1π Rad	0.15π Rad	0.25π Rad
450	113	146	191	202	204
460	119	153	200	212	214
470	122	157	205	217	219
480	124	160	209	222	224
490	127	164	214	227	229
500	129	167	217	231	233
510	131	169	221	234	236
520	133	172	225	238	240
530	136	175	228	243	245
540	137	177	231	245	247
550	139	180	235	249	251
560	142	183	239	254	256
570	146	188	246	264	263
580	150	193	252	268	270
590	153	197	257	273	275
600	155	200	262	278	280
610	160	206	269	286	288
620	163	210	274	291	294
630	166	214	279	296	299
640	168	217	283	301	303
650	170	220	287	305	307
660	172	222	290	308	311
670	175	226	295	313	316
680	178	229	300	318	321
690	180	232	304	322	325
700	183	235	308	327	329

5.4 EXPERIMENTAL SET-UP AND CALIBRATION

The experimental set-up was as described in Section 3.2 and Figure 3.4. The axes of the optics were identified as described in Section 3.2.2. Images were taken in the four different channels (C1, C2, C3 and C4) with their different ellipticities (0°- 45°) in all the three different wavelengths mentioned. The methods described in Section 5.2 help in determining the absorber-concentration ratio for the case of detection of total intensity, and needs a normalization* to work with different illuminating wavelengths. In the work presented here, the normalization was done by standardizing to the exposure time, t_λ, and percentage of transmission through the optics. Table 5.5A shows the transmission of different optics and different wavelengths. For the whole set-up including the optics of the illumination and detection paths, the transmission coefficients can be normalized to one of the wavelengths to give rise to a transmission factor, $T(\lambda)$, for each wavelength used (See Table 5.5B). After determining the transmission factor, each image can be normalized by wavelength and exposure time by, $I_{norm} = (I_0 * T(\lambda))/t(\lambda)$. This form of normalization is not an absolute measurement, and is regarded as a relative quantity. After normalization of the images, they can be used to compute relative concentrations of different chromophores as described in Section 5.2.

* Normalization can be done by imaging a completely reflecting and non-scattering surface (e. g. white reference like a lambertien sample) to capture the full extent of the incident light and then normalizing that to the different wavelengths using the form $(\log I_0 - \log I)$. In our experiments, this method of normalization was not implemented.

Table 5.5: Transmission coefficients for different optical components for normalization of images taken under different wavelengths

A: INDIVIDUAL TRANSMISSION COEFFICIENTS FOR OPTICS USED IN SECTION. 5.4

	Transmission (%)			
	Red01 - 670nm	Red02 - 633nm	Yellow - 570nm	Green - 532nm
Illumination				
Light Source	-	-	-	-
Bandpass Filter - 633nm	70±0.5	-	-	-
Bandpass Filter - 670nm	-	70±0.5	-	-
Bandpass Filter - 570nm	-	-	48±0.5	-
Bandpass Filter - 532nm	-	-	-	51±0.5
Polarizer	81±0.5	79±0.5	76±0.5	70±0.5
Quarter-wave plate	97±0.5	97±0.5	97±0.5	97±0.5
Detection				
Quarter-wave plate	97±0.5	97±0.5	97±0.5	97±0.5
Polarizer	81±0.5	79±0.5	76±0.5	70±0.5
Lens	98±0.5	98±0.5	98±0.5	98±0.5
Detector/Camera	68±0.5	72±0.5	72±0.5	70±0.5

B: TRANSMISSION FACTORS FOR NORMALIZING WAVELENGTHS

Wavelength (nm)	Transmission Factor
670	1.0±0.1
633	1±0.1
570	0.40±0.1
532	0.25±0.1

5.5 RESULTS

First trials of spectroscopy with elliptically polarized light were tried on the *in vivo* images acquired from the exposed cortex of an anaesthetized rat (see Section 3.3 for sample preparation). Images were taken for ellipticities from 10° to 45° at three wavelengths 532nm, 633nm and 670nm respectively (with their molar extinction coefficients represented in Figure 5.3).

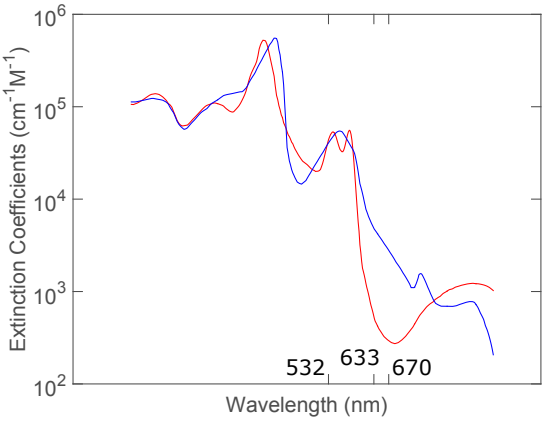

Figure 5.3: Absorption spectra for Oxyhaemoglobin (HbO_2) (red) and Deoxyhaemoglobin (Hb) (blue).]

5.5.1 *Mapping attenuation*

The starting point of any spectroscopic analyses is the measurement of absorption spectrum at a given wavelength as defined by Beer-Lambert's law (Eqn. 5.1). Attenuation (A) maps of polarization-gated images (MPDI) for different wavelengths can be seen in Figure 5.4 and it compares $A(\lambda)$ for different ellipticities 20°, 30°and 45° respectively. It also shows the kind of information/signal that can be accessed at different depths (translated from different ellipticities) for each wavelength.

Attenuation maps in Figure 5.4 elucidate the fact that at shorter wavelengths, blood is more absorbing with the evidence of many vessels and other vasculature, and also probe superficial depths. Attenuation which is mainly due to scattering is directly related to the Constant offset in attenuation (G) as described by the Modified Beer-Lambert's Law (MBLL). From these attenuation maps, it is then possible to isolate the absorption maps of the images using Eqn. 5.3, by estimating G as the minimum value of total attenuation (i.e. $G \simeq \min(A)$). To quantify the μ_a for images at different wavelengths and ellipticities, the mean absorption was plotted as a function of the wavelength at different ROIs (of size 10x10 pixels) and can be seen in Fig. 5.5. ROI-01 consisted of the background in the rat cortex, ROI-02 and ROI-03 consisted of two large vessels respectively. These vessels could be seen visually in the absolute intensity image and are highlighted in Figure 5.5a.

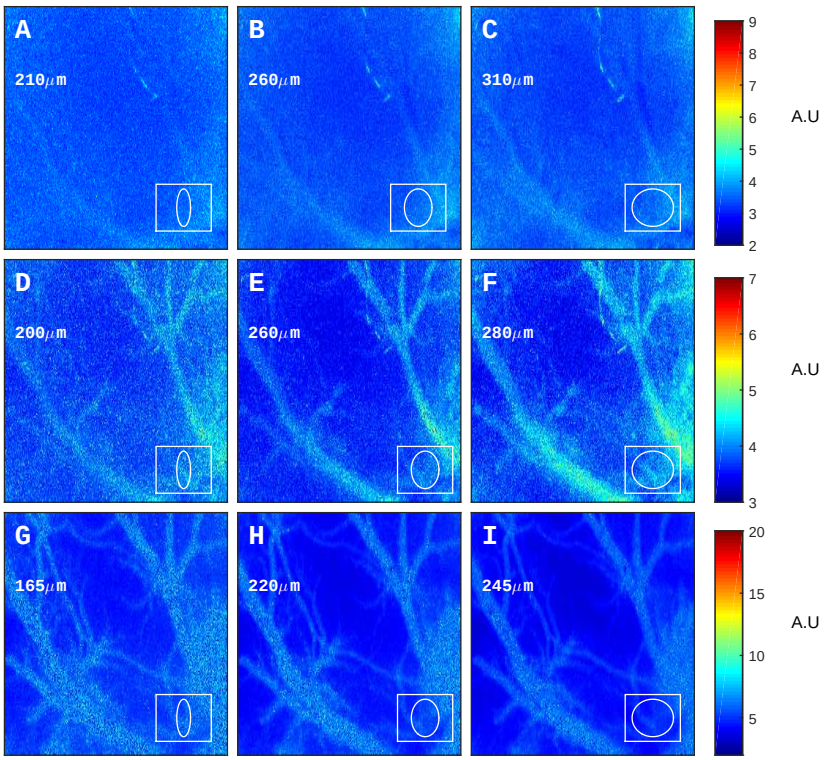

Figure 5.4: Attenuation (A) maps of MPDI images for different wavelengths and ellipticities for *in vivo* measurements on exposed cortex of an anaesthetized rat. Panels A-C: 670nm, Panels D-F: 633nm and Panels G-I: 532nm. The ellipticity of each image is represented at the bottom-right corner of each panel and is in the order 20°, 30°and 45° respectively. Each row (corresponding to a single wavelength) has a common colorbar represented at the right border of the image. Images from different wavelengths were normalized to their respective exposure times and transmission coefficients, so the units of comparison are in arbitrary units. The representative depths of each image is shown in the top-right corner, taken from Figure 5.2.

The absorption in the vessels was seen to be more than that of the background, but the actual values of μ_a were underestimated (as compared to the expected value) for all the three wavelengths. To recapitulate, the images were normalized to their respective exposure times and transmission coefficients, rendering the images of different wavelengths relative (expressed in arbitrary units) and not absolute. Hence it is impractical to compare these values to those in literature. However, our measurements suggest that the values of μ_a found are relative w.r.t wavelengths, and it can be shown, for example, that the absorption in 532nm wavelength is greater than that in 633nm wavelength by a factor of 3, i.e. $\mu_a(532nm) = 3\mu_a(633nm)$. This anomaly could be explained by the uncertainty in the normalization of the images to the reference. An error in the normalization of any one of the wavelengths affects the attenuation and leads to an underestimation of the constant G due to scattering. In comparison, the absorption for different wavelengths in both the vessels that were observed were similar for ROIs 2 and 3. Panels (c) and (d) in Figure 5.5, show that μ_a for the three wavelengths are in a similar range, confirming that the vessels have similar absorption, but there is not much information about the depth of these vessels.

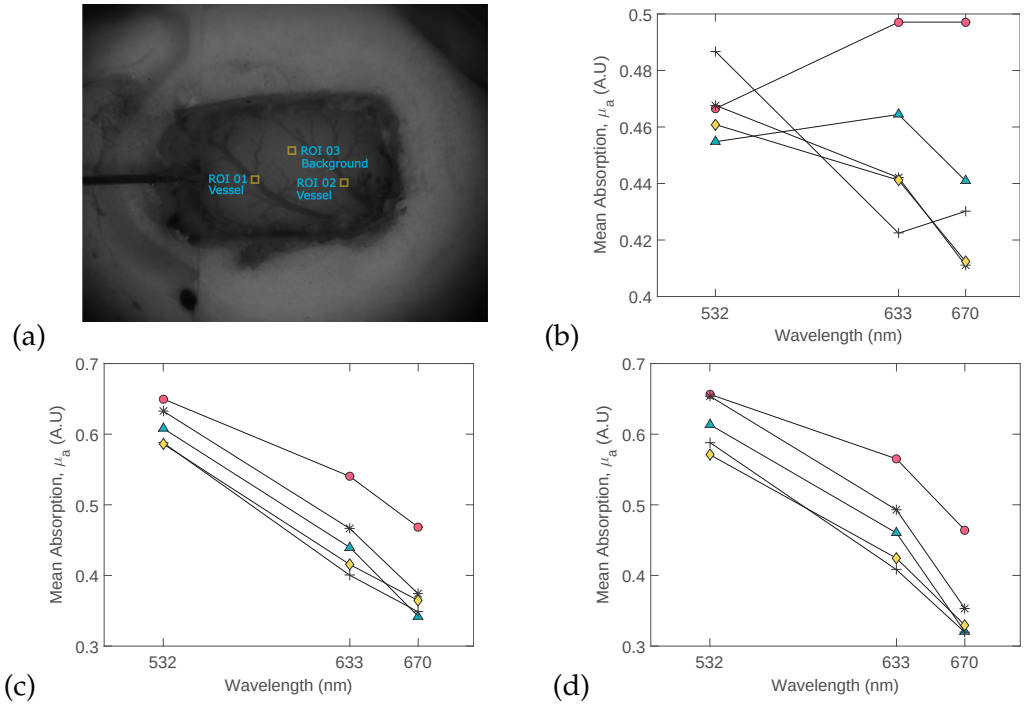

Figure 5.5: Mean absorption, μ_a, for *in vivo* images of exposed cortex of rat taken at different ROI where (a) Absolute intensity image of rat brain cortex with highlights of the three different ROI, (b) Mean μ_a for ROI-01 containing the background, (c) Mean μ_a for ROI-02, containing vessel (01), and, (d) Mean μ_a for ROI-03, containing vessel (01). The ellipticities are represented as circles (10°), asterisks (20°), triangles (30°), plus signs (40°) and diamonds (45°) respectively. Images from different wavelengths were normalized to their respective exposure times and transmission coefficients, so the units of comparison are in arbitrary units.

However, neglecting this drop in absorption values and improving the normalization process can lead to an important feature connecting the attenuation and isolating the absorption at different depths. This process of efficiently accessing the absorption spectrum at different depths is quite consistent and can be done using the different channels of ellipticity coupled with Multi-Polarization Difference Imaging (MPDI). Accessing absorption at user-defined depths without the need of information about the concentration of chromophores (either blood oxygen components, melanin or others) is quite an advantage and serves as a simple and consistent tool for the same.

5.5.2 *Chromophore concentrations*

Once we have an idea about the attenuation and more specifically the absorption maps of images at different wavelengths and thus different depths, the next step would be to quantify the concentrations of different chromophores, more specifically oxy- and deoxy-haemoglobin in our case. This can be carried out by applying our experimental images to Stockford et al.'s method of measuring R or R′ as described in Section 5.2. Images at three different wavelengths are needed to solve the system of equations and arrive at a concentration ratio for the chromophores. Considering the fact that each image of a particular

wavelength and a particular ellipticity corresponds to a particular volume in depth, it is imperative to use images that correspond to the same volume.

To be able to compare the same volumes, images from different wavelengths and ellipticities were chosen according to the values represented in Section 5.3. To get an idea about the achievable depths with different ellipticities for our chosen wavelengths, the appropriate depths can be seen plotted as a function of ellipticity and wavelength in Figure 5.6 (taken from Figure 5.2). Images from the rat brain cortex, taken at different ellipticities and wavelengths were analysed with MPDI to look at same volumes and are shown in Figure 5.7. The rat brain cortex although a highly scattering tissue structure, when imaged with our set-up showed the presence of vessels as deep as ~ 320µm (corresponding to the images taken at 670nm and 45° ellipticity). The chosen ellipticities for each wavelength are: 20° at 670nm, 20° at 633nm and 30° at 532nm which all correspond to a penetration depth of about 220µm.

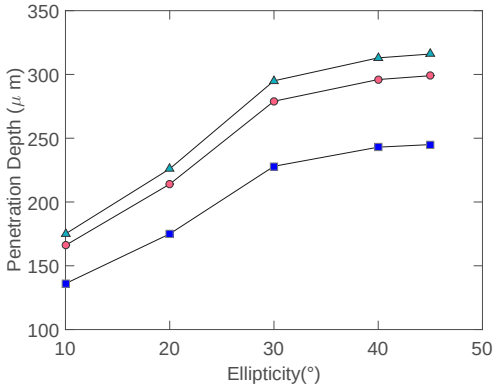

Figure 5.6: Penetration depths for different wavelengths and ellipticities for *in vivo* images of exposed cortex of rat taken from Figure 5.2 in Section 5.3 [Mesradi et al., 2013; Rehn et al., 2013]. 'Squares' represent 532nm, 'Circles' represent 633nm and 'Triangles' represent 670nm.

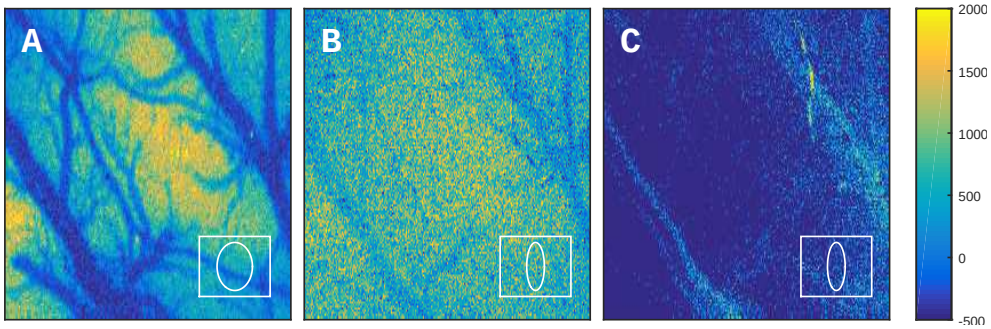

Figure 5.7: Comparison of MPDI images corresponding to the same volume from different wavelengths for *in vivo* measurements on exposed cortex of an anaesthetized rat. Panel A is 532nm, Panel B is 633nm and Panel C is 670nm. Behaviour of the polarized light (elliptical) is represented at the bottom-right corner of each panel. Images from different wavelengths were normalized to a mean intensity value and to their respective exposure times.

Panel A, at 532nm shows the presence of many vessels that are highly absorbing in the green wavelength. Panels B and C show lesser vessels at the same volume due to lower absorption of biological tissues at the red wavelengths. Now that we have information about the images at same volume from each wavelength, we can use these images (as they correspond to the wavelength-specific attenuation) in Eqn. 5.10 to estimate the ratio of concentration of chromophores, R', for oxy- (HbO_2) and deoxyhaemoglobin (Hb). The uncoupling of concentrations ρ_{oxy} and ρ_{deoxy} can be calculated using polarization gating with multiple wavelengths and their corresponding Mean Visitation Depth (MVD) with the assumption that we are dealing with similar path lengths, that should conform to the fact that Constant offset in attenuation (G) and Alpha factor for spectroscopy (α_s) are constant.

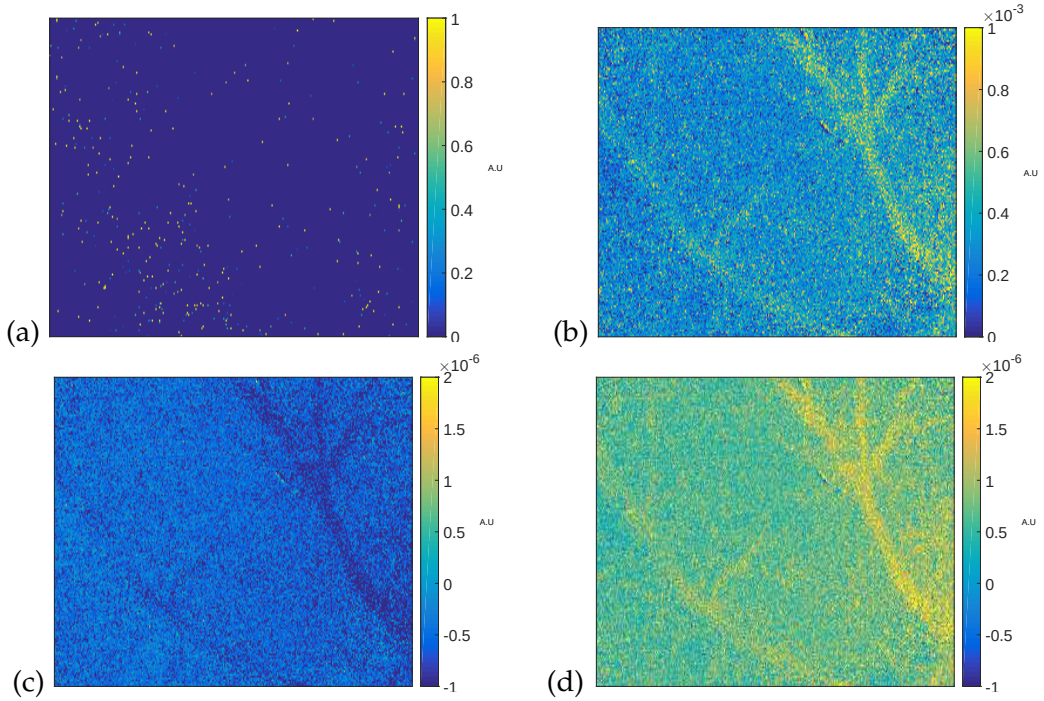

Figure 5.8: (a) Estimation of ratio of concentrations of two chromophores, R', (b) Alpha factor for spectroscopy (α_s), (c) Oxyhaemoglobin concentration (ρ_{oxy}), and, (d) Deoxyhaemoglobin concentration (ρ_{deoxy}) calculated for *in vivo* images of rat brain cortex by polarization spectroscopy using Multi-Polarization Difference Imaging (MPDI) technique. Individual colorbar is presented at right corner of each image. The images are all represented in arbitrary units.

As described in Section 5.2, the various quantities R', α_s, ρ_{oxy}, ρ_{deoxy} were computed for a set of images of the rat brain cortex taken *in vivo*. The respective images are represented in Figure 5.8. The quantities were measured as shown in the polarized spectroscopy technique presented in this thesis, and verified with the images chosen to represent a depth of 220µm (to look at the same volume). The solutions for R' (Figure 5.8a) were found to be negative, regarding the expression invalid. Unfortunately, the fact that G and α_s are constant is overridden by using our method of polarization gating. The values for α_s were found to be wavelength-specific, but with no certain dependence. The method also showed negative concentration of HbO_2 and Hb at some localised areas in the image, which led to inconsistent ratio of blood oxygenation inside the vessels. The main problem was with

the images from 532nm wavelength, which were found to be less absorbing than normal, which meant that G is supposed to be much smaller than it is found to be. The drop in absorption value of 532nm wavelength images by a factor of '3' leads to many repercussions on the calculation of R'. This drop in attenuation would mean that the sample is less scattering and more absorbing leading to a path length 3 times smaller than the normal value.

5.6 SUMMARY

In this chapter, it was shown that it is possible to get consistent information about attenuation of images at different depths by using a combination of Modified Beer-Lambert's Law (MBLL) and polarization gating using Multi-Polarization Difference Imaging (MPDI). This marks the stepping stone for merging polarization gating and spectroscopy, mainly for quantifying optical properties and concentration of chromophores at different penetration depths. Translating polarization gating into extracting spectroscopical information on concentration of chromophores needs to be studied in more detail. It was also shown that it is possible to get an idea of the Constant offset in attenuation (G), by estimating G as the minimum value of total attenuation (i.e. $G \simeq A_{min}$). The results of calculation of Estimate of R (R') lead to a negative value arising from the reduced absorption in the 532nm wavelength. More trials need to be conducted to get a better idea of the values of G and α_s. As a ramification of this erroneous value, the path lengths needed to examine this theory are very small. To achieve these smaller path lengths, it is advisable to use a more appropriate range of wavelengths as well as have a consistent normalization process. Also, by plugging in a smaller value of G (about 3 times smaller), gave a consistent result, indicating that the sample is less scattering than we believe it to be.

Depending on optical properties of the medium, the exact depth and extent of these subsurface volumes can be calculated and is represented in Section. 5.3 for both human tissues as well as rat brain tissues. With advancement in the set-up and better signal processing, this method should allow for imaging deeper volumes at specific/user-defined depths. This method could be very valuable in the field of non-invasive blood flow-sensing, detection of low-lying tumours or other skin abnormalities.

To achieve more reliable normalization of the images from different wavelengths, it is advisable to try additionally on calibrated phantoms with known optical properties. Once the normalization, which is a wavelength-specific process is achieved with known phantoms, this process can be applied to *in vivo* imaging of biological tissues. With selective and limited wavelengths as in our case, it is not possible to access the entire range of depths as suggested in Figure 5.1 and Table 5.2. The chosen spectra does not allow us to probe as deep as expected. It is thus necessary to chose the wavelengths according to their spectra and also wavelengths closer to each other.

To quantify the concentration of chromophores and also isolate the absorption maps of biological tissues at different depths, it is thus essential to have knowledge about the attenuation at a wider range of wavelengths in order to fit the conditions for G and also for

α_s. This can be easily achieved by using a hyper-spectral camera and resorting to Hyper-Spectral Imaging (HSI).

6

EXTENSION OF POLARIZATION GATING TO LASER-SPECKLE CONTRAST IMAGING (LSCI)

USING coherent light with optical methods to extract information from biological tissues revolves around the existence of 'Speckles'. This chapter deals with the definition and the kind of information that can be retrieved from speckles. And it further elaborates on the preliminary experiments that were conducted to combine coherent light and polarization gating techniques. The experiments were first conducted on solid phantoms to verify validation of the method.

6.1 INTRODUCTION

'*Speckle*' is an intensity pattern produced when coherent light hits a slightly rough surface or a scattering volume. With the advent of lasers, the study of this intensity pattern produced by mutual interference of a set of wavelengths became popular for extracting information from the media it hits [Allen and Jones, 1963; Oliver, 1963; Pedersen, 1976; Rigden and Gordon, 1962]. When a coherent light source is incident on biological tissue, it produces a speckle pattern, and if there are scatterers that are moving (as in the case of red blood cells), their movement causes phase shifts in the scattered light and thus changes the random interference pattern. These in-turn produce temporal fluctuations in the speckle pattern that is analogous to the intensity fluctuations that arise from Doppler shifts. The dynamics of the speckle pattern thus contains information about the motion of the scattering particles in the sample. This characteristic made it popular for implementation in various applications.

The use of laser speckles in medical imaging dates back to the 70's where it gained popularity in the assessment of blood flow [Stern et al., 1977] followed by works of Briers and Fercher to study the retinal vasculature [Briers and Fercher, 1982; Fercher and Briers, 1981] (also called Laser Speckle Contrast Analysis (LASCA) and now referred to as Laser Speckle Contrast Imaging (LSCI)). With the availability of faster digital acquisition and processing, LSCI advanced rapidly for imaging blood flow in retina [Sugiyama et al., 2010], skin [Briers et al., 1999; Draijer et al., 2009], brain [Dunn et al., 2001; Yuan et al., 2005]. Speckle contrast techniques concentrate mainly on the statistical analysis of the speckle pattern as first shown by Goodman [1975]. Some of the most important of these methods include: Laser Doppler Flowmetry (LDF), Diffuse Correlation Spectroscopy (DCS) and Laser Speckle Flowmetry (LSF). LDF uses the frequency shift produced by the Doppler effect to measure velocity either for blood flow or tissue movement inside the body [Briers, 2001; Dirnagl et al., 1989]. LSF uses the spatio-temporal blurring of speckles to measure

flow [Ayata et al., 2004; Boas and Dunn, 2010]. DCS uses the light intensity autocorrelation of diffusing light transported through tissue to measure dynamics of the scatterers, and thus flow [Boas et al., 1995; Boas and Yodh, 1997; Durduran et al., 2010]. One of the major differences between these methods is the volume that they probe, i. e. their penetration depth: LDF and LSF mainly deal with single-scattering events and thus usually probe superficial volumes ($< 1mm$), whereas DCS that is based on the photon diffusion theory accesses multiple scattered photons up to several centimetres. LDF methods also have the disadvantage of limited application due to long scanning and image acquisition times. In the field of micro-circulation imaging, in comparison to currently available methods like polarization spectroscopy, Photo Acoustic Tomography (PAT), tissue viability imaging and capillaroscopy, laser speckle-based methods are superior due to their high resolution and possibility of real-time image acquisition [Leahy et al., 2007]. MRI and PET methods can produce 3D spatial information for Cerebral Blood Flow (CBF) mapping, but at the cost of low resolutions, expensive and bulky infrastructures [Dunn et al., 2001]. In general, these methods do not cater to the assessment of the same physical quantities.

Of all the optical technologies available for the analysis of tissue structure and dynamics, coherence-domain and polarimetric methods have proven to be a more simple, robust and fairly economical alternative to non-coherent photon diffusion and ultra-short pulse techniques when applied to rather thin tissues [Bicout et al., 1994; Hielscher et al., 1997; Morgan et al., 1997; Schmitt et al., 1992; Tuchin, 2013; Zimnyakov et al., 1997]. Using these coherent techniques in diffuse optics is seen dominated in methods like DCS and LSF methods, but with focus on probing parameters that are not the same. The statistical properties of laser speckle patterns have been studied extensively over the years, starting from Goodman [1975]'s review on speckle properties, theoretical and experimental verifications on first-order statistics of Stokes parameters [Fercher and Steeger, 1981; Steeger and Fercher, 1982], statistics of normalized Stokes parameters [Brosseau, 1995], statistics of partially polarized light [Barakat, 1985] to micro-statistics of polarization behaviour [Freund et al., 1990; Tarhan and Watson, 1992]. Studies have also been done to get extensive information about the depolarization among speckle patterns [Elies et al., 1997] and more importantly on the DOP of points in a speckle field [Li et al., 2002]. Li et al. concluded in their study of DOP on single and multiple coherence areas, that depolarization of the incident polarization is unavoidable, but that the measured DOP mainly depends on the size of detected area (larger the area, smaller the DOP). However, most of these studies focussed on studying the depolarization of speckles as opposed to finding measures of retaining polarized speckles. Also, Speckle contrast as a unit of measurement has some ambiguity, as it is a relative-statistical quantity which has limited information about the size, density, or depth of the structure that is being studied.

To overcome the drawbacks of the past methods, we would like to propose the use of elliptically polarized light with a coherent light system. As discussed in previous chapters, the use of elliptically polarized light with Polarization Difference Imaging (PDI) has shown substantial results in terms of enhanced contrast and signal and for accessing user-defined depths at given wavelengths. In this chapter, the main focus is on adapting the aforementioned polarization gating techniques with a coherent light system, i. e. laser speckles. The goal of this study is to understand if this added property of 'polarization gating' can help

us throw light on the possible differences in depth and density of scatterers present in the subsurface. And to achieve this, it is imperative to understand the basics of speckles, their statistical properties, both spatial and temporal, and to choose the methods that is most adapted to our desired system.

6.1.1 *Laser Speckle: Basics*

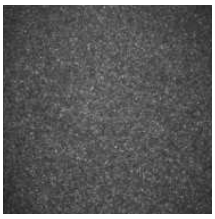

Figure 6.1: Speckle pattern observed when coherent laser light is incident on a rough surface.

When an object is illuminated with coherent light from a laser, a random interference pattern or speckle is produced. This light that is back-scattered and detected at the camera shows a mixture of bright and dark spots (Figure 6.1) which is due to the fact that laser light that reaches each pixel has travelled slightly different path lengths (due to the inhomogeneity of the surface), and adds constructively and destructively. A graphical representation of the speckle types is represented in Figure 6.2.

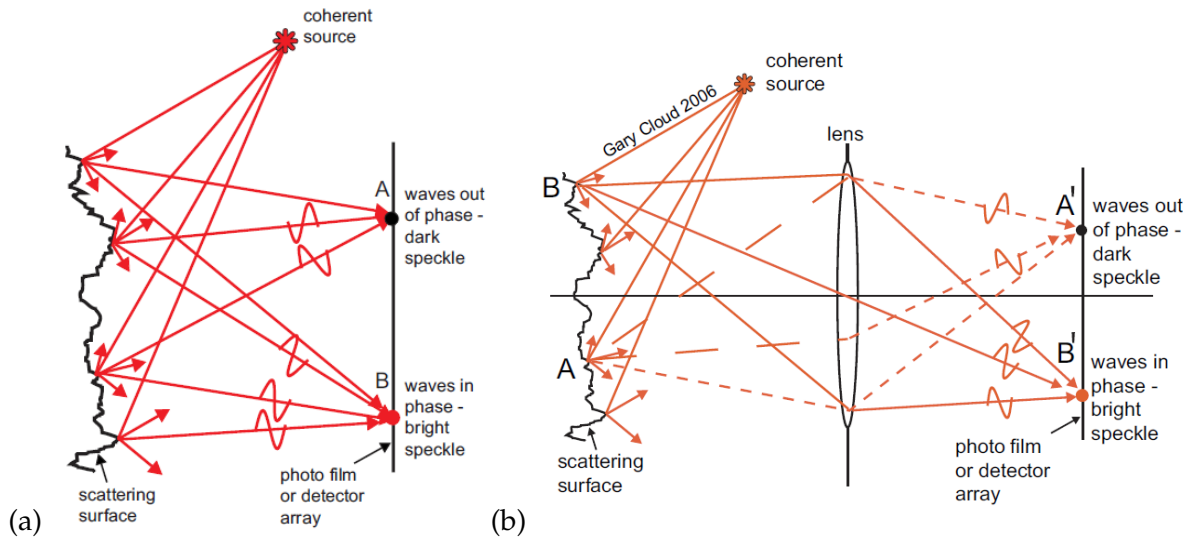

Figure 6.2: Types of speckles with (a) Objective speckle formation, and, (b) Subjective speckle formation [Cloud, 2007].

Based one the formation of the speckle pattern, there are two types of speckles: objective and subjective speckles. Objective coherent speckles are so defined due to the absence of

a lens in the system and they cannot be observed directly. Subjective speckles, however is generated with the use of a lens in the system and affects all the pictures taken with coherent illumination. In our context, objective lenses are used, and therefore only subjective speckles are taken into account. If scattering particles in the medium are moving, their motion causes changes in the interference, which is detected as intensity variations in the image. The movement of the object alters the speckle pattern over time. Laser speckle is a random phenomenon and can only be described statistically [Goodman, 1975]. By quantifying the temporal and spatial statistics of the speckle pattern, we can extract information about the motion or flow of the scattering particles. The extent of the fluctuations can be high and cause blurring of the speckles depending on the exposure time of the camera (i. e. it is longer than the time scale of the intensity fluctuations, ~ 1ms for biological tissues) and choice of detector/s.

Speckle contrast can be measured either spatially or temporally on the measured intensity, I. The speckle contrast (κ) in general, can be defined as the ratio of the standard deviation of measured intensity (σ_I) over different speckles separated in space or time to their mean intensity (μ_I) [Briers and Webster, 1996],

$$\kappa = \frac{\sigma_I}{\mu_I} \tag{6.1}$$

For a polarized speckle pattern, or a fully developed speckle pattern, the speckle contrast is equal to 1, which means that there is no blurring of speckle pattern, and therefore, no motion of scatterers. And if the speckle contrast is 0, it means that the scatterers are moving too fast and thus blur all the speckles.

Just to be familiar with the techniques of calculating speckle contrast, it is important to know the definitions of the important parameters. For speckle contrast from spatial statistics, one of the most important parameter is the speckle size relative to the camera pixel size. And the minimum speckle size for a speckle pattern to be imaged onto a camera is given by [Boas and Dunn, 2010],

$$\rho_{speckle} = 2.44\lambda(1 + M)f/\# \tag{6.2}$$

where λ is the wavelength of light, M is the magnification of the imaging system and $f/\#$ is the F-number of the system (ratio of the lens's focal length to the diameter of the entrance pupil, which gives a quantitative measure of lens speed in an optical system). Kirkpatrick et al. [2008] demonstrated that the Nyquist sampling criteria must be satisfied, which means that the size of speckle must be at least twice the size of the pixel (i. e. $\rho_{speckle} \geqslant 2\rho_{pixel}$), to obtain a fitting speckle intensity distribution. κ is estimated based on the mean and standard deviation of the speckle intensity and is calculated by a square-window of NxN *pixels*. Larger the window, a greater speckle contrast is achieved, but at the expense of spatial resolution. The laser speckle community has chosen a window of 7x7 *pixels* as being an optimal choice which does not hamper the spatial resolution and gives a good estimation of κ, totally dependent on the camera resolution, speckle size and desired contrast resolution [Boas and Dunn, 2010]. On the other hand, temporal speckle contrast involves the process of imaging all the pixels in parallel to measure the temporal fluctuations of speckle, which forms a Fourier transform pair with the intensity temporal

autocorrelation function, $g_2(\tau)$(See Eqn. 6.3). Typically, if temporal samples are statistically independent (i. e. time between samples is greater than the correlation time), lesser number of samples are required for an accurate estimation of the speckle contrast.

Another important concept that plays a key role for quantifying the speckle contrast due to motion of particles inside a medium, is how the motion of particles in the medium affects the phenomenon of light scattering. This can be understood by measuring how a signal at a certain time, t, is related to a signal measured at a time, $t+\tau$, given by the normalized intensity temporal autocorrelation function [Berne and Pecora, 1976],

$$g_2(\tau) = \frac{\langle I(t)I(t+\tau)\rangle}{\langle I(t)^2\rangle}. \tag{6.3}$$

Intensity which is the readily available quantity from measurements is related to the electric field (which contains information about speckle pattern fluctuations, due to random changes in phase) as, $I(t) = |E(t)|^2$. And further, the normalized electric-field autocorrelation function is represented as,

$$g_1(\tau) = \frac{\langle E^*(t)E(t+\tau)\rangle}{\langle E(t)^2\rangle} \tag{6.4}$$

It is useful to express the $g_1(\tau)$ in terms of intensity measured at the detector. Finally, the electric-field auto-correlation function can be extracted from the intensity data using Siegert's relation [Lemieux and Durian, 1999] as,

$$g_2(\tau) = 1 + \beta|g_1(\tau)|^2 \tag{6.5}$$

where β is a constant and correction factor that accounts for the number of speckles detected depending on the experimental conditions.

6.2 POLARIZATION GATING WITH COHERENT LIGHT

Speckle contrast analyses have been done extensively over the years with constant improvements in different dimensions for enhanced spatial and depth resolution. The focus of this chapter is on further retrieving depth information by using laser speckle methods with elliptically polarized light. To combine polarization gating methods discussed in this thesis to laser speckle contrast methods, we have adopted a noise correction regime from Speckle Contrast Optical Spectroscopy (SCOS) techniques from Valdes et al. [2014] to optimize the algorithm.

6.2.1 *Speckle Contrast Calculation*

6.2.1.1 *Raw Speckle Contrast*

The raw intensity images are initially corrected for the dark background before computing the speckle contrast. A mean dark image, $\mu_{(I_D)}$, is obtained by taking the mean of several dark frames, I_D. From each raw intensity image, I, the $\mu_{(I_D)}$ is subtracted to give the dark corrected images denoted as,

$$I_c = I - \mu_{(I_D)} \tag{6.6}$$

The speckle contrast is then defined as the ratio of the standard deviation over different dark-corrected speckles separated in space or time, $\sigma_{(I_c)}$, to their mean, $\mu_{(I_c)}$, i. e.,

$$\kappa = \frac{\sigma_{(I_c)}}{\mu_{(I_c)}} \tag{6.7}$$

Here the dark correction will remove the contribution of the mean dark counts from the $\mu_{(I_c)}$ because $\mu_{(I_c)} = \mu_{(I)} - \mu_{(I_D)}$, and the variance of the mean dark counts is then expressed as,

$$\sigma^2_{(I_c)} = \sigma^2_{(I)} + \sigma^2_{(\mu_{(I_D)})} \ ^\star \tag{6.8}$$

However, subtracting the mean dark image from the raw image does not help remove the noise (variance) associated with the dark image. Hence, a dark variance correction, $\sigma^2_{(d)}$, was performed to remove the dark noise variance from the variance of raw intensity images. This parameter contains different sources of noise including the read-out noise. The mean dark variance, $\sigma^2_{(d)} = \mu(\sigma^2_{(I_D)})$, is the mean of variances computed from several dark frames which are acquired at the same exposure time as we use to obtain the raw intensity images. Another significant noise source is the inherent shot-noise, and the speckle contrast can be corrected to account for this factor as well [Yuan, 2008] and can be represented as,

$$\kappa_c = \sqrt{\frac{\sigma^2_{(I_c)} - \sigma^2_{(s)} - \sigma^2_{(d)}}{\mu^2_{(I_c)}}} \tag{6.9}$$

where $\sigma^2_{(s)}$ is the shot-noise contribution.

The corrected speckle contrast calculation was summarized as developed and described by Valdes et al. [2014] and summarizes the noise correction algorithm that was used in Speckle Contrast Optical Spectroscopy (SCOS). SCOS is a technique similar to LSF that uses the speckle contrast but with a difference in instrumentation. It uses point sources placed at a distance as in DCS, used for detecting photons that have undergone multiple scattering. This facilitates detection of many speckles in parallel but with extended path lengths for deep tissue sampling (mainly for measuring deep tissue blood flow). As their first trials, they calculated the speckle-contrast with shot-noise correction κ_c, for liquid phantom Lipofundin (analogous to Intra-lipid®) and found a fitting particle diffusion co-efficient (D_B) value with the measured DCS autocorrelation curve. They also repeated these measurements for inhomogeneous flows in microfluidic phantom with Lipofundin and also *in vivo* for the measurement of blood flow in forearm, and validated the measurements of changes in flow w.r.t the calculated speckle contrast. To summarize, the speckle contrast ranges from 0 to 1, where the highly stationary particles produce no/less blurring and have higher values ($0.2 < \kappa < 12$) as in the case of solids like tissues. For liquids, or particles moving fast, the speckle contrast is generally found to be lower ($0 < \kappa < 0.2$) as the

⋆ **Property**
Variance of two random variables where one is subtracted from the other is additive (associative), i.e. $Var[X - Y] = Var[X] + Var[Y]$

scatterers are moving fast enough to blur all the speckles. So with these distinct values of speckle contrast, it is possible to differentiate between the structure/volume we are looking at.

6.2.1.2 *Polarized Speckle Contrast*

To equate this speckle contrast calculation to the use of images with different incident polarization configurations (see channels C1-C4 in Table 3.1), we will first try a simple PDI method with Elliptical Polarization Difference Imaging (EPDI). The cross-linear intensity images C2 are subtracted from each angle of co-elliptical intensity images C3 in order to get an idea of the depth probed with each elliptic angle ($0° - 45°$ in steps of $10°$, i.e. 5 different angles, and therefore 5 sets of raw intensity images). In the case of polarization gating with EPDI, it is not necessary to correct for the dark background, as this is already achieved with gating. Even with dark correction, the contribution from the mean dark counts is really low and can be neglected. This excludes a whole portion of computing the dark mean counts and simplifies background subtraction.

The Polarization gated speckle contrast (κ_P) is then defined as the ratio of the standard deviation of EPDI, $\sigma_{(EPDI)}$, to its mean, $\mu_{(EPDI)}$,i.e.

$$\kappa_P = \frac{\sigma_{(EPDI)}}{\mu_{(EPDI)}} \tag{6.10}$$

where EPDI represents the polarization maintaining photons (intensity) after having subtracted the cross-linear intensity from the co-elliptical intensity, i.e.

$$EPDI = C3 - C2 \tag{6.11}$$

Now taking the variance of Eqn. 6.11, we get

$$\sigma^2_{(EPDI)} = \sigma^2_{(C3)} + \sigma^2_{(C2)} - 2.Cov[C3,\ C2]^\star \tag{6.12}$$

And thus, Speckle contrast with polarization gating (EPDI) is given by,

$$\kappa_P = \sqrt{\frac{\sigma^2_{(C3)} + \sigma^2_{(C2)} - 2.Cov[C3c,\ C2c]}{(\mu_{(C3)} - \mu_{(C2)})^2}} \tag{6.13}$$

⋆ **Property**
Variance of two random variables where one is subtracted from the other is expressed as the sum of their individual variances and the difference of twice their covariance, i.e.
$Var[X - Y] = Var[X] + Var[Y] - 2.Cov[X, Y]$
Covariance is a measure of how much two random variables change together. If the greater values of one variable mainly correspond with the greater values of the other variable, and the same holds for the smaller values, i.e., the variables tend to show similar behaviour, the covariance is positive. In the opposite case, when the greater values of one variable mainly correspond to the smaller values of the other, i.e., the variables tend to show opposite behaviour, the covariance is negative.

To add shot-noise corrections to the speckle contrast, we can rewrite the Noise-corrected polarization gated speckle contrast (κ_{PC}), as,

$$\kappa_{PC} = \sqrt{\frac{\sigma^2_{(C3)} + \sigma^2_{(C2)} - 2.\mathrm{Cov}[C3c,\ C2c] - \sigma^2_{(s)}}{(\mu_{(C3)} - \mu_{(C2)})^2}} \tag{6.14}$$

In our context, it is important to understand how κ relates to polarization gating with different channels and what values/information is expected. To recapitulate, it was shown that with increasing ellipticities, the polarization-maintaining photons travel deeper and that polarization gating (with PDI) helps remove all background and depolarized photons. For example, in case of blood vessels, if one vessel shows a lower speckle contrast than another vessel, this could be because the vessel is deeper (causing fewer photons to reach the vessel, decorrelate, and return to the surface), or because the amount of suspended particles in the vessel is lower (also causing lower photon numbers to scatter from the vessel). In other words, there is limited information on the size, density, or depth of the buried vessel due to this ambiguity. This is where polarization gating will help us in quantifying this depth information and correlating this to the value of speckle contrast. With measuring the trend of speckle contrast values for each ellipticity, it is possible to have an idea about depth-related information.

6.3 EXPERIMENTAL SET-UP AND CALIBRATION

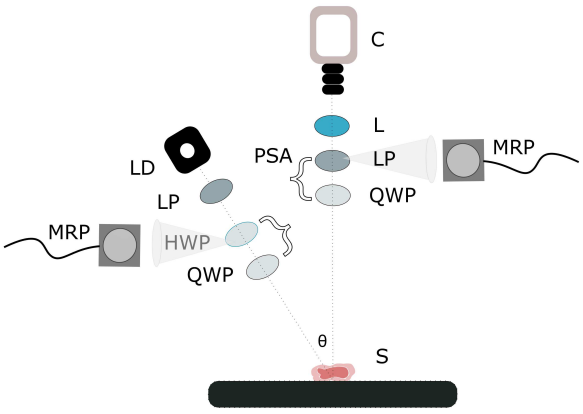

Figure 6.3: Schematic of the experimental set-up with coherent light where, LD: laser diode, LP: linear polarizer, HWP: half-wave plate, QWP: quarter-wave plate, θ: angle of incidence, PSA: polarization state analyzer composed of a quarter-wave plate (QWP) and analyzer, L: magnification lens, C: CMOS camera with objective, MRP: motorized rotation plate.

The set-up as seen in Figure 6.3 is composed of a laser diode (HL63133DG, 170mW at 637nm, Thorlabs®, Germany) as source, half-wave plate (1", achromatic wave plate for wavelength range 400-800nm Thorlabs®, Germany) and a quarter-wave plate (1", achro-

matic zero-order wave plate for wavelength range 500-700nm with a $\pi/2$ de-phasing at 633nm, SPD - Samoylov A.V., Ukraine) on the illumination path. The laser diode is linearly polarized at 0° to the plane of incidence. Moreover, the polarizer guarantees that the incident beam is linearly polarized. The half-wave plate is used to flip this transmission axis of the laser diode, and the fast-axis of the quarter-wave plate is then used to generate different states of polarization (linear, vertical, elliptical or circular). The incident beam after hitting the sample, is then detected through a Polarization State Analyzer (PSA) composed of a quarter-wave plate (2", achromatic zero-order wave plate for wavelength range 500-700nm with a $\pi/2$ de-phasing at 633nm, SPD - Samoylov A.V., Ukraine) and an analyzer (1", dichroic, extinction ratio 10000:1, LPVISB100, Thorlabs®, Germany), to return the state of polarization. The relative rotation angle between polarizers and quarter-wave plates is tuned such as to obtain the desired polarization modes for illumination and detection (Figure 3.5 and Table. 3.1). The reflected beam then passes through a magnification lens (AC508-400 A-ML, Thorlabs®, Germany) and is detected by a CMOS camera (Orca Flash 4.0, Hamamatsu Photonics, Japan) with an objective (7000E, Laser Components SAS, France).

The system was calibrated for the polarization optics as described in Section 3.2.2 with the exception of the half-wave plate which was only used to set the transmission axis of the laser to a desired orientation. For precision of tuning the angles, motorized rotation plates were used to move the half-wave plate and linear polarizer in the detection path. The required speckle size, $\rho_{speckle}$, was calculated as described in 6.2, and to achieve the optimum $\rho_{speckle}$ of 21µm, the f/# was set to a value of 11 on the objective. Before image acquisition, the homogeneity of the incident coherent beam was verified in both x− and y−axes to check for the formation of speckles w.r.t the exposure time. About 50 images were taken per angle of ellipticity in order to account for statistics. The exposure times were varied from 1.5ms to 5ms depending on the sample used. Once all the channels were imaged, the laser diode was covered with a lid in order to take dark images, accounting for background noise. The speckle contrast of the images were then calculated based on the methods described in 6.2.1.

6.4 RESULTS

After calibration, preliminary experiments were conducted on liquid and solid/gel phantoms to measure the speckle contrast at different polarization configurations. Speckle contrast was calculated with and without polarization gating, i. e. κ and κ_P and compared for each case. In case of liquid phantoms, about 250ml of the Intra-lipid® (at desired concentration) was poured into a transparent container for imaging. In case of solid phantoms, the solid was moulded into the same transparent container with a total volume of ~ 250ml. To recapitulate the Reduced scattering coefficient (μ_s') and the respective dilutions used for manufacturing liquid and solid/gel phantoms with Agar and Intra-lipid®, the data is represented in Table 6.1. The Absorption coefficient (μ_a) was considered negligible and the Anisotropy factor (g) of Intra-lipid® was taken from literature as $g = 0.73$ [van Staveren et al., 1991].

Table 6.1: Concentrations of Agar and Intra-lipid® and their respective Reduced scattering coefficient (μ_s') for the preparation of solid and liquid phantoms.

	Concentration (%)	μ_s' (cm^{-1})
Liquid		
	0.1% Intra-lipid®	~ 1
	1.0% Intra-lipid®	~ 10
Solid/Gel		
	1% Agar - 0.1% Intra-lipid®	~ 1
	1% Agar - 1.0% Intra-lipid®	~ 10

The phantoms for different concentrations are represented in Figure 6.4 for (a) Intra-lipid®, (b) Agar - Intra-lipid® phantoms of (a) 0.1% and (b) 1% respectively. The respective horizontal cross-plots are seen in Panels (c) for 0.1% and (d) for 1% concentrations respectively. The cross-plots indicate a similitude in intensity over the phantoms (horizontally) validating their homogeneity. Visual inspection and also further quantification suggest that the phantoms are optically matched quite well, despite being in two different states, liquid and solid.

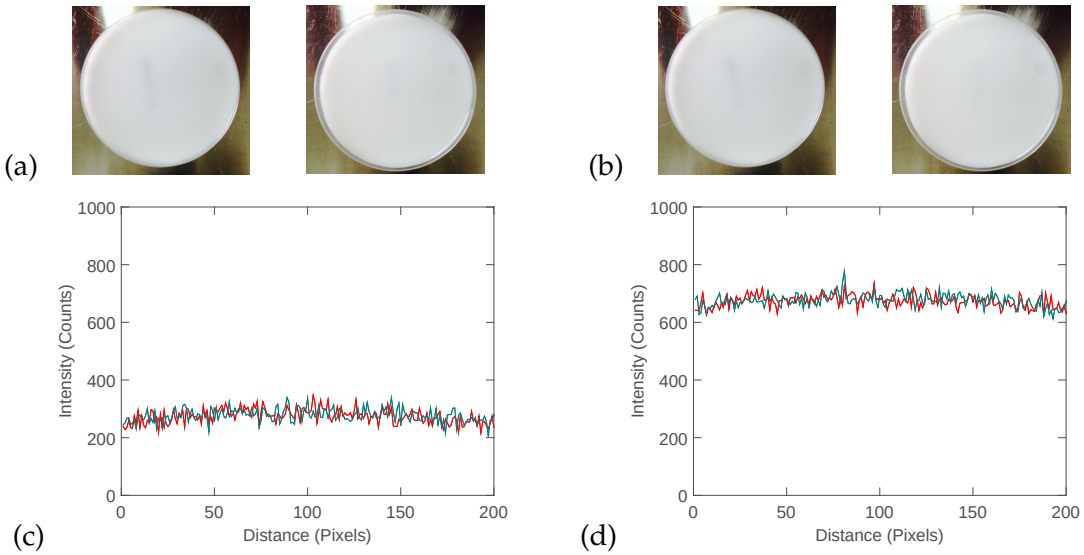

Figure 6.4: Images of Intra-lipid® (liquid) and Agar and Intra-lipid® (solid) phantoms for concentrations (a) 0.1% ($\mu_s' = 1cm^{-1}$), and, (b) 1% ($\mu_s' = 10cm^{-1}$) along with their horixontal cross-plots (c) and (d) respectively. Plot line 'red' represents Intra-lipid® (liquid) and 'blue' represents Agar and Intra-lipid® (solid) phantom respectively.

Figure 6.5 shows the mean speckle contrast (taken over the whole phantom with homogeneous surface) determined for a liquid phantom (0.1% Intra-lipid®, Figure 6.5a) and for a solid phantom (1% Agar and 0.1% Intra-lipid®, Figure 6.5b). The optical properties of the two phantoms were matched by using the correct dilutions for Agar and Intra-lipid®. For preliminary measurements, the speckle contrast was just calculated as in Equation 6.7

and no other noise correction was made.

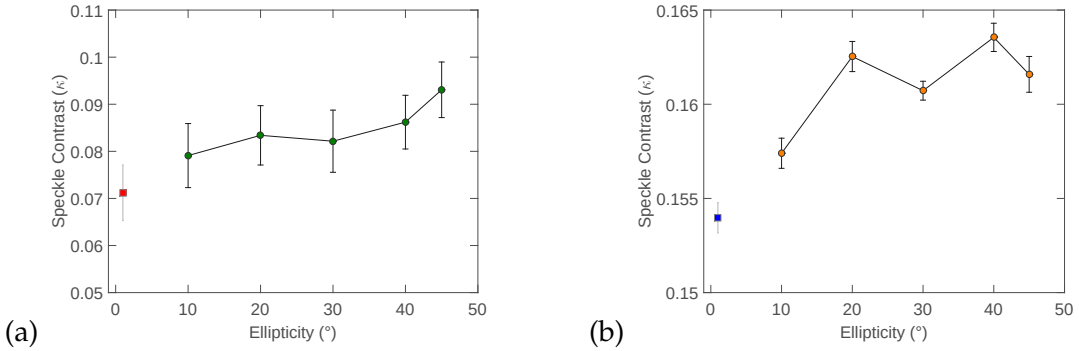

Figure 6.5: Speckle contrast, κ, at different polarization channels for (a) 0.1% Intra-lipid®, (b) 1% Agar - 0.1% Intra-lipid® phantoms. Squares represent the Cross-linear channel (C2). Circles represent the C3, from 10°-45°. Standard deviation bars are also shown. Image exposure time, 3ms.

Comparing Figures 6.5a and 6.5b, the ranges of κ conform to the fact that liquids have a lower speckle contrast as compared to solids or gels (see Section 6.2). In both phantoms, channel C2 appears to have lower values as compared to channel C3. Channel C3 at different ellipticities shows a slight increase with increase in ellipticity. Thus, for homogeneous media, the speckle contrast behaviour with different polarization configurations was found to increase slightly with increase in ellipticity. We also need to keep in mind that this corresponds only to the raw speckle contrast at different ellipticities. Only background noise has been removed but no background subtraction has been performed to eliminate depolarized/specular components.

To verify the depth that can be probed with polarized speckles, it was essential to design a phantom with layers consisting of both solid and liquid components which allowed for the clear distinction of speckle contrast values. For this purpose, we designed two models of phantoms using both, a solid/gel phantom and a liquid phantom. The solid/gel phantom was composed of Agar and Intra-lipid® with desired concentration (for desired optical properties, μ_a and μ_s') and fabricated using the technique described in Section 3.3.2. The liquid phantom was a solution of Intra-lipid® diluted to match the properties of the solid phantom. The two models of phantoms and their respective speckle contrasts are described shortly.

Homogeneous Two-layer phantom

The first type of layered phantom was a two-layer homogeneous model, with gel/solid as the bottom layer and liquid as top layer. A schematic of the sample can be seen in Figure 6.6 with the dimensions of the phantom. Layers of the liquid were added on top of the gel layer in increasing heights of 0.5mm and the speckle contrast was measured at each of these heights of the liquid (corresponding to different depths of liquid on the gel layer)

and also at different ellipticities.

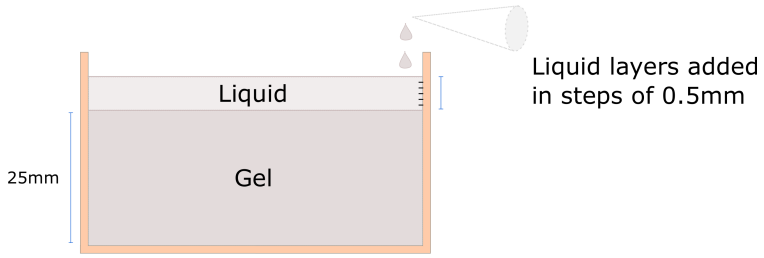

Figure 6.6: Schematic of a two-layered homogeneous phantom made with Agar-Intra-lipid® gel (bottom layer) and Intra-lipid® (bottom layer). The liquid layer is added in steps of $0.5mm$ for measurement at different heights of the liquid on the gel.

As a first sample, we prepared the gel and liquid to have a μ_s' of $1cm^{-1}$ (see Table 6.1 for concentrations). The speckle contrast calculated at different heights of the liquid on the gel can be seen in Figure 6.7. The blue square in the figure represents the raw speckle contrast calculated for Intra-lipid® with a height identical to the solid phantom (25mm). Circles represent the speckle contrast measured starting at just the gel (i. e. $0mm$ of liquid) to a height of $3mm$ of liquid added on the gel. The trend of speckle contrast shows a decrease with increase in the height of liquid. After a depth of $1.5mm$, the speckle contrasts measured is equal to that measured for only liquid (blue square on Figure 6.7) suggesting that the speckles are not hitting the solid surface any longer. The further drop in speckle contrast can only suggest that the decrease in κ is due to the movement of speckles and/or due to sedimentation of particles in the liquid. The values of κ between heights 0 and $1.5mm$ show intermediate values from being solid to liquid suggesting that the speckles are due to different depths of the liquid. The next step would be to compare the speckle contrast versus depth curves for different ellipticities and polarization gating to observe the trend of speckle contrast values w.r.t depth probed.

Figure 6.8 shows the Polarization gated speckle contrast (κ_P) measured for different ellipticities and at different heights of liquid layer added. The curves for all ellipticities suggest a drop in speckle contrast value with addition of $0.5mm$ layer of Intra-lipid® solution. This value then appears to be constant at the following depths from $1-3mm$. This could be due to the fact that at steps of $0.5mm$, the actual depth probed is a smaller volume (in the order of microns evaluated with the optical properties of Intra-lipid®) and since we are looking at a deeper quantity, the depth-sensitivity of the different ellipticities is not accurate. After a depth of $0.5mm$ of Intra-lipid® layer, the κ_P shows values that classify as of liquids and suggest the evidence of strong depolarization. To further study this purpose, we constructed a two-layer wedged phantom that will allow us to differentiate a gradient of depths more easily.

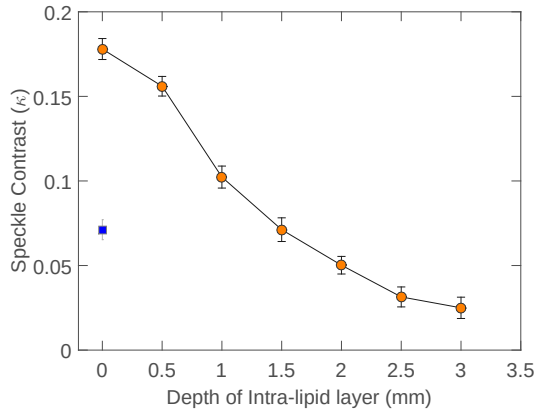

Figure 6.7: Speckle contrast, κ, at different depths of liquid Intra-lipid® layers for the homogeneous two-layer phantom with gel and liquid. Squares represent liquid Intra-lipid® at same sample height as just the solid gel as seen in Figure 6.6. Circles represent speckle contrast of sample taken with addition of different amounts of liquid Intra-lipid® in steps of 0.5mm. Image exposure time, 3ms.

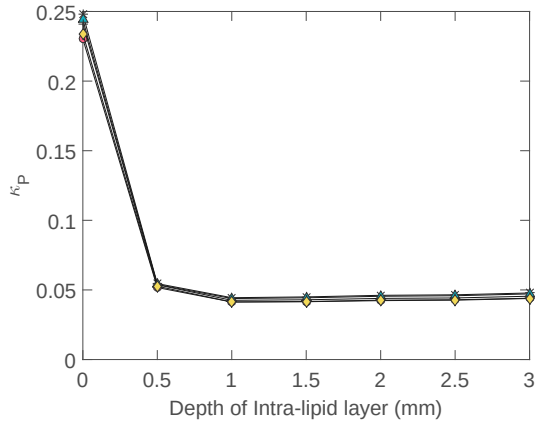

Figure 6.8: Polarization gated speckle contrast (κ_P) at different ellipticities and different depths for the homogeneous two-layer phantom with gel and liquid. The ellipticities are represented as circles (10°), asterisks (20°), triangles (30°), plus signs (40°) and diamonds (45°) respectively. Image exposure time, 3ms.

Two-layer wedge phantom

The second phantom was a wedge-like phantom consisting of a solid phantom on the top layer which inclined till the bottom, to have different depths at a gradient as shown in Figure 6.9. The lower layer was filled with liquid and then the phantom was imaged from the top.

A 400x400 pixels image was taken at each channel and later analyzed at a smaller ROI of 320x50 pixels (yellow rectangle indicated in Figure 6.9c and in Figure 6.10a). The phantoms were first imaged with water added in the cavity as a reference to the measurements with liquid Intra-lipid®, and later imaged with 0.1% Intra-lipid®. Figure 6.10 shows the raw intensity image (Panel (a)) of the wedge phantom along with the ROI for speckle contrast calculation and is highlighted. This ROI was chosen where the phantom was most

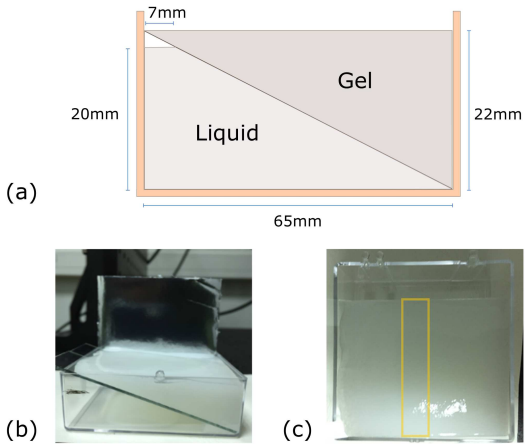

Figure 6.9: (a) Schematic of the wedged phantom made with Schematic of the wedged phantom made with 1% Agar-0.1% Intra-lipid® along with its dimensions, (b) Side-view image of the wedged phantom and (c) Top-view image of the wedged phantom. The yellow rectangle in Panel (c) represents the ROI analysed for speckle contrast. It represents a gradient of depths up to 20mm.

homogeneous in structure and also received homogeneous illumination in horizontal as well as vertical axes. Panel (b) and (c) show the speckle contrast images of the ROI when images with water and Intra-lipid® respectively. Panel (b) shows that κ is quite uniform throughout the image (but changing in intensity) with speckles distributed evenly. This confirms the absence of scatterers in water, and that the speckle contrast arises only from the solid gel surface which is uniform. On the contrary, κ in Panel (c) is seen to have a gradient (from top to bottom). This can be explained by the fact that light reaches the liquid Intra-lipid® (with scatterers) at lower depths of the gel and as the height of the gel increases, the speckle contrast increases. There are more speckles where the light hits only the gel layer, and vice versa for the liquid layers. Thus to quantify the speckle contrast as a function of depth of the gel/liquid interface, the vertical section of the ROI was divided into slices of 10x50 pixels, and each layer represented a depth of 1.42mm. The mean speckle contrast was calculated at each slice and for each ellipticity, and represented as a function of depth and can be seen in Figures 6.11 and 6.12 for water and Intra-lipid® respectively.

The curves represented in Figure 6.11 show channels C2 and C3 (ellipticities 10°-45°) at different positions on the phantom that corresponds to different depths of the gel. The range of speckle contrast belongs to that of solid phantoms, and thus shows that with water underneath the solid layer, the speckle collected at the detector were stemming from the solid layer only. The curves from different channels do not show any relation to one another, but show a similar random behaviour (with very small changes in speckle contrast value) which can be neglected, meaning that they are all stemming from the same homogeneous solid layer. At depths of 0 - 3cm, there are some fluctuations in speckle contrast which may have been due to some surface roughness during the manufacture of the phantom.

After replacing water with 0.1% Intra-lipid® in the cavity, the same experiment was repeated, and imaged at different channels. Figure 6.12 shows the speckle contrasts at dif-

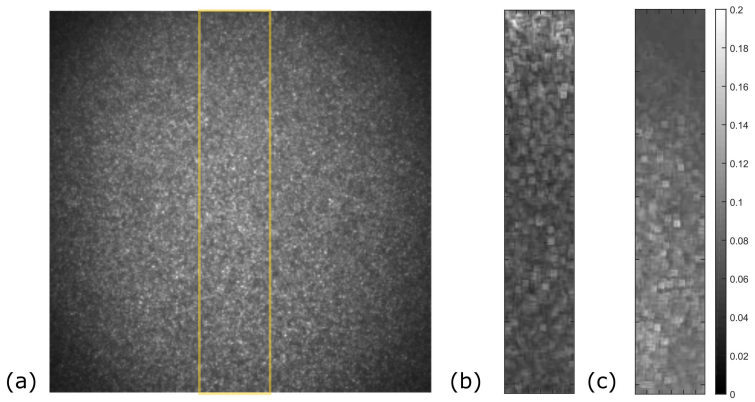

Figure 6.10: (a) Raw intensity image of the wedge phantom, imaged from the top. Image size, 400x400 pixels. Yellow rectangle represents the ROI of 320x50 pixels used to calculate the speckle contrast, (b) Speckle contrast image of the wedged phantom when filled with water, and, (c) Speckle contrast image of the wedged phantom when filled with Intralipid®. Panels (b) and (c) have a common colorbar represented at the right corner of the figure. Image exposure time, 3ms.

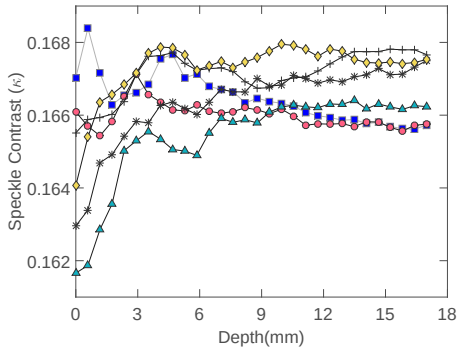

Figure 6.11: Speckle contrast, κ, at different channels for a two-layer wedged phantom with gel and water, representing different depths. Squares represent channel C2. Channels C3 is represented as circles (10°), asterisks (20°), triangles (30°), plus signs(40°) and diamonds (45°) respectively. Image exposure time, 3ms.

ferent channels and positions representing different depths. The curves show a gradual increase in speckle contrast with increase in depth of the gel phantom. The curves from different ellipticities seem to show similar order of magnitude and seem to have the same general behaviour. We observed that the absolute value of the spatial speckle contrast is different for the various polarization channels, and also that within each channel, the speckle contrast is sensitive to the particular depth of the liquid layer. At the very least, this shows that the influence of polarization channels on the photon paths is sufficient enough to be observed in the speckle contrast, and that there is potential for depth characterization by selecting various channels.

To further explore the effects of polarization gating with speckles, we calculated the κ_P for the wedged-phantom at different concentrations as described in Section 6.2 (based on Elliptical Polarization Difference Imaging (EPDI)) and using Eqn. 6.13. Graphical rep-

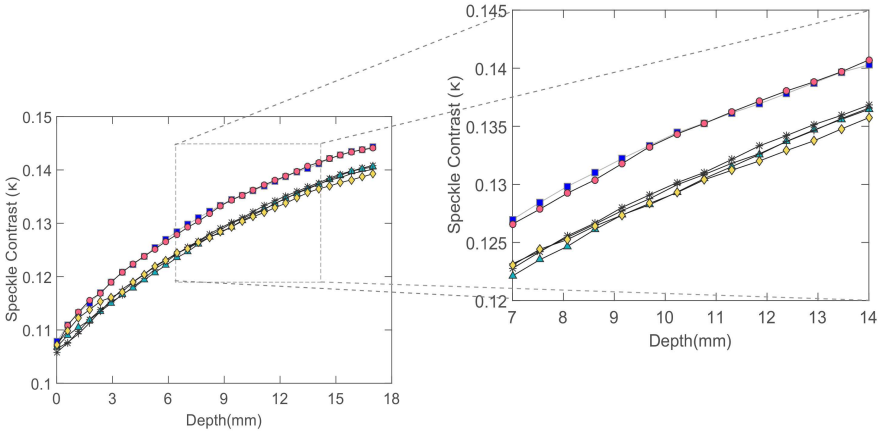

Figure 6.12: Speckle contrast, κ, at different channels for a two-layer wedged phantom with gel and Intra-lipid®, representing different depths. Squares represent channel C2. Channels C3 is represented as circles (10°), asterisks (20°), triangles (30°), plus signs(40°) and diamonds (45°) respectively. Image exposure time, 3ms.

resentation of κ_P versus the depths of the wedged solid taken for samples with reduced scattering coefficients of 1 and $10cm^{-1}$ can be seen in Figure 6.13.

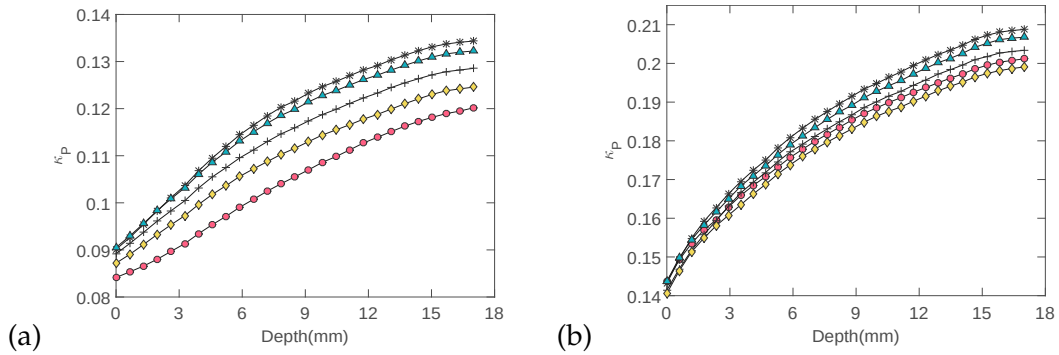

Figure 6.13: Polarization gated speckle contrast (κ_P) at different ellipticities and different depths for a two-layer wedged phantom with concentrations, (a) 1% Agar - 0.1% Intra-lipid® ($\mu_s' = 1cm^{-1}$), and, (b) 1% Agar - 1% Intra-lipid® ($\mu_s' = 10cm^{-1}$). The ellipticities are represented as circles (10°), asterisks (20°), triangles (30°), plus signs (40°) and diamonds (45°) respectively. Image exposure time, 3ms.

Both concentrations of the phantom show similar behaviour with slight differences in their slope. The range of values for κ_P for phantom (a) is lower than that of phantom (b) indicating that higher the concentration of gel (i. e. less transparent) higher is the calculated speckle contrast for a given depth or ellipticity. Comparing the curves for each ellipticity, it can be concluded that there is an increase in the speckle contrast with increasing ellipticity, indicating behaviour similar to that seen in polarization gating with incoherent light (e.g. both in EPDI and MPDI).

From these preliminary tests, it is evident that adding polarization gating to the statistics of speckles provides substantial information about the depths it affects and is also related

to the ellipticity of polarization used. Secondly, we must carefully consider the mechanism by which the speckle contrast changes, and how this relates to the photon paths, and the changes in the polarization state/ellipticity. Understanding this will potentially allow us to resolve the depth and density information that we are interested in.

6.5 SUMMARY

Speckle-based methods are really popular for the study of blood flow and related problems. Due to the ambiguity of the information contained in the measurement of speckle contrast, and the need for more information on depth and density of the scattering medium, we have employed the use of polarization gating based imaging. The preliminary tests of adding this polarization variable, showed that the absolute speckle contrast varied for every polarization channel and the depth in question. We also found evidence that the polarization channels influence the photon paths and change the value of speckle contrast accordingly. These findings indicate that there is definitely information about depth and the possibility of depth characterization becomes evident.

One of the main concerns regarding this method is the evident loss of polarization while probing from one medium to another. In other words, for layered samples, one cannot recover polarized speckles that depolarize based on the medium they are in. While probing in depth from a gel/solid to a liquid, it is possible to still track the speckle contrast (which drops drastically when it hits a liquid layer). But in the opposite case, when we probe from liquid to gel, it is not yet possible to recover the polarized speckles as there is significant depolarization inside the liquid caused by moving scatterers.

Further work is being done on layered phantoms using different scatterers, phantom thickness and lower exposure times. The next steps also include calculation of temporal speckle contrast with the possibility of using more detectors for simultaneous measurement of different polarization channels. Temporal speckle contrast can improve the visibility of deep blood vessels and is less susceptible to static speckle artefacts when compared with the spatial algorithm and can be an interesting point of comparison.

7

DISCUSSION & CONCLUSIONS

This thesis focusses on using polarization-based methods, specifically elliptically polarized light as a means of accessing information from highly diffuse media like biological tissues. The work performed in course of this thesis differs from past investigations due to two significant reasons: it mainly uses the concept of retaining polarization-maintaining photons as opposed to finding the apparent Degree of Polarization (DOP), and it employs the use of elliptically polarized light and not the conventional use of linear polarization gating. The measurement of polarization-maintaining photons after removal of depolarized, multiply-scattered and specularly reflected photons, helps lead the way in accessing deeper structures with the photons that have travelled different path-lengths. Circularly polarized light, or more generally elliptically polarized light has the added advantage of retaining their polarization for longer number of scattering events in comparison to linearly polarized light as explained by the 'polarization memory effect'. This property of elliptically polarized was exploited and incorporated in polarization gating methods to cater to different applications.

As discussed before, polarization gating is a term used for extracting information from samples by using and manipulating the polarization property of light. In our context, we developed an image subtraction mechanism that used different polarization channels (co- and cross-linear; co- and counter-elliptical) to isolate polarization-maintaining photons and eliminate the background (depolarized, unpolarized and specular photons). This method, called Multi-Polarization Difference Imaging (MPDI) was found to be superior to it's contemporaries, Linear Polarization Difference Imaging (LPDI) and Elliptical Polarization Difference Imaging (EPDI) in terms of the measured signal, contrast and resolution of images. LPDI helps access only surface information and with EPDI it is possible to access photons that have travelled deeper by using light with different elliptical polarizations (or otherwise known as ellipticities). But the latter is a simplified form of gating that oversubtracts specular reflections from linear and elliptical polarizations. In this sense, MPDI provides the whole package by providing accurate removal of specularly reflected photons as well as multiply-scattered ones and accessing photons that have travelled deeper (to quantify probed-depth). In addition, this novel method converges with the fact that there is a substantial relationship between the depth/volume probed and the ellipticity of polarized illumination. During the course of this thesis, I have contributed in the construction, automation, calibration and validation of the experimental set-up used for polarization gating with MPDI. In this manuscript we have also summarized the feasibility of depth examination by tuning the state of polarization in four imaging channels, and compare two systems of image subtraction with experiments on calibrated Intra-lipid® phantoms, *ex vivo*, and *in vivo* tissues. With the measurements on Intra-lipid® phantoms, a maximum depth of 7mm could be probed using higher ellipticities of polarization. This translated to the possibility of probing biological tissues to a depth of 0.7mm (since the optical properties of Intra-lipid® phantoms was scaled by a factor of 10 as compared to biological

tissues). *Ex vivo* experiments on chicken neck and *in vivo* human skin experiments conform with the above conclusions, and show higher signal intensity and higher contrast of some structures with elliptic channels (from 0° to 45°) probing subsurface structures. In terms of image processing, important milestones were achieved for movement correction in *in vivo* images. With *in vivo* measurements, the appearance of movements (of the order of a few pixels) in images from one channel to the other are inevitable. This adds constraints in performing $pixel-to-pixel$ subtraction with any of the polarization gating methods (LPDI, EPDI or MPDI). With the developed MATLAB algorithm, precision of ± 1 pixel was achieved and can certainly be improved for an enhances SNR with sophisticated programs of image registration.

In the context of probing deeper volumes, it was evident that with using the counter-elliptical channel (C4) structures in deeper volumes were more 'visible' as compared to the cross-linear (C2). C4, which removes signals coming from superficial layers was found to have more information about depth than the conventionally used C2 [Morgan and Ridgway, 2000; Morgan and Stockford, 2003; Stockford et al., 2002] which gives an apparent measure of the 'deepest probe-able volume'. It would be quite interesting to follow on this lead for clinical uses of accessing deep structures. Another prime development was the concept of linking the wavelength of illumination, ellipticity of polarized illumination as a function of the probed-depth based on the works of Rehn et al. [2013], Zonios and Dimou [2006] and Mesradi et al. [2013] (for rat brain tissue). This feature not only helps one access user-defined depths in biological tissue, but also creates a stepping stone for performing depth-resolved spectroscopy with polarization gating.

Chapter 5 revolved around accessing intrinsic information of tissues by using the Modified Beer-Lambert's Law (MBLL) and polarization gating with MPDI. As a beginning to polarized spectroscopy that can be depth-sensitive, we measured the Ratio of concentrations of two chromophores (R) on two samples, *in vivo* images of a burn scar on human skin and exposed cortex of an anaesthetized rat. A more general form of estimating the R as described by Stockford et al. [2007] was adopted to measure the chromophores in blood, Oxyhaemoglobin (HbO_2) and Deoxyhaemoglobin (Hb) (for rat brain cortex). The study was based on the fact that the Constant offset in attenuation (G) (due to scattering) and Alpha factor for spectroscopy (α_s) are constant values independent of the wavelengths used. But when verified with polarization gating, this was found to be untrue. The theory that G and α_s correspond to the same path lengths was disregarded with our gating system. The images in some wavelengths were found to be more scattering than expected and did not help fit the data to get measurable concentrations of chromophores. To help study the problem in detail, it is advisable to carry out experiments with more controlled factors like external illumination, concentration and spectra of the chromophores and ensure that the source of inconsistencies or errors can be detected from the scratch. The next steps would include to theoretically and empirically test the method with a well-known solution of chromophores with different concentrations in a certain scattering medium which mimics tissue behaviour and the use of polarization gated light which helps selecting and choosing the depth of penetration. With selective and limited wavelengths as in our case, it is not possible to access the entire range of depths as suggested in Section 5.3 (Figure 5.1 and Table 5.2). The chosen spectra does not allow us to probe as deep as expected and

thus necessary to chose the wavelengths according to their spectra and also a closer wavelength range. Although the field of spectroscopy has a long history, very little work has been done on polarized spectroscopy in the wide field, especially one that provides depth information at user-defined volumes. Recently it was shown that Elliptical Polarized Reflectance Spectroscopy (EPRS) was capable of detecting different spectroscopic signatures in multi-layer tissue mimicking phantoms and *in situ* biological tissues [Bailey and Sokolov, 2016]. EPRS showed the possibility of probing target depths for samples with known optical properties, but did not give valuable information in terms of quantifying the tissue chromophores so far. To enable this quantification of the concentration of chromophores and also isolate the absorption maps of biological tissues at different depths, is definitely an important task at hand for improving precision in disease detection, monitoring and image guided surgeries. One method of achieving this is by employing Hyper-Spectral Imaging (HSI). In recent studies, HSI techniques have proven very valuable to the assessment of tissue oxygenation [Calin et al., 2014; Lu and Fei, 2014; McCormack et al., 2014] by providing a non-invasive method of mapping the distribution of HbO_2 and Hb.

An additional application I explored with polarization gating included the use of coherent illumination, which meant the utilization of speckles to gather information from desired media. Recently, coherence-domain and polarimetric methods using speckle theory are quite popular for studying photon-diffusion based applications in biological tissues. The concept of polarized laser-speckles has not been entirely unknown. Li et al. [2002] investigated the behaviour of Degree of Polarization (DOP) for both linear and circular polarization in laser speckles for turbid media. Although it gives a start to the understanding of polarization phenomena in turbid media like biological tissue, there is little information known about the polarized speckles itself and its quantification. The results presented were naive and not convincing of the actual signal coming from the polarized speckle. On the other hand, for the study of blood-flow and related diseases, speckle-based methods have gained popularity. They use a statistically measurable quantity called the Speckle contrast (κ) which correlates the motion of the scatterers (usually red-blood cells in the case of blood), thus giving information on the blood flow. This variable κ is an ambiguous quantity and does not give sufficient information on the size, density, and/or depth of the structure under study. For this reason, we have focussed on adding the concept of polarization gating to the speckle contrast to extract depth information from the samples. We have adopted the results from Valdes et al. [2014] and modified it to facilitate polarization gating via Elliptical Polarization Difference Imaging (EPDI). To validate the method, we performed preliminary tests on layered phantoms with both solid and liquid layers and calculated the Speckle contrast (κ) as well as the derived Polarization gated speckle contrast (κ_P). In summary, the tests suggested that the absolute speckle contrast varied as a function of polarization channel and the depth in question. This meant that the speckle contrast was sensitive to the inherent polarization and in turn to the photon paths. This elucidates the fact that it is possible to extract depth information and in turn have an idea of the density of the volume (solid/gel or liquid etc). Although it gives us an idea of the depths that we can probe, there is a loss of polarization while probing in different media, especially in liquids. The loss of polarization becomes evident when probing from liquid layer to the solid (as seen in Section), as the speckles are lost mainly due to motion of scatterers. These problems can be overcome by using layered phantoms with different scat-

terers (with known optical properties), phantom thickness and adaptive exposure times. With advancements this method can be applied *in vivo* and can provide valuable information in the field of blood-flow sensing in the retina, skin, and the brain.

And thus, in this thesis, an overview of the possible applications and developments of polarization gating imaging using elliptically polarized light has been presented. With immediate applications in various biomedical imaging fields, polarization gating based methods are being sought after. They facilitate the possibility of having ideal diagnostic systems which are non-invasive, low-cost and mostly flexible and portable.

BIBLIOGRAPHY

[Allen and Jones 1963] Allen, L. ; Jones, D. G. C.: An analysis of the granularity of scattered optical maser light. In: *Physics Letters* 7 (1963), Nr. 5, p. 321 – 323. – URL http://dx.doi.org/10.1016/0031-9163(63)90054-4

[Ambrose and Hounsfield 1973] Ambrose, J. ; Hounsfield, G.: Computerized transverse axial tomography. In: *The British Journal of Radiology* 46 (1973), Nr. 542, p. 148–149

[Anastasiadou et al. 2008] Anastasiadou, M. ; Martino, A. D. ; Clement, D. ; Liége, F. ; Laude-Boulesteix, B. ; Quang, N. ; Dreyfuss, J. ; Huynh, B. ; Nazac, A. ; Schwartz, L. ; Cohen, H.: Polarimetric imaging for the diagnosis of cervical cancer. In: *Pysica Satus Solidi (C)* 5 (2008), Nr. 5, p. 1423–1426. – URL http://dx.doi.org/10.1002/pssc.200777805

[Anderson 1991] Anderson, R. R.: Polarized-light examination and photography of the skin. In: *Archives of Dermatology* 127 (1991), Nr. 7, p. 1000–1005. – URL http://dx.doi.org/10.1001/archderm.1991.01680060074007

[Antonelli et al. 2010] Antonelli, M. R. ; Pierangelo, A. ; Novikova, T. ; Validire, P. ; Benali, A. ; Gayet, B. ; De Martino, A.: Mueller matrix imaging of human colon tissue for cancer diagnostics: how Monte Carlo modeling can help in the interpretation of experimental data. In: *Optics Express* 18 (2010), Nr. 10, p. 10200–10208. – URL https://dx.doi.org/10.1364/OE.18.010200

[Arridge et al. 1992] Arridge, S. R. ; Cope, M. ; Delpy, D. T.: The theoretical basis for the determination of optical pathlengths in tissue: temporal and frequency analysis. In: *Physics in Medicine and Biology* 37 (1992), Nr. 7, p. 1531. – URL http://dx.doi.org/10.1088/0031-9155/37/7/005

[Arridge et al. 1986] Arridge, S. R. ; Cope, M. ; Der Zee, P. van ; Hillson, P. J. ; Delpy, D. T.: Visualisation of the oxygenation state of brain and muscle in newborn infants by near infrared transillumination. In: Bacharach, S.L (Editor): *Information Processing in Medical Imaging: Proceedings of the 9th conference, Washington D.C., 10–14 June 1985*. Springer Netherlands, 1986, p. 155–176. – URL http://dx.doi.org/10.1007/978-94-009-4261-5_12

[Ayata et al. 2004] Ayata, C. ; Dunn, A. K. ; Gursoy-Özdemir, Y. ; Huang, Z. ; Boas, D. A. ; Moskowitz, M. A.: Laser Speckle Flowmetry for the Study of Cerebrovascular Physiology in Normal and Ischemic Mouse Cortex. In: *Journal of Cerebral Blood Flow and Metabolism* 24 (2004), Nr. 7, p. 744–755. – URL http://dx.doi.org/10.1097/01.WCB.0000122745.72175.D5

[Backman et al. 1999] Backman, V. ; Gurjar, R. ; Badizadegan, K. ; Itzkan, L. ; Dasari, R. R. ; Perelman, L. T. ; Feld, M. S.: Polarized light scattering spectroscopy

for quantitative measurement of epithelial cellular structures in situ. In: *IEEE Journal of selected topics in Quantum Electronics* 5 (1999), Nr. 4, p. 1019–1026. – URL http://dx.doi.org/10.1109/2944.796325

[Bailey and Sokolov 2016] Bailey, M. J. ; Sokolov, K.: Depth-resolved measurements with elliptically polarized reflectance spectroscopy. In: *Biomed. Opt. Express* 7 (2016), Nr. 7, p. 2861–2876. – URL http://dx.doi.org/10.1364/BOE.7.002861

[Barakat 1985] Barakat, R.: The Statistical Properties of Partially Polarized Light. In: *Optica Acta: International Journal of Optics* 32 (1985), Nr. 3, p. 295–312. – URL http://dx.doi.org/10.1080/713821736

[Bartlett and Jiang 2002] Bartlett, M. ; Jiang, H. B.: Measurement of particle size distribution in multilayered skin phantoms using polarized light spectroscopy. In: *Physical Review E* 65 (2002), Nr. 3, 1. – URL http://dx.doi.org/10.1103/PhysRevE.65.031906

[Beard 2011] Beard, P.: Biomedical photoacoustic imaging. In: *Interface Focus* 1 (2011), Nr. 4, p. 602–631. – URL http://dx.doi.org/10.1098/rsfs.2011.0028

[Beaurepaire et al. 1999] Beaurepaire, E. ; Moreaux, L. ; Amblard, F. ; Mertz, J.: Combined scanning optical coherence and two-photon-excited fluorescence microscopy. In: *Optics Letters* 24 (1999), Nr. 14, p. 969–971. – URL http://dx.doi.org/10.1364/OL.24.000969

[Berne and Pecora 1976] Berne, B. J. ; Pecora, R.: *Dynamic Light Scattering*. John Wiley and Sons, New York, 1976. – URL http://dx.doi.org/10.1002/pi.4980090216

[Bhutani et al. 2000] Bhutani, V. K. ; Gourley, G. R. ; Adler, S. ; Kreamer, B. ; Dalin, C. ; Johnson, L. H.: Noninvasive Measurement of Total Serum Bilirubin in a Multiracial Predischarge Newborn Population to Assess the Risk of Severe Hyperbilirubinemia. In: *Pediatrics* 106 (2000), Nr. 2, p. e17. – URL http://pediatrics.aappublications.org/content/106/2/e17

[Bickel and Bailey 1985] Bickel, W. S. ; Bailey, W. M.: Stokes vectors, Mueller matrices, and polarized scattered light. In: *Am. J. Phys* 53 (1985), p. 468–478. – URL http://dx.doi.org/10.1119/1.14202

[Bicout and Brosseau 1992] Bicout, D. ; Brosseau, C.: Multiply scattered waves through a spatially random medium : entropy production and depolarization. In: *Journal de Physique I* 2 (1992), Nr. 11, p. 2047–2063. – URL http://dx.doi.org/10.1051/jp1:1992266

[Bicout et al. 1994] Bicout, D. ; Brosseau, C. ; Martinez, A. S. ; Schmitt, J. M.: Depolarization of multiply scattered waves by spherical diffusers: Influence of the size parameter. In: *Phys. Rev. E* 49 (1994), p. 1767–1770. – URL http://dx.doi.org/10.1103/PhysRevE.49.1767

[Boas et al. 1995] Boas, D. A. ; Campbell, L. E. ; Yodh, A. G.: Scattering and Imaging with Diffusing Temporal Field Correlations. In: *Phys. Rev. Lett.* 75 (1995), p. 1855–1858. – URL http://dx.doi.org/10.1103/PhysRevLett.75.1855

[Boas and Dunn 2010] Boas, D. A. ; Dunn, A. K.: Laser speckle contrast imaging in biomedical optics. In: *Journal of biomedical optics* 15 (2010), Nr. 1, p. 011109. – URL http://dx.doi.org/10.1117/1.3285504

[Boas and Yodh 1997] Boas, D. A. ; Yodh, A. G.: Spatially varying dynamical properties of turbid media probed with diffusing temporal light correlation. In: *Journal of the Optical Socitety of America A - Optics Image Science and Vision* 14 (1997), Nr. 1, p. 192–215. – URL http://dx.doi.org/10.1364/JOSAA.14.000192

[Briers 2001] Briers, J. D.: Laser Doppler, speckle and related techniques for blood perfusion mapping and imaging. In: *Physiological Measurement* 22 (2001), Nr. 4, p. R35. – URL http://dx.doi.org/10.1088/0967-3334/22/4/201

[Briers and Fercher 1982] Briers, J. D. ; Fercher, A. F.: Retinal blood-flow visualization by means of laser speckle photography. In: *Investigative Ophthalmology and Visual Science* 22 (1982), Nr. 2, p. 255. – URL http://iovs.arvojournals.org/article.aspx?articleid=2176497

[Briers et al. 1999] Briers, J. D. ; Richards, G. ; He, X. W.: Capillary Blood Flow Monitoring Using Laser Speckle Contrast Analysis (LASCA). In: *Journal of Biomedical Optics* 4 (1999), Nr. 1, p. 164–175. – URL http://dx.doi.org/10.1117/1.429903

[Briers and Webster 1996] Briers, J. D. ; Webster, S.: Laser speckle contrast analysis (LASCA): a nonscanning, full-field technique for monitoring capillary blood flow. In: *Journal of Biomedical Optics* 1 (1996), Nr. 2, p. 174–179. – URL http://dx.doi.org/10.1117/12.231359

[Brigger et al. 2002] Brigger, I. ; Dubernet, C. ; Couvreur, P.: Nanoparticles in cancer therapy and diagnosis. In: *Advanced Drug Delivery Reviews* 54 (2002), Nr. 5, p. 631–651. – URL http://dx.doi.org/10.1016/j.addr.2012.09.006

[Bright 1831] Bright, R.: Serous cysts in the arachnoid. In: *Diseases of the Brain and Nervous system, Part I: Reports on medical cases selected with a view of illustrating the symptoms and cure of diseases by a reference to morbid anatomy* Volume 2. Longman, Rees, Orme, Brown and Green, 1831, p. 437–439

[Brosseau 1995] Brosseau, C.: Statistics of the normalized Stokes parameters for a Gaussian stochastic plane wave field. In: *Appl. Opt.* 34 (1995), Nr. 22, p. 4788–4793. – URL http://dx.doi.org/10.1364/AO.34.004788

[Calin et al. 2014] Calin, M. A. ; Parasca, S. V. ; Savastru, D. ; Manea, D.: Hyperspectral Imaging in the Medical Field: Present and Future. In: *Applied Spectroscopy Reviews* 49 (2014), Nr. 6, p. 435–447. – URL http://dx.doi.org/10.1080/05704928.2013.838678

[Chance et al. 1988] Chance, B. ; Leigh, J. S. ; Miyake, H. ; Smith, D. S. ; Nioka, S. ; Greenfeld, R. ; Finander, M. ; Kaufmann, K. ; Levy, W. ; Young, M. ; Cohen, P. ; Yoshioka, H. ; Boretsky, R.: Comparison of Time-Resolved and Unresolved Measurements of Deoxyhemoglobin in Brain. In: *Proceedings of The National Academy of Sciences* 85 (1988), p. 4971–4975. – URL http://www.jstor.org/stable/32340

[Chandrasekhar 1960] Chandrasekhar, S.: *Radiative transfer*. Courier Dover Publications, 1960

[Chen et al. 2009] Chen, Y. ; Aguirre, A. D. ; Ruvinskaya, L. ; Devor, A. ; Boas, D. A. ; Fujimoto, J. G.: Optical Coherence Tomography (OCT) reveals depth-resolved dynamics during functional brain activation. In: *Journal of Neuroscience Methods* 178 (2009), Nr. 1, p. 162–173. – URL http://dx.doi.org/10.1016/j.jneumeth.2008.11.026

[Cheng 2012] Cheng, R.: *Fluorescence Angular Domain Imaging with Stabilized Intralipid Test Phantom*, Simon Fraser University, Ph.D. Thesis, 2012

[Cheong et al. 1990] Cheong, W. F. ; Prahl, S. A. ; Welch, A. J.: A Review of the Optical Properties of Biological Tissues. In: *IEEE J. Quantum Electron.* 26 (1990), p. 2166–2185. – URL http://dx.doi.org/10.1109/3.64354

[Cherry 2006] Cherry, S. R.: Multimodality in vivo imaging systems: Twice the power or double the trouble?. In: *Annual Review of Biomedical Engineering* 8 (2006), p. 35–62. – URL http://dx.doi.org/10.1146/annurev.bioeng.8.061505.095728

[Chipman 1994] Chipman, R. A.: Polarimetry. In: Bass, M. (Editor): *Handbook of Optics (Vol. II)*. McGraw Hill Education, 1994, p. 1–37

[Chrysostomou et al. 2007] Chrysostomou, A. ; Lucas, P. W. ; Hough, J. H.: Circular polarimetry reveals helical magnetic fields in the young stellar object HH 135-136. In: *Nature* 450 (2007), Nr. 7166, p. 71–73. – URL http://dx.doi.org/10.1038/nature06220

[Cloud 2007] Cloud, G.: Optical Methods in Experimental Mechanics. In: *Experimental Techniques* 31 (2007), Nr. 1, p. 15–19. – URL http://dx.doi.org/10.1111/j.1747-1567.2006.00129.x

[Collett 1990] Collett, E.: *Polarized light : Fundamentals and applications*. Marcel Dekker, New York, 1990. – URL http://nla.gov.au/nla.cat-vn1133995

[Conn 1999] Conn, P. M.: *Methods in Enzymology - Confocal Microscopy*. Volume 307. Academic Press, 1999. – URL http://dx.doi.org/10.1016/S0076-6879(99)07001-9

[Cooper et al. 1996] Cooper, C. E. ; Elwell, C. E. ; Meek, J. H. ; Matcher, S. J. ; Wyatt, J. S. ; Cope, M. ; Delpy, D. T.: The noninvasive measurement of absolute cerebral deoxyhemoglobin concentration and mean optical path length in the neonatal brain by second derivative near infrared spectroscopy. In: *Pediatric Research* 39 (1996), Nr. 1, p. 32–38. – URL http://dx.doi.org/10.1203/00006450-199601000-00005

[Cubeddu et al. 1997] Cubeddu, R. ; Pifferi, A. ; Taroni, P. ; Torricelli, A.: A solid tissue phantom for photon migration studies. In: *Physics in Medicine and Biology* 42 (1997), p. 1971–1977. – URL http://dx.doi.org/10.1088/0031-9155/42/10/011

[Cutler 1929] Cutler, M.: Transillumination as an aid in the diagnosis of breast lesions. In: *The Journal of Surgery, Gynaecology and Obstetrics* 48 (1929), p. 721–729

[Da Silva 2013] Da Silva, A.: Optical Imaging. In: Fanet, H. (Editor): *Photon-Based Medical Imagery*. John Wiley and Sons, Inc., 2013, Chap 7, p. 267–324. – URL http://dx.doi.org/10.1002/9781118601242.ch7

[Da Silva et al. 2012] Da Silva, A. ; Deumié, C. ; Vanzetta, I.: Elliptically polarized light for depth resolved optical imaging. In: *Biomedical Optics Express* 3 (2012), Nr. 11, p. 2907. – URL http://dx.doi.org/10.1364/BIOMED.2012.BTu3A.14

[Delpy et al. 1988] Delpy, D. T. ; Cope, M. ; Der Zee, P. van ; Arridge, S. R. ; Wray, S. ; Wyatt, J.: Estimation of optical pathlength through tissue from direct time of flight measurement. In: *Physics in Medicine and Biology* 33 (1988), Nr. 12, p. 1433. – URL http://dx.doi.org/10.1088/0031-9155/33/12/008

[Demos and Alfano 1996] Demos, S. G. ; Alfano, R. R.: Temporal gating in highly scattering media by the degree of optical polarization. In: *Optics Letters* 21 (1996), Nr. 2, p. 161–163. – URL http://dx.doi.org/10.1364/OL.21.000161

[Demos and Alfano 1997] Demos, S. G. ; Alfano, R. R.: Optical polarization imaging. In: *Applied optics* 36 (1997), p. 150–155. – URL http://dx.doi.org/10.1364/AO.36.000150

[Demos et al. 2000] Demos, S. G. ; Radousky, H. B. ; Alfano, R. R.: Deep subsurface imaging in tissues using spectral and polarization filtering. In: *Optics Express* 7 (2000), Nr. 1, p. 23–28. – URL http://dx.doi.org/10.1364/OE.7.000023

[Dirnagl et al. 1989] Dirnagl, U. ; Kaplan, B. ; Jacewicz, M. ; Pulsinelli, W.: Continuous Measurement of Cerebral Cortical Blood Flow by Laser-Doppler Flowmetry in a Rat Stroke Model. In: *Journal of Cerebral Blood Flow and Metabolism* 9 (1989), Nr. 5, p. 589–596. – URL http://dx.doi.org/10.1038/jcbfm.1989.84

[Draijer et al. 2009] Draijer, M. ; Hondebrink, E. ; Leeuwen, T. van ; Steenbergen, W.: Review of laser speckle contrast techniques for visualizing tissue perfusion. In: *Lasers in Medical Science* 24 (2009), Nr. 4, p. 639–651. – URL http://dx.doi.org/10.1007/s10103-008-0626-3

[Ducros et al. 2001] Ducros, M. G. ; Marsack, J. D. ; Rylander, H. G. ; Thomsen, S. L. ; Milner, T. E.: Primate retina imaging with polarization-sensitive optical coherence tomography. In: *Journal of the Optical Society of America A-Optics Image Science and Vision* 18 (2001), Nr. 12, p. 2945–2956. – URL http://dx.doi.org/10.1364/JOSAA.18.002945

[Dunn et al. 2001] Dunn, A. K. ; Bolay, T. ; Moskowitz, M. A. ; Boas, D. A.: Dynamic imaging of cerebral blood flow using laser speckle. In: *Journal of Cerebral Blood Flow and Metabolism* 21 (2001), Nr. 3, p. 195–201. – URL http://dx.doi.org/10.1097/00004647-200103000-00002

[Durduran et al. 2010] Durduran, T. ; Choe, R. ; Baker, W. B. ; Yodh, A. G.: Diffuse optics for tissue monitoring and tomography. In: *Reports on Progress in Physics* 73 (2010), Nr. 7, p. 076701. – URL http://dx.doi.org/10.1088/0034-4885/73/7/076701

[Elies et al. 1997] Elies, P. ; Jeune, B. L. ; Roy-Brehonnet, F. L. ; Cariou, J. ; Lotrian, J.: Experimental investigation of the speckle polarization for a polished aluminium sample. In: *Journal of Physics D: Applied Physics* 30 (1997), Nr. 1, p. 29. – URL http://dx.doi.org/10.1088/0022-3727/30/1/006

[Falconet et al. 2008] Falconet, J. ; Sablong, R. ; Perrin, E. ; Jaillon, F. ; Saint-Jalmes, H.: Analysis of simulated and experimental backscattered images of turbid media in

linearly polarized light: estimation of the anisotropy factor. In: *Applied Optics* 47 (2008), Nr. 31, p. 5811–5820. – URL http://dx.doi.org/10.1364/AO.47.005811

[Farrell and Patterson 1992] Farrell, T. J. ; Patterson, M. S.: A diffusion theory model of spatially resolved, steady-state diffuse reflectance for the noninvasive determination of tissue optical properties in vivo. In: *Medical Physics* 19 (1992), p. 879–88. – URL http://dx.doi.org/10.1118/1.596777

[Feng et al. 2013] Feng, X. ; Sun, L. ; Zhang, E.: Depth selectivity for the assessment of microstructure by polarization studies. In: *Biomedical optics express* 4 (2013), Nr. 6, p. 958–66. – URL http://dx.doi.org/10.1364/BOE.4.000958

[Fercher and Briers 1981] Fercher, A. F. ; Briers, J. D.: Flow visualization by means of single-exposure speckle photography. In: *Optics Communications* 37 (1981), Nr. 5, p. 326 – 330. – URL http://dx.doi.org/10.1016/0030-4018(81)90428-4

[Fercher and Steeger 1981] Fercher, A.F. ; Steeger, P. F.: First-order Statistics of Stokes Parameters in Speckle Fields. In: *Optica Acta: International Journal of Optics* 28 (1981), Nr. 4, p. 443–448. – URL http://dx.doi.org/10.1080/713820577

[Freund et al. 1990] Freund, I. ; Kaveh, M. ; Berkovits, R. ; Rosenbluh, M.: Universal polarization correlations and microstatistics of optical waves in random media. In: *Phys. Rev. B* 42 (1990), p. 2613–2616. – URL http://dx.doi.org/10.1103/PhysRevB.42.2613

[Friedland et al. 2003] Friedland, S. ; Benaron, D. ; Parachikov, I. ; Soetikno, R.: Measurement of mucosal capillary hemoglobin oxygen saturation in the colon by reflectance spectrophotometry. In: *Gastrointestinal Endoscopy* 57 (2003), Nr. 4, p. 492 – 497. – URL http://dx.doi.org/10.1067/mge.2003.162

[Fujimoto et al. 1995] Fujimoto, J. G. ; Brezinski, M. E. ; Tearney, G. J. ; Boppart, S. A. ; Bouma, B. ; Hee, M. R. ; Southern, J. F. ; Swanson, E. A.: Optical Biopsy and imaging using Optical Coherence Tomography. In: *Nature Medicine* 1 (1995), Nr. 9, p. 970–972. – URL http://dx.doi.org/10.1038/nm0995-970

[Fujimoto and Farkas 2009] Fujimoto, J. G. ; Farkas, D.: *Biomedical Optical Imaging*. Oxford University Press, 2009

[Fukuda et al. 2005] Fukuda, M. ; Rajagopalan, U. M. ; Homma, R. ; Matsumoto, M. ; Nishizaki, M. ; Tanifuji, M.: Localization of activity-dependent changes in blood volume to submillimeter-scale functional domains in cat visual cortex. In: *Cerebral Cortex* 15 (2005), Nr. 6, p. 823–833. – URL http://dx.doi.org/10.1093/cercor/bhh183

[Gadsden et al. 1979] Gadsden, M. ; Rothwell, P. ; Taylor, M. J.: Detection of circularly polarised light from noctilucent clouds. In: *Nature* 278 (1979), p. 628. – URL http://dx.doi.org/10.1038/278628a0

[Gelebart 1998] Gelebart, B.: *Réflectance résolue dans le temps et dans l'espace appliquée à l'étude de milieux stratifiés - preliminary results on biological tissue phantoms.*, Université Paris-Nord, Ph.D. Thesis, 1998

[Georges et al. 2007] Georges, G. ; Deumié, C. ; Amra, C.: Selective probing and imaging in random media based on the elimination of polarized scattering. In: *Optics express* 15 (2007), Nr. 15, p. 9804–9816. – URL http://dx.doi.org/10.1364/OE.15.009804

[Ghosh and Vitkin 2011] Ghosh, N. ; Vitkin, I. A.: Tissue polarimetry: concepts, challenges, applications, and outlook. In: *Journal of Biomedical Optics* 16 (2011), p. 110801. – URL http://dx.doi.org/10.1117/1.3652896

[Gobin et al. 1999] Gobin, L. ; Blanchot, L. ; Saint-Jalmes, H.: Integrating the digitized backscattered image to measure absorption and reduced-scattering coefficients in vivo. In: *Applied optics* 38 (1999), Nr. 19, p. 4217–4227. – URL http://dx.doi.org/10.1364/AO.38.004217

[Goodman 1975] Goodman, J. W.: *Statistical properties of laser speckle patterns*. p. 9–75. In: *Laser Speckle and Related Phenomena*, Springer Berlin Heidelberg, 1975. – URL http://dx.doi.org/10.1007/BFb0111436

[Gozalez and Woods 2002] Gozalez, R. C. ; Woods, R. E.: Digital Image Fundamentals. In: *Digital Image Processing*. 2nd. New Jersey, Prentice Hall, 2002

[Gurjar et al. 2001] Gurjar, R. S. ; Backman, V. ; Perelman, L. T. ; Georgakoudi, I. ; Badizadegan, K. ; Itzkan, I. ; Dasari, R. R. ; Feld, M. S.: Imaging human epithelial properties with polarized light-scattering spectroscopy. In: *Nature Medicine* 7 (2001), Nr. 11, p. 1245–1248. – URL http://dx.doi.org/10.1038/nm1101-1245

[Hebden et al. 1997] Hebden, J. C. ; Arridge, S. R. ; Delpy, D. T.: Optical imaging in medicine: I. Experimental techniques. In: *Physics in Medicine and Biology* 42 (1997), Nr. 5, p. 825. – URL http://dx.doi.org/10.1088/0031-9155/42/5/007

[Henderson et al. 1985] Henderson, T. C. ; Triendl, E. E. ; Winter, R.: Edge-and Shape-Based Geometric Registration. In: *IEEE Transactions on Geoscience and Remote Sensing* GE-23 (1985), Nr. 3, p. 334–342. – URL http://dx.doi.org/10.1109/TGRS.1985.289536

[Hielscher et al. 1997] Hielscher, A. H. ; Eick, A. A. ; Mourant, J. R. ; Shen, D. ; Freyer, J. P. ; Bigio, I. J.: Diffuse backscattering Mueller matrices of highly scattering media. In: *Optics Express* 1 (1997), Nr. 13, p. 441–453. – URL http://dx.doi.org/10.1364/OE.1.000441

[Huang et al. 1991] Huang, D. ; Swanson, E. A. ; Lin, C. P. ; Schuman, J. S. ; Stinson, W. G. ; Chang, W. ; Hee, M. R. ; Flotte, T. ; Gregory, K. ; Puliafito, C. A. ; Fujimoto, J. G.: Optical Coherence Tomography. In: *Science* 254 (1991), Nr. 5035, p. 1178–1181. – URL http://dx.doi.org/10.1126/science.1957169

[Ishimaru 1978] Ishimaru, A.: . Volume 2. Academic press New York, 1978

[Jacques 1999] Jacques, S. L.: *Video imaging of superficial biological tissue layers using polarized light*. 1999. – URL http://www.google.ca/patents/CA2321842A1?cl=en. – CA Patent App. CA 2,321,842

[Jacques 2013] Jacques, S. L.: Corrigendum: Optical properties of biological tissues: a review. In: *Physics in Medicine and Biology* 58 (2013), p. 5007–5008. – URL http://dx.doi.org/10.1088/0031-9155/58/14/5007

[Jacques et al. 2002] Jacques, S. L. ; Ramella-Roman, J. C. ; Lee, K.: Imaging skin pathology with polarized light. In: *Journal of biomedical optics* 7 (2002), Nr. 3, p. 329–340. – URL http://dx.doi.org/10.1117/1.1484498

[Jacques et al. 2000] Jacques, S. L. ; Roman, J. R. ; Lee, K.: Imaging superficial tissues with polarized light. In: *Lasers in Surgery and Medicine* 26 (2000), Nr. 2, p. 119–129. – URL http://dx.doi.org/10.1002/(SICI)1096-9101(2000)26:2<119::AID-LSM3>3.0.CO;2-Y

[Jaiswal et al. 2003] Jaiswal, J. K. ; Mattoussi, H. ; Mauro, J. M. ; Simon, S. M.: Long-term multiple color imaging of live cells using quantum dot bioconjugates. In: *Nature Biotechnology* 21 (2003), Nr. 1, p. 47–51. – URL http://dx.doi.org/10.1038/nbt767

[Jöbsis 1977] Jöbsis, F. F.: Noninvasive, infrared monitoring of cerebral and myocardial oxygen sufficiency and circulatory parameters. In: *Science* 198 (1977), Nr. 4323, p. 1264–1267. – URL http://dx.doi.org/10.1126/science.929199

[Jones 1941] Jones, R. C.: A New Calculus for the Treatment of Optical Systems, I. Description and Discussion of the Calculus. In: *J. Opt. Soc. Am.* 31 (1941), Nr. 7, p. 488–493. – URL http://dx.doi.org/10.1364/JOSA.31.000488

[Kapsokalyvas et al. 2013] Kapsokalyvas, D. ; Bruscino, N. ; Alfieri, D. ; Giorgi, V. de ; Cannarozzo, G. ; Cicchi, R. ; Massi, D. ; Pimpinelli, N. ; Pavone, F. S.: Spectral morphological analysis of skin lesions with a polarization multispectral dermoscope. In: *Optics express* 21 (2013), Nr. 4, p. 4826–40. – URL http://dx.doi.org/10.1364/OE.21.004826

[Kirkpatrick et al. 2008] Kirkpatrick, S. J. ; Duncan, D. D. ; Wells-Gray, E. M.: Detrimental effects of speckle-pixel size matching in laser speckle contrast imaging. In: *Opt. Lett.* 33 (2008), Nr. 24, p. 2886–2888. – URL http://dx.doi.org/10.1364/OL.33.002886

[Kliger et al. 1990] Kliger, D. S. ; Lewis, J. W. ; Randall, C. E.: Polarization properties of Light. In: Kliger, D. S. (Editor) ; Lewis, J. W. (Editor) ; Randall, C. E. (Editor): *Polarized Light in Optics and Spectroscopy*. Academic Press, 1990, p. 1 – 7. – URL http://dx.doi.org/10.1016/B978-0-08-057104-1.50004-1

[Kollias 1995] Kollias, N.: The spectroscopy of human melanin pigmentation. In: *Melanin: Its Role in Human Photoprotection*. Valdenmar Publishing Co., 1995, p. 31–38

[Kollias and Baqer 1985] Kollias, N. ; Baqer, A.: Spectroscopic Characteristics of Human Melanin In Vivo. In: *Journal of Investigative Dermatology* 85 (1985), Nr. 1, p. 38 – 42. – URL http://dx.doi.org/10.1111/1523-1747.ep12275011

[Kumar and Richards-Kortum 2006] Kumar, S. ; Richards-Kortum, R.: Optical molecular imaging agents for cancer diagnostics and therapeutics. In: *Nanomedicine* 1 (2006), Nr. 1, p. 23–30. – URL http://dx.doi.org/10.2217/17435889.1.1.23

[Kunnen et al. 2015] Kunnen, B. ; Macdonald, C. ; Doronin, A. ; Jacques, S. ; Eccles, M. ; Meglinski, I.: Application of circularly polarized light for non-invasive diagnosis of cancerous tissues and turbid tissue-like scattering media. In: *Journal of Biophotonics* 8 (2015), Nr. 4, p. 317–323. – URL http://dx.doi.org/10.1002/jbio.201400104

[Lauterbur 1973] Lauterbur, P. C.: Image formation by induced local interactions: examples employing nuclear magnetic resonance. In: *Nature* (1973), Nr. 242, p. 190–191. – URL http://dx.doi.org/10.1038/242190a0

[Leahy et al. 2007] Leahy, M. J. ; Enfield, J. G. ; Clancy, N. T. ; O'Doherty, J. ; McNamara, P. ; Nilsson, G. E.: Biophotonic methods in microcirculation imaging. In: *Medical Laser Application* 22 (2007), Nr. 2, p. 105 –126. – URL http://dx.doi.org/10.1016/j.mla.2007.06.003

[Lemieux and Durian 1999] Lemieux, P.-A. ; Durian, D. J.: Investigating non-Gaussian scattering processes by using nth-order intensity correlation functions. In: *J. Opt. Soc. Am. A* 16 (1999), Nr. 7, p. 1651–1664. – URL http://dx.doi.org/10.1364/JOSAA.16.001651

[Li et al. 2002] Li, J. ; Yao, G. ; Wang, L. V.: Degree of polarization in laser speckles from turbid media: Implications in tissue optics. In: *Journal of Biomedical Optics* 7 (2002), Nr. 3, p. 307–312. – URL http://dx.doi.org/10.1117/1.1483313

[Licha et al. 2008] Licha, K. ; Schirner, M. ; Henry, G.: Optical Agents. In: Semmler, W. (Editor) ; Schwaiger, M. (Editor): *Handbook of Experimental Pharmacology* Volume 185/1. Springer Berlin Heidelberg, 2008, p. 203–222. – URL http://dx.doi.org/10.1007/978-3-540-72718-7_10

[Liu et al. 2005] Liu, Y. ; Kim, Y. L. ; Li, X. ; Backman, V.: Investigation of depth selectivity of polarization gating for tissue characterization. In: *Optics Express* 13 (2005), Nr. 2, p. 601–611. – URL http://dx.doi.org/10.1364/OPEX.13.000601

[Lu and Fei 2014] Lu, G. ; Fei, B.: Medical hyperspectral imaging: a review. In: *Journal of Biomedical Optics* 19 (2014), Nr. 1. – URL http://dx.doi.org/10.1117/1.JBO.19.1.010901

[M. F. G.Wood and Vitkin 2010] M. F. G.Wood, X. G. ; Vitkin, I. A.: Towards noninvasive glucose sensing using polarization analysis of multiply scattered light. In: Tuchin, V. V. (Editor): *Handbook of Optical Sensing of Glucose in Biological Fluids and Tissues: Series in Medical Physics and Biomedical Engineering* Volume 12. Taylor and Francis Publishing, London, 2010, Chap 17

[MacKintosh et al. 1989] MacKintosh, F. C. ; Zhu, J. X. ; Pine, D. J. ; Weitz, D. A.: Polarization memory of multiply scattered light. In: *Phys. Rev. B* 40 (1989), p. 9342–9345. – URL http://dx.doi.org/10.1103/PhysRevB.40.9342

[Maheswari et al. 2003] Maheswari, R. U. ; Takaoka, H. ; Kadono, H. ; Homma, R. ; Tanifuji, M.: Novel functional imaging technique from brain surface with optical coherence tomography enabling visualization of depth resolved functional structure in vivo. In: *Journal of Neuroscience Methods* 124 (2003), Nr. 1, p. 83–92. – URL http://dx.doi.org/10.1016/S0165-0270(02)00370-9

[Mansfield and Maudsley 1977] Mansfield, P. ; Maudsley, A. A.: Medical Imaging by NMR. In: *The British Journal of Radiology* 50 (1977), Nr. 591, p. 188–194

[Matcher et al. 1994] Matcher, S. J. ; Cope, M. ; Delpy, D. T.: Use of the water absorption spectrum to quantify tissue chromophore concentration changes in near-infrared

spectroscopy. In: *Physics in Medicine and Biology* 39 (1994), Nr. 1, p. 177. – URL http://dx.doi.org/10.1088/0031-9155/39/1/011

[Mattes et al. 2001] Mattes, D. ; Haynor, D. R. ; Vesselle, H. ; Lewellyn, T. K. ; Eubank, W.: *Nonrigid multimodality image registration*. 2001. – URL http://dx.doi.org/10.1117/12.431046

[McCormack et al. 2014] McCormack, D. R. ; Walsh, A. J. ; Sit, W. ; Arteaga, Carlos L. ; Chen, J. ; Cook, R. S. ; Skala, M. C.: In vivo hyperspectral imaging of microvessel response to trastuzumab treatment in breast cancer xenografts. In: *Biomedical Optics Express* 5 (2014), Nr. 7, p. 2247–2261. – URL http://dx.doi.org/10.1364/BOE.5.002247

[McNichols and Coté 2000] McNichols, R.J. ; Coté, G. L.: Optical glucose sensing in biological fluids: an overview. In: *Journal of Biomedical Optics* 5 (2000), Nr. 1, p. 5–16. – URL http://dx.doi.org/10.1117/1.429962

[Medintz et al. 2005] Medintz, I. L. ; Uyeda, H. T. ; Goldman, E. R. ; Mattoussi, H.: Quantum dot bioconjugates for imaging, labelling and sensing. In: *Nature Materials* 4 (2005), Nr. 6, p. 435–446. – URL http://dx.doi.org/10.1038/nmat1390

[Mesradi et al. 2013] Mesradi, M. ; Genoux, A. ; Cuplov, V. ; Abi Haidar, D. ; Jan, S. ; Buvat, I. ; Pain, F.: Experimental and analytical comparative study of optical coefficient of fresh and frozen rat tissues. In: *Journal of Biomedical Optics* 18 (2013), Nr. 11, p. 117010–117010. – URL http://dx.doi.org/10.1117/1.JBO.18.11.117010

[Minsky 1988] Minsky, M.: Memoir on inventing the confocal scanning microscope. In: *Scanning* 10 (1988), Nr. 4, p. 128–138. – URL http://dx.doi.org/10.1002/sca.4950100403

[Moré 1978] Moré, J. J.: *Numerical Analysis: Proceedings of the Biennial Conference Held at Dundee, June 28–July 1, 1977*. Chap The Levenberg-Marquardt algorithm: Implementation and theory, p. 105–116, Springer Berlin Heidelberg, 1978. – URL http://dx.doi.org/10.1007/BFb0067700

[Morgan et al. 2005] Morgan, N. Y. ; English, S. ; Chen, W. ; Chernomordik, V. ; Russo, A. ; Smith, P. D. ; Gandjbakhche, A.: Real time in vivo non-invasive optical imaging using near-infrared fluorescent quantum dots. In: *Academic Radiology* 12 (2005), Nr. 3, p. 313–323. – URL http://dx.doi.org/10.1016/j.acra.2004.04.023

[Morgan et al. 1997] Morgan, S. P. ; Khong, M. P. ; Somekh, M. G.: Effects of polarization state and scatterer concentration on optical imaging through scattering media. In: *Appl. Opt.* 36 (1997), Nr. 7, p. 1560–1565. – URL http://dx.doi.org/10.1364/AO.36.001560

[Morgan et al. 2006] Morgan, S. P. ; Lu, B. ; Stockford, I. M. ; Pitter, M. C. ; Crowe, J. A. ; Hayes-Gill, B. R.: Modelling and instrumentation for polarized light imaging and spectroscopy of scattering media - art. no. 604712. In: *Fourth International Conference on Photonics and Imaging in Biology and Medicine, Pts 1 and 2* 6047 (2006), p. 4712. – URL http://dx.doi.org/10.1117/12.710963

[Morgan and Ridgway 2000] Morgan, S. P. ; Ridgway, M.: Polarization properties of light backscattered from a two layer scattering medium. In: *Optics express* 7 (2000), Nr. 12, p. 395–402. – URL http://dx.doi.org/10.1364/OE.7.000395

[Morgan and Stockford 2003] Morgan, S. P. ; Stockford, I. M.: Surface-reflection elimination in polarization imaging of superficial tissue. In: *Optics letters* 28 (2003), Nr. 2, p. 114–116. – URL http://dx.doi.org/10.1364/OL.28.000114

[Mueller 1943] Mueller, H.: Memorandum on the polarization optics of the photoelastic shutter. In: *Report No. 2 of OSR, project OEMsr-576* (1943)

[N. Ghosh and Vitkin 2010] N. Ghosh, M. F. G. W. ; Vitkin, I. A.: Polarized light assessment of complex turbid media such as biological tissues using Mueller matrix decomposition,. In: Tuchin, V. V. (Editor): *Handbook of Photonics for Biomedical Science*. Taylor and Francis Publishing, London, 2010, Chap 9, p. 253–282

[Nutt 2002] Nutt, R.: The History of Positron Emission Tomography. In: *Molecular Imaging and Biology* 4 (2002), Nr. 1, p. 11 – 26. – URL http://dx.doi.org/10.1016/S1095-0397(00)00051-0

[Oliver 1963] Oliver, B. M.: Sparkling spots and random diffraction. In: *Proceedings of the IEEE* 51 (1963), Nr. 1, p. 220–221. – URL http://dx.doi.org/10.1109/PROC.1963.1686

[Ostermeyer et al. 1996] Ostermeyer, M. R. ; Stephens, D. V. ; Wang, L. ; Jacques, S. L.: Nearfield polarization effects on light propagation in random media. In: *Biomedical Optical Spectroscopy and Diagnostics*, URL http://dx.doi.org/10.1364/AO.36.001560, 1996, p. SP2

[Patton and Budinger 2003] Patton, J. A. ; Budinger, T. F.: Single Photon Emission Computed Tomography. In: Sandler, M. P. (Editor) ; Coleman, R. E. (Editor) ; Patton, J. A. (Editor) ; Wackers, F. J. T. (Editor) ; Gottschalk, A. (Editor): *Diagnostic Nuclear Medicine*. 4th. Lippincott Williams and Wilkins, 2003

[Pedersen 1976] Pedersen, H. M.: Theory of speckle dependence on surface roughness*. In: *J. Opt. Soc. Am.* 66 (1976), Nr. 11, p. 1204–1210. – URL http://dx.doi.org/10.1364/JOSA.66.001204

[Pierangelo et al. 2011] Pierangelo, A. ; Benali, A. ; Antonelli, M.-R. ; Novikova, T. ; Validire, P. ; Gayet, B. ; De Martino, A.: Ex-vivo characterization of human colon cancer by Mueller polarimetric imaging. In: *Optics Express* 19 (2011), Nr. 2, p. 1582–1593. – URL http://dx.doi.org/10.1364/OE.19.001582

[Pierangelo et al. 2013] Pierangelo, A. ; Nazac, A. ; Benali, A. ; Validire, P. ; Cohen, H. ; Novikova, T. ; Ibrahim, B. H. ; Manhas, S. ; Fallet, C. ; Antonelli, R. ; Martino, A.: Polarimetric imaging of uterine cervix : a case study. In: *Optics Express* 21 (2013), Nr. 12, p. 14120. – URL http://dx.doi.org/10.1364/OE.21.014120

[Pluim et al. 2000] Pluim, J. P. W. ; Maintz, J. B. A. ; Viergever, M. A.: Image registration by maximization of combined mutual information and gradient information. In: *IEEE Transactions on Medical Imaging* 19 (2000), Nr. 8, p. 809–814. – URL http://dx.doi.org/10.1109/42.876307

[Pluim et al. 2003] Pluim, J. P. W. ; Maintz, J. B. A. ; Viergever, M. A.: Mutual-information-based registration of medical images: a survey. In: *IEEE Transactions on Medical Imaging* 22 (2003), Nr. 8, p. 986–1004. – URL http://dx.doi.org/10.1109/TMI.2003.815867

[Pointcaré 1892] Pointcaré, H.: *Theorie mathematique de la lumiere vol. 2*. G. Carre, Paris, 1892

[Prahl et al. 1993] Prahl, S. A. ; Gemert, M. J. C. van ; Welch, A. J.: Determining the optical properties of turbid media by using the adding–doubling method. In: *Appl. Opt.* 32 (1993), Nr. 4, p. 559–568. – URL http://dx.doi.org/10.1364/AO.32.000559

[Puliafito et al. 1995] Puliafito, C. A. ; Hee, M. R. ; Lin, C. P. ; Reichel, E. ; Schuman, J. S. ; Duker, J. S. ; Izatt, J. A. ; Swanson, E. A. ; Fujimoto, J. G.: Imaging of Macular Diseases with Optical Coherence Tomography. In: *Ophthalmology* 102 (1995), Nr. 2, p. 217 – 229. – URL http://dx.doi.org/10.1016/S0161-6420(95)31032-9

[Rakovic et al. 1999] Rakovic, M. J. ; Kattawar, G. W. ; Mehrubeoglu, M. ; Cameron, B. D. ; Wang, L. V. ; Rastegar, S. ; Cote, G. L.: Light backscattering polarization patterns from turbid media: theory and experiment. In: *Applied Optics* 38 (1999), Nr. 15, p. 3399–3408. – URL http://dx.doi.org/10.1364/AO.38.003399

[Ramella-Roman et al. 2004] Ramella-Roman, J. C. ; Lee, K. ; Prahl, S. A. ; Jacques, S. L.: Design, testing, and clinical studies of a handheld polarized light camera. In: *Journal of Biomedical Optics* 9 (2004), p. 1305–1310. – URL http://dx.doi.org/10.1117/1.1781667

[Ramella-Roman et al. 2011] Ramella-Roman, J. C. ; Nayak, A. ; Prahl, S. A.: A Spectroscopic sensitive polarimeter for biomedical applications. In: *Journal of Biomedical Optics* 16 (2011), p. 047001. – URL http://dx.doi.org/10.1117/1.3561907

[Ramella-Roman et al. 2005] Ramella-Roman, J. C. ; Prahl, S. A. ; Jacques, S. L.: Three Monte Carlo programs of polarized light transport into scattering media: part I. In: *Opt. Express* 13 (2005), Nr. 12, p. 4420–4438. – URL http://dx.doi.org/10.1364/OPEX.13.004420

[Rehn 2012] Rehn, S.: *Imagerie sélective des tissus biologiques: Apport de la polarisation pour une sélection en profondeur.*, Université d'Aix-Marseille, Ph.D. Thesis, 2012

[Rehn et al. 2013] Rehn, S. ; Planat-Chrétien, A. ; Berger, M. l. ; Dinten, J.-M. ; Deumié, C. ; Da Silva, A.: Depth probing of diffuse tissues controlled with elliptically polarized light. In: *Journal of biomedical optics* 18 (2013), p. 16007. – URL http://dx.doi.org/10.1117/1.JBO.18.1.016007

[Rigden and Gordon 1962] Rigden, J. D. ; Gordon, E. I.: The granularity of scattered optical maser light. In: *Proc. of the Institute of Radio Engineers* 50 (1962), p. 2367–2368

[Röntgen 1898] Röntgen, W. K.: Über eine neue Art von Strahlen. In: *Annalen der Physik* 300 (1898), Nr. 1, p. 12–17

[Rowe et al. 1995] Rowe, M. P. ; Pugh, E. N. ; Tyo, J. S. ; Engheta, N.: Polarization-difference imaging–a biologically inspired technique for observation through scattering media. In: *Optics Letters* 20 (1995), Nr. 6, p. 608–610. – URL http://dx.doi.org/10.1364/OL.20.000608

[Sankaran et al. 1999] Sankaran, V. ; Everett, M. J. ; Maitland, D. J. ; Walsh, J. T.: Comparison of polarized-light propagation in biological tissue and phantoms. In: *Opt. Lett.* 24 (1999), Nr. 15, p. 1044–1046. – URL http://dx.doi.org/10.1364/OL.24.001044

[Sassaroli and Fantini 2004] Sassaroli, A. ; Fantini, S.: Comment on the modified Beer–Lambert law for scattering media. In: *Physics in Medicine and Biology* 49 (2004), Nr. 14, p. 255. – URL http://dx.doi.org/10.1088/0031-9155/49/14/N07

[Schmitt et al. 1992] Schmitt, J. M. ; Gandjbakhche, A. H. ; Bonner, R. F.: Use of polarized-light to discriminate short-path photons in a multiply scattering medium. In: *Applied Optics* 31 (1992), Nr. 30, p. 6535–6546. – URL http://dx.doi.org/10.1364/AO.31.006535

[Schuman et al. 1995] Schuman, J. S. ; Hee, M. R. ; Puliafito, C. A. ; Wong, C. ; Pedut-Kloizman, T. ; Lin, C. P. ; Hertzmark, Izatt-J. A. ; Swanson, E. A. ; Fujimoto, J. G.: Quantification of nerve fiber layer thickness in normal and glaucomatous eyes using optical coherence tomography: A pilot study. In: *Archives of Ophthalmology* 113 (1995), Nr. 5, p. 586–596. – URL http://dx.doi.org/10.1001/archopht.1995.01100050054031

[Serganova and Blasberg 2006] Serganova, I. ; Blasberg, R. G.: Multi-Modality Molecular Imaging of Tumors. In: *Hematology/Oncology Clinics of North America* 20 (2006), Nr. 6, p. 1215 – 1248. – URL http://dx.doi.org/10.1016/j.hoc.2006.09.006

[Shukla and Pradhan 2009] Shukla, P. ; Pradhan, A.: Mueller decomposition images for cervical tissue: Potential for discriminating normal and dysplastic states. In: *Optics Express* 17 (2009), Nr. 3, p. 1600–1609. – URL http://dx.doi.org/10.1364/OE.17.001600

[Shung 2005] Shung, K. K.: *Diagnostic Ultrasound: Imaging and Blood Flow Measurements*. Taylor and Francis Group, CRC Press Book, 2005

[Sorg et al. 2005] Sorg, B. S. ; Moeller, B. J. ; Donovan, O. ; Cao, Y. ; Dewhirst, M. W.: Hyperspectral imaging of hemoglobin saturation in tumor microvasculature and tumor hypoxia development. In: *Journal of Biomedical Optics* 10 (2005), Nr. 4, p. 044004–044004–11. – URL http://dx.doi.org/10.1117/1.2003369

[Sridhar and Da Silva 2016a] Sridhar, S. ; Da Silva, A.: Enhanced contrast and depth resolution in polarization imaging using elliptically polarized light. In: *Journal of Biomedical Optics* 21 (2016), Nr. 7, p. 071107. – URL http://dx.doi.org/10.1117/1.JBO.21.7.071107

[Sridhar and Da Silva 2016b] Sridhar, S. ; Da Silva, A.: Protocol using elliptically polarized light for enhanced contrast in polarization gating imaging of biological tissues. In: *Optical Biopsy XIV: Toward Real-Time Spectroscopic Imaging and Diagnosis, SPIE Proceedings* Volume 9703, URL http://dx.doi.org/10.1117/12.2208760, 2016, p. 970319

[van Staveren et al. 1991] Staveren, H. J. van ; Moes, C. J. ; Marie, J. van ; Prahl, S. A. ; Gemert, M. J. van: Light scattering in Intralipid-10% in the wavelength range of 400-1100 nm. In: *Applied optics* 30 (1991), Nr. 31, p. 4507–4514. – URL https://dx.doi.org/10.1364/AO.30.004507

[Steeger and Fercher 1982] Steeger, P. F. ; Fercher, A. F.: Experimental Investigation of the First-order Statistics of Stokes Parameters in Speckle Fields. In: *Optica Acta: International Journal of Optics* 29 (1982), Nr. 10, p. 1395–1400. – URL http://dx.doi.org/10.1080/713820756

[Stern et al. 1977] Stern, M. D. ; Lappe, D. L. ; Bowen, P. D. ; Chimosky, J. E. ; Holloway, G. A. ; Keiser, H. R. ; Bowman, R. L.: Continuous measurement of tissue blood flow by laser-Doppler spectroscopy. In: *American Journal of Physiology* 232 (1977), Nr. 4, p. H441–H448. – URL http://ajpheart.physiology.org/content/232/4/H441

[Stockford et al. 2007] Stockford, I. M. ; Lu, B. ; Crowe, J. A. ; Morgan, S. P. ; Morris, D. E.: Reduction of Error in Spectrophotometry of Scattering Media Using Polarization Techniques. In: *Appl. Spectrosc.* 61 (2007), Nr. 12, p. 1379–1389. – URL http://dx.doi.org/10.1366/000370207783292028

[Stockford and Morgan 2005] Stockford, I. M. ; Morgan, S. P.: Application of a look-up table to polarized light imaging for characterising skin. In: *Saratov Fall Meeting 2004: Optical Technologies in Biophysics and Medicine VI* 5771 (2005), p. 151–158. – URL http://dx.doi.org/10.1117/12.634617

[Stockford et al. 2002] Stockford, I. M. ; Morgan, S. P. ; Chang, P. C. Y. ; Walker, J. G.: Analysis of the spatial distribution of polarized light backscattered from layered scattering media. In: *Journal of biomedical optics* 7 (2002), Nr. 3, p. 313–320. – URL http://dx.doi.org/10.1117/1.1483316

[Stokes 1901] Stokes, G. G.: *Mathematical and Physical Papers*. Volume 3. Cambridge University Press, 1901. – URL http://dx.doi.org/10.1017/CBO9780511702266

[Strupler et al. 2007] Strupler, M. ; Pena, A.-M. ; Hernest, M. ; Tharaux, P. L. ; Martin, J. L. ; Beaurepaire, E. ; Schanne-Klein, M. C.: Second harmonic imaging and scoring of collagen in fibrotic tissues. In: *Optics Express* 15 (2007), Nr. 7, p. 4054–4065. – URL http://dx.doi.org/10.1364/OE.15.004054

[Styner et al. 2000] Styner, M. ; Brechbuhler, C. ; Szekely, G. ; Gerig, G.: Parametric estimate of intensity inhomogeneities applied to MRI. In: *IEEE Transactions on Medical Imaging* 19 (2000), Nr. 3, p. 153–165. – URL http://dx.doi.org/10.1109/42.845174

[Sugiyama et al. 2010] Sugiyama, T. ; Araie, M. ; Riva, Charles E. ; Schmetterer, L. ; Orgul, S.: Use of laser speckle flowgraphy in ocular blood flow research. In: *Acta Ophthalmologica* 88 (2010), Nr. 7, p. 723–729. – URL http://dx.doi.org/10.1111/j.1755-3768.2009.01586.x

[Swami et al. 2014] Swami, M. K. ; Patel, H. ; Somyaji, M. R. ; Kushwaha, P. K. ; Gupta, P. K.: Size-dependent patterns in depolarization maps from turbid medium and tissue. In: *Applied Optics* 53 (2014), Nr. 27, p. 6133. – URL http://dx.doi.org/10.1364/AO.53.006133

[Swami et al. 2013] Swami, M. K. ; Patel, H. S. ; Geethu, P. ; Uppal, A. ; Kushwaha, P. K. ; Gupta, P. K.: Effect of gold nanoparticles on depolarization characteristics of Intralipid tissue phantom. In: *Optics letters* 38 (2013), Nr. 15, p. 2855–7. – URL http://dx.doi.org/10.1364/OL.38.002855

[Tarhan and Watson 1992] Tarhan, I. I. ; Watson, G. H.: Polarization microstatistics of laser speckle. In: *Phys. Rev. A* 45 (1992), p. 6013–6018. – URL http://dx.doi.org/10.1103/PhysRevA.45.6013

[Ter-Pogossian et al. 1975] Ter-Pogossian, M. M. ; Phelps, M. E. ; Hoffman, E. J. ; Mullani, N. A.: Positron-emission transaxial tomograph for nuclear imaging (PETT). In: *Radiology* 114 (1975), Nr. 1, p. 89–98. – URL http://dx.doi.org/10.1148/114.1.89

[Tromberg et al. 2005] Tromberg, B. J. ; Cerussi, A. ; Krasieva, T. ; Venugopalan, V. ; Chen, Z.: *Multi-Dimensional Optical Imaging in Thick Tissues: Contrast across spatial scales*. 2005

[Tseng et al. 2009] Tseng, S.-H. ; Hayakawa, C. ; Spanier, J. ; Durkin, A. J.: Investigation of a probe design for facilitating the uses of the standard photon diffusion equation at short source-detector separations: Monte Carlo simulations. In: *Journal of Biomedical Optics* 14 (2009), Nr. 5, p. 054043–054043–12. – URL http://dx.doi.org/10.1117/1.3253386

[Tuchin 2000] Tuchin, V. V.: *Tissue Optics*. SPIE Press, 2000

[Tuchin 2013] Tuchin, V. V.: *Handbook of Coherent-Domain Optical Methods*. Springer-Verlag New York, 2013. – URL https://dx.doi.org/10.1007/978-3-540-45321-5

[Tuchin et al. 2006] Tuchin, V. V. ; Wang, L. V. ; Zimnyakov, D. A.: *Optical Polarization in Biomedical Applications*. Springer Berlin Heidelberg, 2006. – URL https://dx.doi.org/10.1007/978-3-540-45321-5

[Twersky 1962] Twersky, V.: Multiple Scattering of Waves and Optical Phenomena*. In: *J. Opt. Soc. Am.* 52 (1962), Nr. 2, p. 145–171. – URL http://dx.doi.org/10.1364/JOSA.52.000145

[Valdes et al. 2014] Valdes, C. P. ; Varma, H. M. ; Kristoffersen, A. K. ; Dragojevic, T. ; Culver, J. P. ; Durduran, T.: Speckle contrast optical spectroscopy, a non-invasive, diffuse optical method for measuring microvascular blood flow in tissue. In: *Biomedical Optics Express* 5 (2014), Nr. 8, p. 2769. – URL http://dx.doi.org/10.1364/BOE.5.002769

[Jöbsis van der Vliet 1999] Vliet, F. F. Jöbsis van der: Discovery of the Near-Infrared Window into the Body and the Early Development of Near-Infrared Spectroscopy. In: *Journal of Biomedical Optics* 4 (1999), Nr. 4, p. 392–396. – URL http://dx.doi.org/10.1117/1.429952

[Jöbsis van der Vliet and Jöbsis 1999] Vliet, F. F. Jöbsis van der ; Jöbsis, P. D.: Biochemical and Physiological Basis of Medical Near-Infrared Spectroscopy. In: *Journal of Biomedical Optics* 4 (1999), Nr. 4, p. 397–402. – URL http://dx.doi.org/10.1117/1.429953

[Vo-Dinh 2003] Vo-Dinh, T.: *Biomedical Photonics Handbook*. CRC Press, 2003. – URL http://dx.doi.org/10.1201/9780203008997.sec1

[Wang et al. 2004] Wang, H. Z. ; Wang, H. Y. ; Liang, R. Q. ; Ruan, K. C.: Detection of tumor marker CA125 in ovarian carcinoma using quantum dots. In: *Acta Biochimica et Biophysica Sinica* 36 (2004), Nr. 10, p. 681–686. – URL https://dx.doi.org/10.1093/abbs/36.10.681

[Wang et al. 2002] Wang, L. V. ; Coté, G. L. ; Jacques, S. L.: Special Section Guest Editorial: Tissue Polarimetry. In: *Journal of Biomedical Optics* 7 (2002), Nr. 3, p. 278–278. – URL http://dx.doi.org/10.1117/1.1489434

[Wang and Wang 2002] Wang, X. D. ; Wang, L. H. V.: Propagation of polarized light in birefringent turbid media: A Monte Carlo study. In: *Journal of Biomedical Optics* 7 (2002), Nr. 3, p. 279–29. – URL https://dx.doi.org/10.1117/1.1483315

[Weinreb and Khaw 2004] Weinreb, R. N. ; Khaw, P. T.: Primary open-angle glaucoma. In: *The Lancet* 363 (2004), Nr. 9422, p. 1711–1720. – URL http://dx.doi.org/10.1016/S0140-6736(04)16257-0

[Weissleder and Ntziachristos 2003] Weissleder, R. ; Ntziachristos, V.: Shedding light onto live molecular targets. In: *Nature Medicine* 9 (2003), Nr. 1, p. 123–128. – URL https://dx.doi.org/10.1038/nm0103-123

[Wild and Reid 1952] Wild, J. J. ; Reid, J. M.: Application of Echo-Ranging Techniques to the Determination of Structure of Biological Tissues. In: *Science* 115 (1952), p. 226–230

[Wilson 1990] Wilson, T.: *Confocal Microscopy*. Academic Press, 1990

[Wyatt et al. 1990] Wyatt, J. S. ; Cope, M. ; Delpy, D. T. ; Richardson, C. E. ; Edwards, A. D. ; Wray, S. ; Reynolds, E. O.: Quantification of cerebral blood volume in human infants by near-infrared spectroscopy. In: *Journal of Applied Physiology* 68 (1990), Nr. 3, p. 1086–1091. – URL http://jap.physiology.org/content/68/3/1086

[Yasui et al. 2004] Yasui, T. ; Tohno, Y. ; Araki, T.: Characterization of collagen orientation in human dermis by two-dimensional second-harmonic-generation polarimetry. In: *Journal of Biomedical Optics* 9 (2004), Nr. 2, p. 259–264. – URL https://dx.doi.org/10.1117/1.1644116

[Yodh and Chance 1995] Yodh, A. ; Chance, B.: Spectroscopy and imaging with diffusing light. In: *Physics Today* 48 (1995), Nr. 3, p. 34–40. – URL http://dx.doi.org/10.1063/1.881445

[Yoo and Alfano 1989] Yoo, K. M. ; Alfano, R. R.: Time resolved depolarization of multiple backscattered light from random media. In: *Physics Letters A* 142 (1989), Nr. 8-9, p. 531–536. – URL http://dx.doi.org/10.1016/0375-9601(89)90530-6

[Yuan 2008] Yuan, S.: *Sensitivity, noise and quantitative model of laser speckle contrast imaging*, Tufts University, Ph.D. Thesis, 2008

[Yuan et al. 2005] Yuan, S. ; Devor, A. ; Boas, D. A. ; Dunn, A. K.: Determination of optimal exposure time for imaging of blood flow changes with laser speckle contrast imaging. In: *Appl. Opt.* 44 (2005), Nr. 10, p. 1823–1830. – URL http://dx.doi.org/10.1364/AO.44.001823

[Zhang et al. 2007] Zhang, L. ; Lee, K. C. ; Bhojani, M. S. ; Khan, A. P. ; Shilman, A. ; Holland, E. C. ; Ross, B. D. ; Rehemtulla, A.: Molecular imaging of AKT kinase activity. In: *Nature Medicine* 13 (2007), Nr. 9, p. 1114–1119. – URL https://dx.doi.org/10.1038/nm1608

[Zimnyakov et al. 1997] Zimnyakov, D. A. ; Tuchin, V. V. ; Mishin, A. A.: Coherent-domain methods in biomedical optics. In: *Proc. SPIE* Volume 3317, URL http://dx.doi.org/10.1117/12.295702, 1997, p. 342–354

[Zonios et al. 2001] Zonios, G. ; Bykowski, J. ; Kollias, N.: Skin Melanin, Hemoglobin, and Light Scattering Properties can be Quantitatively Assessed In Vivo Using Diffuse Reflectance Spectroscopy. In: *Journal of Investigative Dermatology* 117 (2001), p. 1452 – 1457. – URL http://dx.doi.org/10.1046/j.0022-202x.2001.01577.x

[Zonios and Dimou 2006] Zonios, G. ; Dimou, A.: Modeling diffuse reflectance from semi-infinite turbid media: application to the study of skin optical properties. In: *Opt. Express* 14 (2006), Nr. 19, p. 8661–8674. – URL http://dx.doi.org/10.1364/OE.14.008661

[Zonios et al. 1999] Zonios, G. ; Perelman, L. T. ; Backman, V. ; Manoharan, R. ; Fitzmaurice, M. ; Dam, J. van ; Feld, M. S.: Diffuse reflectance spectroscopy of human adenomatous colon polyps in vivo. In: *Appl. Opt.* 38 (1999), Nr. 31, p. 6628–6637. – URL http://dx.doi.org/10.1364/AO.38.006628

PUBLICATIONS

The results of the work in course of this thesis may have appeared previously in the following peer-review publications, conference proceedings, and presentations:

[i] Susmita Sridhar and Anabela Da Silva; Screening biological tissues in depth with elliptically polarized light imaging. *OptDIAG 2014*, l'Institut de Physique du Globe, Paris, France, 14 - 16 May, 2014. *[Oral Presentation]*.

[ii] Susmita Sridhar and Anabela Da Silva; Enhanced contrast and depth resolution in polarization imaging using elliptically polarized light. *J. Biomed. Opt.*, 21(7):071107, 2016.

[iii] Susmita Sridhar and Anabela Da Silva; Protocol using elliptically polarized light for enhanced contrast in polarization gating imaging of biological tissues. *Proc. SPIE - 9703, Optical Biopsy XIV: Toward Real-Time Spectroscopic Imaging and Diagnosis*, BiOS 2016, San Francisco, USA, 970319, 13 - 18 February, 2016.

[iv] Susmita Sridhar and Anabela Da Silva; Multiple wavelength probing of skin structures in depth with elliptically polarized light. *BIOMED 2016 - In Vivo Human Optical Imaging*, page TTh1B.5, OSA, Fort-Lauderdale, USA, 25 - 28 April, 2016.

[v] Susmita Sridhar and Anabela Da Silva; Enhanced contrast in polarization gating imaging of biological tissues with elliptically polarized light. *OptDIAG 2016*, l'Institut de Physique du Globe, Paris, France, 25 - 27 May, 2016. *[Oral Presentation]*.